Standard Model is best model (working title)

William Kennedy DiClemente

A DISSERTATION
in
Physics and Astronomy

Presented to the Faculties of The University of Pennsylvania
in Partial Fulfillment of the Requirements for the Degree of Doctor of Philosophy
2019 Last compiled: January 17, 2019

I. Joseph Kroll, Professor, Physics
Supervisor of Dissertation

Joshua Klein, Professor, Physics
Graduate Group Chairperson

Dissertation Committee
(Committee Prof. 1), Professor, Physics
(Committee Prof. 2), Associate Professor, Physics
(Committee Prof. 3), Professor, Physics
(Committee Prof. 4), Professor, Physics
I. Joseph Kroll, Professor, Physics

Standard Model is best model (working title)

Acknowledgements

I'd like to thanks the Ghosts of Penn Students Past for providing me with such an amazing thesis template.

ABSTRACT

STANDARD MODEL IS BEST MODEL (WORKING TITLE)

William Kennedy DiClemente

J. Kroll

This is the abstract text.

Contents

Acknowledgements iii

Abstract iv

Contents v

List of Tables ix

List of Figures xi

Preface xv

1 Introduction 1

2 Theoretical Framework 2
- 2.1 Introduction to the Standard Model . . . 2
- 2.2 Electroweak Mixing and the Higgs Field . . . 2

3 LHC and the ATLAS Detector 3
- 3.1 The Large Hadron Collider . . . 3
- 3.2 The ATLAS Detector . . . 3
  - 3.2.1 The Inner Detector . . . 3
    - 3.2.1.1 Pixel Detector . . . 3
    - 3.2.1.2 Semiconductor Tracker . . . 3
    - 3.2.1.3 Transition Radiation Tracker . . . 3
  - 3.2.2 The Calorimeters . . . 4

3.2.2.1 Liquid Argon Calorimeters . . . 4
3.2.2.2 Tile Calorimeters . . . 4
3.2.3 The Muon Spectrometer . . . 4
3.2.4 Particle reconstruction . . . 5
3.2.4.1 Track reconstruction . . . 5
3.2.4.2 Muon reconstruction . . . 5
3.2.4.3 Electron reconstruction . . . 5
3.2.4.4 Jet reconstruction . . . 5

4 Alignment of the ATLAS Inner Detector **6**
4.1 Effects of Misalignment . . . 6
4.2 The Alignment Method . . . 6
4.3 Momentum Bias Corrections . . . 6
4.4 Alignment of the IBL . . . 7
4.5 Alignment Monitoring . . . 7

5 Measurement of same-sign WW production at $\sqrt{s} = 13$ TeV with ATLAS **8**
5.0.1 Theoretical overview of vector boson scattering . . . 8
5.0.2 Same-sign $W^{\pm}W^{\pm}$ scattering . . . 10
5.0.3 Overview of backgrounds . . . 12
5.1 Data and Monte Carlo samples . . . 14
5.1.1 Monte Carlo samples . . . 14
5.2 Object and event selection . . . 15
5.2.1 Object selection . . . 15
5.2.1.1 Muon candidate selection . . . 16
5.2.1.2 Electron candidate selection . . . 18
5.2.1.3 Jet candidate selection . . . 18
5.2.1.4 Treatment of overlapping objects . . . 18
5.2.2 Signal event selection . . . 20
5.3 Background estimations . . . 22
5.3.1 Estimation of the WZ background . . . 22
5.3.2 Estimation of the $V\gamma$ background . . . 23
5.3.3 Estimation of backgrounds from charge misidentification . . . 25

5.3.3.1 Validation of the charge misidentification estimate 28
5.3.4 Estimation of non-prompt backgrounds with the fake factor method 29
5.3.4.1 Overview of the default fake factor method 29
5.3.4.2 The fake factor with $p_{\mathrm{T}}^{\mathrm{cone}}$ 30
5.3.4.3 Application of the fake factor 32
5.3.4.4 Systematic uncertainties 37
5.3.4.5 Results of the fake factor 37
5.3.4.6 Validation of the fake factor 39
5.3.5 Reduction of WZ background using custom overlap removal 42
5.4 Cross section measurement 45
5.5 Results 46

6 Prospects for same-sign WW at the High Luminosity LHC **47**
6.0.1 Analysis Overview 48
6.1 Theoretical motivation 48
6.1.1 Experimental sensitivity to longitudinal polarization 49
6.2 Monte Carlo samples 49
6.3 Background estimations 51
6.3.1 Truth-based isolation 52
6.4 Object and event selection 53
6.4.1 Object selection 53
6.4.2 Event selection 53
6.5 Selection optimization 54
6.5.1 Random grid search algorithm 54
6.5.2 Inputs to the optimization 56
6.5.3 Results of the optimization 57
6.6 Results 58
6.6.1 Event yields 58
6.6.2 Uncertainties 64
6.6.3 Cross section measurement 64
6.6.4 Longitudinal scattering significance 65

7 Conclusion **69**

A Additional material on truth isolation **70**

Bibliography **71**

List of Tables

5.1 Predicted cross sections for EQK and QCD production of diboson processes relevant to VBS at $\sqrt{s}$ = 8TeV using the SHERPA MC generator. Loose generator level cuts are applied on lepton $p_{\mathrm{T}} > 5$ GeV, dilepton invariant mass $m_{ll} > 4$ GeV, and at least two jets with $m_{jj} > 10$ GeV. 11
5.2 Summary of MC samples used in the analysis. 16
5.3 Muon selection criteria. All muons are required to pass the preselection (top), and then either the signal (middle) or loose (bottom) criteria is applied to the preselected electrons. 17
5.4 Electron selection criteria. All electrons are required to pass the preselection (top), and then either the signal (middle) or loose (bottom) criteria is applied to the preselected electrons. 19
5.5 Jet selection criteria. All jets are required to pass the above selection in order to be used in the analysis. 19
5.6 Summary of the overlap removal procedure used in the analysis. If the criteria in the "check" column is met, in the "result" column, the object on the left of the arrow is removed in favor of the object on the right. 20
5.7 Summary of trigger requirements for electrons and muons for $\sqrt{s}$ = 13TeV data collected in 2015 and 2016. At least one of the triggers must be satisfied. 21
5.8 The signal event selection 22
5.9 Event yields in the WZ control region before normalization. All lepton flavor channels are combined. 23
5.10 Selection criteria for the $V\gamma$ control region. 24
5.11 Event yields in the $V\gamma$ control region. The $V\gamma$ scale factor of 1.77 is calculated by scaling up the $Z\gamma$ and Z+jets backgrounds to account for the difference between the data and predicted total background. 25
5.12 Selection criteria for the same-sign inclusive validation region. 28
5.13 Event selection for the dijet region used for calculating the fake factor. The selected lepton can pass either the nominal (signal) or loose selections. In the case of the nominal leptons, the $p_{\mathrm{T}} > 27$ GeV requirement is replaced with $p_{\mathrm{T}} > 15$ GeV. 34
5.14 Values of the fake factor in each p_{T} bin and for each individual systematic source. . . . 38

5.15 Estimated yields for the fake lepton background. The estimated yield is shown in the first column together with the statistical uncertainty followed by the systematic uncertainties from variations of the the fake factors within their statistical (stat.) and systematic (syst.) uncertainties. The labels f_e and f_μ indicate the fake factors for electrons and muons, respectively. . . . 38
5.16 Selection criteria for the same-sign top fakes validation region. . . . 39
5.17 Custom OR definition. Leptons must pass this selection in order to be counted for the trilepton veto. . . . 45

6.1 Summary of MC samples used in the analysis. . . . 51
6.2 Truth-based isolation requirements for electrons and muons. . . . 52
6.3 Summary of the signal event selection. . . . 54
6.4 Updates to the $W^{\pm}W^{\pm}jj$ event selection criteria after optimization. Cuts not listed remain unchanged from the default selection in Table 6.3. . . . 58
6.5 Signal and background event yields using the default event selection for an integrated luminosity of $\mathcal{L} = 3000$ fb^{-1}. Events containing a fake or charge-flipped electron are removed from their respective sources and combined into a single entry each. . . . 62
6.6 Signal and background event yields using the optimized event selection for an integrated luminosity of $\mathcal{L} = 3000$ fb^{-1}. Events containing a fake or charge-flipped electron are removed from their respective sources and combined into a single entry each. . . . 62
6.7 Summary of estimated experimental and rate uncertainties. . . . 64

A.1 Event yields prior to applying any form of truth-based isolation criteria. . . . 70
A.2 Event yields after applying a test version of the truth-based isolation. . . . 70

List of Figures

3.1 General cut-away view of the ATLAS detector. 4

5.1 Cross sections in nanobarns for five different scattering processes of longitudinally polarized vector bosons as a function of center of mass energy $\sqrt{s}$. Without a SM Higgs boson (left), the cross sections grow unbounded with $\sqrt{s}$; however with a 120 GeV Higgs boson (right), the cross sections no longer diverge. 9

5.2 Tree-level Feynman diagrams for VBS EWK $VVjj$ production including triple gauge couplings involving W and/or Z bosons (top left and top middle), quartic gauge coupling (top right), or the exchange of a Higgs boson (s-channel bottom left and t-channel bottom right). The labels are quarks (q), fermions (f), and gauge bosons ($V = W, Z$). 10

5.3 Tree-level Feynman diagrams for non-VBS EWK $VVjj$ production. The labels are quarks (q), fermions (f), and gauge bosons ($V = W, Z$). 10

5.4 Tree-level Feynman diagrams for QCD $VVjj$ production. The labels are quarks (q), fermions (f), and gauge bosons ($V = W, Z$). 11

5.5 Feynman diagrams for VBS EWK production of $W^{\pm}W^{\pm}jj$ events. The leftmost diagram contains a quartic gauge coupling vertex, and the rightmost diagram contains an exchange of a Higgs boson. TODO: Make diagrams consistent with others 12

5.6 $W^{\pm}W^{\pm}jj$ VBS event topology containing two leptons (1 and 2) with the same electric charge, two neutrinos, and two forward tagging jets (3 and 4) with large rapidity separation Δy. 12

5.7 Generator level comparisons at $\sqrt{s} = 8$TeV of dijet invariant mass (m_{jj}, left) and dijet rapidity (Δy_{jj}, right) in EWK (red) and QCD (blue) $W^{\pm}W^{\pm}jj$ events. Both data sets have been normalized to the same area. 13

5.8 ATLAS event display of a $pp \to W^+W^+ \to \mu^+\nu_\mu\mu^+\nu_\mu jj$ event. The muons are represented by the red lines travelling from the ID through the MS, and the forward jets are represented by the blue cones with yellow energy deposits in the calorimeters. The direction of the $E_{\mathrm{T}}^{\mathrm{miss}}$ in the transverse plane is indicated by the gray dashed line in the inset image. Event display taken from [1]. 13

5.9 Leading lepton p_{T} (left) and η (right) distributions in the WZ control region before normalization. All lepton channels are combined. 24

5.10 Trilepton invariant mass m_{lll} distribution in the WZ control region before normalization. All lepton channels are combined. 24

5.11 Charge misidentification rates for electrons as a function of $|\eta|$ and p_{T}. Rates are calculated from $Z \to e^+e^-$ MC after applying sacle factors to approximate the charge mis-ID rates in data. . . . 26
5.12 Dilepton invariant mass distribution m_{ll} for the ee channel in the same-sign inclusive VR. 28
5.13 p_{T} distributions for the leading (left) and subleading (right) electron for the ee channel in the same-sign inclusive VR. In these plots, the cut requiring m_{ee} to fall within the Z mass window has been inverted in order to test the modelling away from the Z peak. . 29
5.14 Δp_{T} distributions for nominal (blue) and loose (red) muons in simulated $t\bar{t}$ events. Each muon has been matched to a truth-level jet. Both distributions are normalized to unit area. . . . 31
5.15 Δp_{T} distributions for muons (top) and electrons (bottom) in simulated $t\bar{t}$ events. Each lepton has been matched to a truth-level jet, and that truth jet has had its p_{T} corrected to include all truth muons within a cone of $\Delta R < 0.4$. The nominal leptons are in black. Δp_{T} is calculated for the loose leptons using p_{T} (red) and $p_{\mathrm{T}} + p_{\mathrm{T}}^{\mathrm{cone}}$ (blue). . . . 33
5.16 Distributions of $p_{\mathrm{T}}^{\mathrm{cone}}/p_{\mathrm{T}}$ for nominal (black) and loose (red) muons in simulated $t\bar{t}$ events. 34
5.17 The measured fake factor as a function of muon $p_{\mathrm{T}} + p_{\mathrm{T}}^{\mathrm{cone}}$. The error bars represent the statistical uncertainty only. . . . 35
5.18 The measured fake factor as a function of electron $p_{\mathrm{T}} + p_{\mathrm{T}}^{\mathrm{cone}}$ in the central ($|\eta| < 1.37$, blue) and forward ($|\eta| > 1.37$, red) regions of the detector. The error bars represent the statistical uncertainty only. . . . 35
5.19 Graphical representation of the fake factor application using $p_{\mathrm{T}} + p_{\mathrm{T}}^{\mathrm{cone}}$. The value of $p_{\mathrm{T}} + p_{\mathrm{T}}^{\mathrm{cone}}$ for the loose lepton is used to "look up" the fake factor weight which is then applied to the event. The loose lepton's p_{T} becomes $p_{\mathrm{T}} + p_{\mathrm{T}}^{\mathrm{cone}}$ for the purpose of the fake background estimation. . . . 36
5.20 Systematic variations in the fake factor as a function of muon $p_{\mathrm{T}} + p_{\mathrm{T}}^{\mathrm{cone}}$. The individual fake factors obtained for each systematic variation are displayed with their statistical uncertainties. . . . 39
5.21 Systematic variations in the fake factor as a function of electron $p_{\mathrm{T}} + p_{\mathrm{T}}^{\mathrm{cone}}$ in the central ($|\eta| < 1.37$, top) and forward ($|\eta| > 1.37$, bottom) regions of the detector. The individual fake factors obtained for each systematic variation are displayed with their statistical uncertainties. . . . 40
5.22 Distributions of the subleading lepton p_{T} in the same-sign top fakes VR for $\mu^\pm\mu^\pm$ events (top right), $e^\pm e^\pm$ events (top left), $\mu^\pm e^\pm$ events (bottom left), and all events combined (bottom right). All errors are statistical only. . . . 41
5.23 Pseudorapidity (η) distributions of truth muons (top) and electrons (bottom) for Sherpa $W^\pm W^\pm jj$ and WZ MC samples. The blue vertical lines represent the allowed η range for each lepton flavor. The numbers correspond to the number of raw MC events that fall within and outside of the allowed η range for each MC sample. . . . 43
5.24 Distributions of $p_{\mathrm{T,ratio}}(\mu, j)$ for EWK and QCD $W^\pm W^\pm jj$ signal (black) and WZ background (teal) for truth-matched third muons in events that pass the trilepton veto. Both distributions are normalized to unit area. The associated efficiency curves are on the right where efficiency is defined as the percentage of total events that would pass a cut on $p_{\mathrm{T,ratio}}(\mu, j)$ at a given value on the x-axis. . . . 43
5.25 Distributions of $\Delta R(\mu, j)$ for EWK and QCD $W^\pm W^\pm jj$ signal (black) and WZ background (teal) for truth-matched third muons in events that pass the trilepton veto. Both distributions are normalized to unit area. The associated efficiency curves are on the right where efficiency is defined as the percentage of total events that would pass a cut on $\Delta R(\mu, j)$ at a given value on the x-axis. . . . 44

5.26 Distributions of $p_{\mathrm{T,ratio}}(e,j)$ for EWK and QCD $W^{\pm}W^{\pm}jj$ signal (black) and WZ background (teal) for truth-matched third electrons in events that pass the trilepton veto. Both distributions are normalized to unit area. The associated efficiency curves are on the right where efficiency is defined as the percentage of total events that would pass a cut on $p_{\mathrm{T,ratio}}(e,j)$ at a given value on the x-axis. 44
5.27 Two-dimensional plots of $p_{\mathrm{T,ratio}}(\mu,j)$ vs $\Delta R(\mu,j)$ for truth-matched third muons in events that pass the trilepton veto for EWK and QCD $W^{\pm}W^{\pm}jj$ signal (left) and WZ background (right). The blue overlay indicates the area in which the third leptons will pass the custom OR and result in the event failing the trilepton veto. 45

6.1 Comparison of the leading (top) and subleading (bottom) lepton p_{T} distributions for purely longitudinal (LL, black) and mixed polarization (LT+TT, cyan) $W^{\pm}W^{\pm}jj$ events. 50
6.2 Comparison of the azimuthal dijet separation ($|\Delta\phi_{jj}|$) for purely longitudinal (LL, black) and mixed polarization (LT+TT, cyan) $W^{\pm}W^{\pm}jj$ events. 51
6.3 A visual representation of a rectangular grid search algorithm. The signal events are the blue triangles, and the red circles are the background events. TODO: replace with own figure 55
6.4 A visual representation of a random grid search algorithm. The signal events are the blue triangles, and the red circles are the background events. TODO: replace with own figure 56
6.5 Leading lepton p_{T} distribution. The default and optimized cuts are represented by the red and green dashed lines, respectively. The $W^{\pm}W^{\pm}jj$ EWK signal (black points) is normalized to the same area as the sum of the backgrounds (colored histogram). TODO: Move to appendix or omit 59
6.6 Dilepton invariant mass distribution. The default and optimized cuts are represented by the red and green dashed lines, respectively. The $W^{\pm}W^{\pm}jj$ EWK signal (black points) is normalized to the same area as the sum of the backgrounds (colored histogram). TODO: Move to appendix or omit 59
6.7 Leading (top) and subleading (bottom) jet p_{T} distributions. The default and optimized cuts are represented by the red and green dashed lines, respectively. The $W^{\pm}W^{\pm}jj$ EWK signal (black points) is normalized to the same area as the sum of the backgrounds (colored histogram). 60
6.8 Dijet invariant mass distribution. The default and optimized cuts are represented by the red and green dashed lines, respectively. The $W^{\pm}W^{\pm}jj$ EWK signal (black points) is normalized to the same area as the sum of the backgrounds (colored histogram). TODO: Move to appendix or omit 61
6.9 Lepton-jet centrality distribution. The default and optimized cuts are represented by the red and green dashed lines, respectively. The $W^{\pm}W^{\pm}jj$ EWK signal (black points) is normalized to the same area as the sum of the backgrounds (colored histogram). 61
6.10 p_{T} distributions for the leading jet using the default (left) and optimized (right) event selections for all channels combined. 63
6.11 p_{T} distributions for the subleading jet using the default (left) and optimized (right) event selections for all channels combined. 63
6.12 p_{T} distributions for lepton-jet centrality ζ using the default (left) and optimized (right) event selections for all channels combined. 63
6.13 Projections of the statistical (black), theoretical (blue), systematic (yellow), and total (red) uncertainties on the measured cross section as a function of integrated luminosity using the optimized event selection. 65

6.14 Dijet azimuthal separation ($|\Delta\phi_{jj}|$) for the low m_{jj} region ($520 < m_{jj} < 1100$ GeV, top) and the high m_{jj} region ($m_{jj} > 1100$ GeV, bottom). The purely longitudinal (LL, gray) is plotted separately from the mixed and transverse (LT+TT, cyan) polarizations. . . . 67
6.15 Projections of the expected longitudinal scattering significance as a function of integrated luminosity when considering all sources of uncertainties (black) or only statistical uncertainties (red). 68

Preface

This is the preface. It's optional, but it's nice to give some context for the reader and stuff.

Will K. DiClemente
Philadelphia, February 2019

Chapter 1

Introduction

The Standard Model (SM)[1] has been remarkably successful...

[1] Here's a footnote.

Chapter 2

Theoretical Framework

(Some example introductory text for this chapter)...

2.1 Introduction to the Standard Model

Modern particle physics is generally interpreted in terms of the Standard Model (SM). This is a quantum field theory which encapsulates our understanding of the electromagnetic, weak, and strong interactions...

2.2 Electroweak Mixing and the Higgs Field

When the theory of the electroweak interaction was first developed [2, 3], the W and Z bosons were predicted to be massless (a typical mass term in the Lagrangian would violate the SU(2) symmetry). However, these were experimentally observed to have masses...

Chapter 3

LHC and the ATLAS Detector

3.1 The Large Hadron Collider

The Large Hadron Collider (LHC) [4] is...

3.2 The ATLAS Detector

ATLAS is a general-purpose particle detector...

3.2.1 The Inner Detector

The Inner Detector serves the primary purpose of measuring the trajectories of charged particles...

3.2.1.1 Pixel Detector

The Pixel detector consists of four cylindrical barrel layers and three disk-shaped endcap layers...

3.2.1.2 Semiconductor Tracker

The Semiconductor Tracker uses the same basic technology as the Pixels, but the fundamental unit of silicon is a larger "strip"...

3.2.1.3 Transition Radiation Tracker

The Transition Radiation Tracker is the outermost component of the ID...

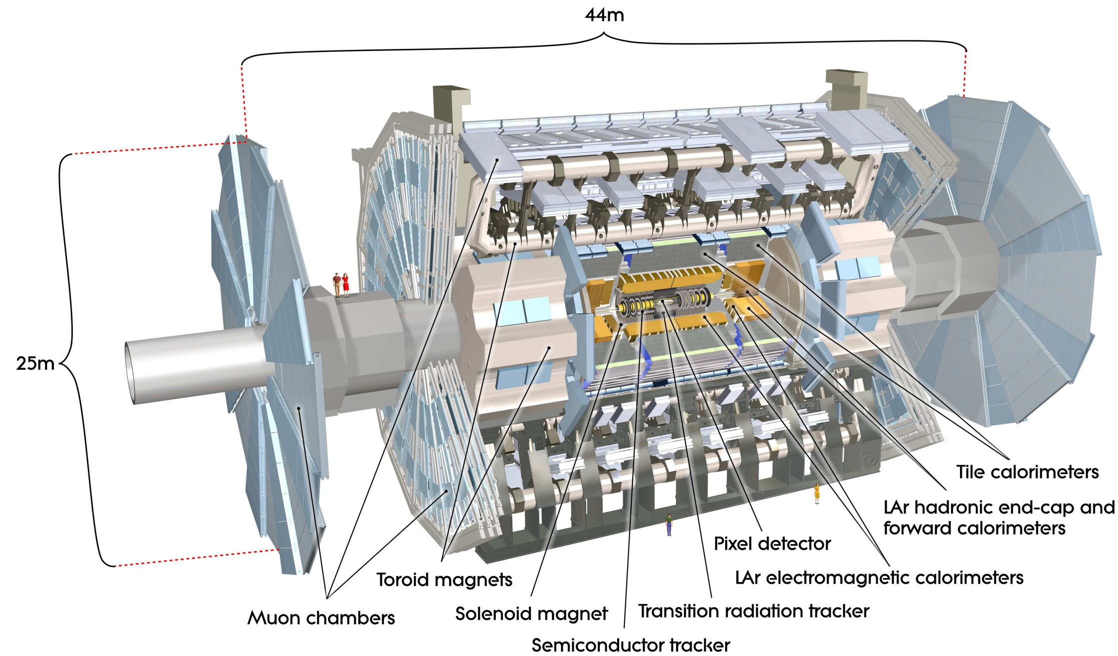

Figure 3.1: General cut-away view of the ATLAS detector [5].

3.2.2 The Calorimeters

ATLAS includes two types of calorimeter system for measuring electromagnetic and hadronic showers. These are the Liquid Argon (LAr) calorimeters and the Tile calorimeters. Together, these cover the region with $|\eta| < 4.9$...

3.2.2.1 Liquid Argon Calorimeters

The Liquid Argon system consists of...

3.2.2.2 Tile Calorimeters

The Tile calorimeter provides coverage for hadronic showers...

3.2.3 The Muon Spectrometer

Muon spectrometer stuff.

3.2.4 Particle reconstruction

Particle reconstruction algorithms

3.2.4.1 Track reconstruction

3.2.4.2 Muon reconstruction

3.2.4.3 Electron reconstruction

3.2.4.4 Jet reconstruction

Chapter 4

Alignment of the ATLAS Inner Detector

In order for the subdetectors of the ID to operate at their designed precisions, it is essential that the locations of the sensors be known as precisely as possible. Differences between the expected and actual positions of a sensor can result in displaced particle hits and degrade track reconstruction quality. These misalignments can occur for any number of reasons, including but not limited to elemnts shifting during maintenance periods or cycles in ATLAS's magnetic field, or simply small movements during normal detector operations. Since it is not practical to physically realign hundreds of thousands of detector elements to μm precision by hand, an iterative track-based alignment algorithm is used to determine the physical positions and orientations of these elements [6]. The effects of misalignments and the steps taken to correct and monitor them are detailed in this chapter.

4.1 Effects of Misalignment

Hello world!

4.2 The Alignment Method

Hello world!

4.3 Momentum Bias Corrections

Hello world!

4.4 Alignment of the IBL

Hello world!

4.5 Alignment Monitoring

Hello world!

Chapter 5

Measurement of same-sign WW production at $\sqrt{s} = 13$ TeV with ATLAS

Production of same-sign W boson pairs is a particularly interesting SM process. When produced via vector boson scattering (VBS), $W^\pm W^\pm jj$ is particularly sensitive to the electroweak symmetry breaking (EWSB) mechanism as well as potential "beyond the Standard Model" (BSM) physics. $W^\pm W^\pm jj$ events can be produced via electroweak-mediated (EWK) diagrams, of which VBS is a subset, or QCD-mediated diagrams. The biggest advantage of same-sign $W^\pm W^\pm jj$ lies in its ratio of electroweak (EWK) to QCD production cross sections. Despite the opposite-sign $W^\pm W^\mp$ having a considerably larger total cross section, its EWK-mediated diagrams are considerably smaller than its QCD-mediated diagrams, while for same-sign $W^\pm W^\pm$ the ratio is approximately one to one. This makes $W^\pm W^\pm jj$ one of the best channels for studying VBS at the LHC.

The first evidence of electroweak (EWK) $W^\pm W^\pm jj$ production was seen by the ATLAS and CMS experiments at $\sqrt{s} = 8$ TeV with exesses of 3.6σ [7] and 2.0σ [8] over backgrounds, respectively. More recently, ATLAS and CMS have both observed the EWK process at $\sqrt{s} = 13$ TeV with significances of 6.9σ [1] and 5.5σ [9], respectively. The analysis presented in this chapter is based off of the ATLAS $\sqrt{s} = 13$ TeV observation and cross section measurement of EWK $W^\pm W^\pm jj$ production [1, 10].

5.0.1 Theoretical overview of vector boson scattering

VBS processes are very important to understand due to their sensitivity to the EWSB mechanism. The scattering amplitude of longitudinally polarized vector bosons grows with center-of-mass energy and ultimately violates unitarity above $\sqrt{s} = 1$ TeV in the absence of a light SM Higgs boson [11, 12]. However, once the Higgs is introduced, the divergences cancel and the cross section no longer grows unbounded, as can be seen in Figure 5.1, which consists of plots from [13].

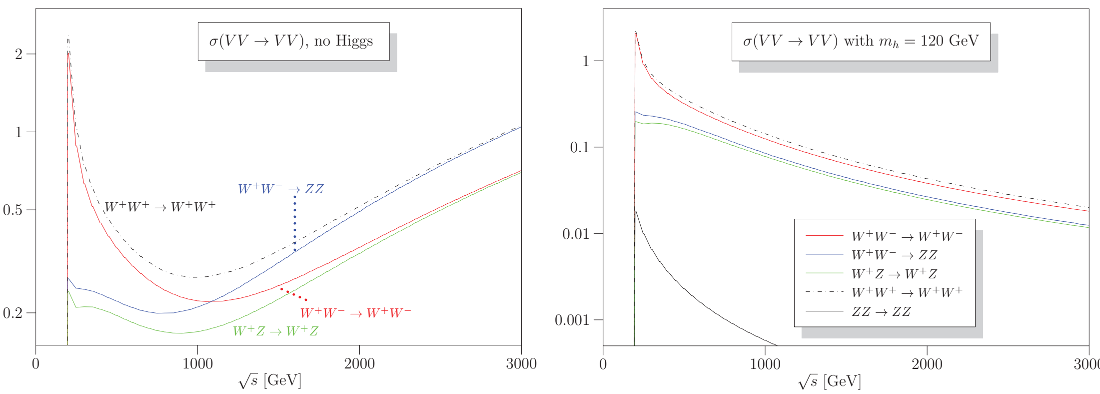

Figure 5.1: Cross sections in nanobarns for five different scattering processes of longitudinally polarized vector bosons as a function of center of mass energy $\sqrt{s}$. Without a SM Higgs boson (left), the cross sections grow unbounded with $\sqrt{s}$; however with a 120 GeV Higgs boson (right), the cross sections no longer diverge. Plots taken from [13].

With the discovery of the Higgs boson in 2012 [14, 15], the EWSB mechanism can now be directly studied. Due to the exchange of a Higgs in the s- and t-channel VBS diagrams ($W^{\pm}W^{\pm}jj$ itself only contains the t-channel diagram), VBS processes are directly sensitive to properties of the Higgs. For example, the high-mass tail in the VV scattering system allows an approximation of the effective coupling strength of the Higgs to vector bosons that is independent of any assumptions on the Higgs width [16]. Additionally, the center of mass energy dependence of the VV scattering can reveal whether the Higgs boson unitarizes the longitudinal scattering amplitude fully or only partially [17].

VBS events are characterized by two quarks from the colliding protons each radiating a massive vector boson which then scatter and decay in the detector. The incoming quarks carry a large amount of momentum and only deflect a small amount upon radiating the vector boson; as a result, they often travel very close to the beam line. Ignoring the decay products of the bosons, these VBS events result in a final state of two vector bosons (V) and two jets (j) at high pseudorapidities (called *forward jets*) from the outgoing quarks. The shorthand $VVjj$ is used to represent this final state.

$VVjj$ events can be produced via two different physical processes. The first involves purely electroweak interactions in the tree-level diagrams, with $\mathcal{O}(\alpha_{\mathrm{EWK}}) = 6$ and will be referred to as *EWK production*. This can be further broken down into VBS and non-VBS production. In the VBS EWK production, the scattering occurs via triple or quartic gauge couplings, as well as the s- or t-channel exchange of a Higgs boson. The non-VBS EWK production contains the same final state of two vector bosons and two outgoing quarks, but the bosons do not scatter. Due to gauge invariance, it is not possible to separate the VBS from the non-VBS productions [18]; therefore, both are included in the signal generation and are indistinguishable from one another. The second process involves a mix of the EWK and strong interactions, of order $\mathcal{O}(\alpha_s) = 2 \otimes \mathcal{O}(\alpha_{\mathrm{EWK}}) = 4$ and will be referred to as *QCD production*. The tree-level Feynman diagrams for VBS EWK, non-VBS EWK, and QCD $VVjj$ production are found in Figures 5.2, 5.3, and 5.4, respectively.

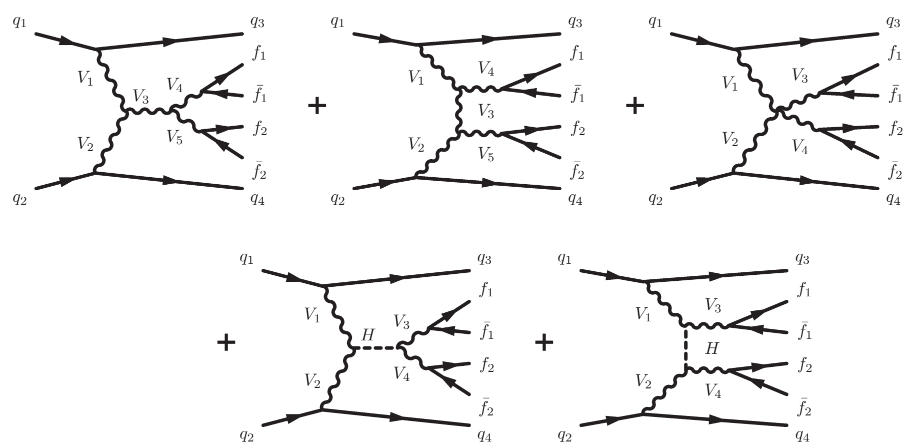

Figure 5.2: Tree-level Feynman diagrams for VBS EWK $VVjj$ production including triple gauge couplings involving W and/or Z bosons (top left and top middle), quartic gauge coupling (top right), or the exchange of a Higgs boson (s-channel bottom left and t-channel bottom right). The labels are quarks (q), fermions (f), and gauge bosons ($V = W, Z$).

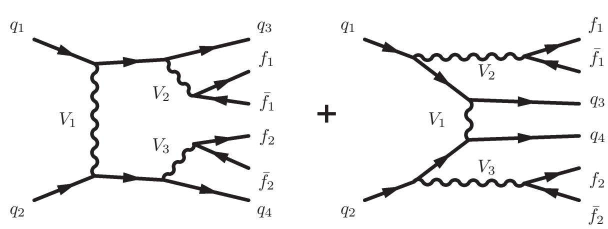

Figure 5.3: Tree-level Feynman diagrams for non-VBS EWK $VVjj$ production. The labels are quarks (q), fermions (f), and gauge bosons ($V = W, Z$).

5.0.2 Same-sign $W^{\pm}W^{\pm}$ scattering

Same-sign $W^{\pm}W^{\pm}jj$ scattering is considered to be one of the best channels for studying VBS at the LHC [16]. This is due primarily to the ratio of the EWK to the QCD production, which matters a great deal due to the VBS events being a subset of the total EWK production. In an analysis

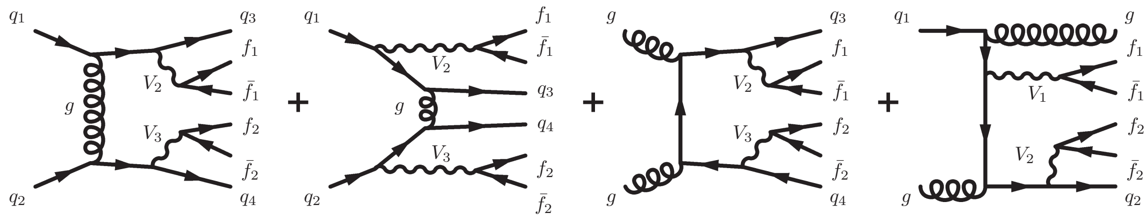

Figure 5.4: Tree-level Feynman diagrams for QCD $VVjj$ production. The labels are quarks (q), fermions (f), and gauge bosons ($V = W, Z$).

the EWK production would be conisdered the signal and the QCD production a background, so a favorable ratio of the two helps greatly when comparing the size of the signal to the backgrounds. A study at $\sqrt{s} = 8$ TeV [19] was done using the SHERPA Monte Carlo (MC) generator to calculate EWK and QCD production cross sections at leading order for a variety of $VVjj$ processes decaying to leptons and can be found in Table 5.1. Despite its lower cross section compared to other $VVjj$ processes, the EWK to QCD ratio for $W^{\pm}W^{\pm}jj$ is approximately one-to-one, whereas for opposite-sign $W^{\pm}W^{\mp}jj$ the ratio is closer to 3%.

Process	Final state	σ_{EWK}	σ_{QCD}
$W^{\pm}W^{\pm}$	$l^{\pm}l^{\pm}\nu\nu jj$	19.5 fb	18.8 fb
$W^{\pm}W^{\mp}$	$l^{\pm}l^{\mp}\nu\nu jj$	91.3 fb	3030 fb
$W^{\pm}Z$	$l^{\pm}l^{\pm}l^{\mp}\nu jj$	30.2 fb	687 fb
ZZ	$l^{+}l^{-}\nu\nu jj$	2.4 fb	162 fb
ZZ	$l^{+}l^{-}l^{+}l^{-}jj$	1.5 fb	106 fb

Table 5.1: Predicted cross sections for EQK and QCD production of diboson processes relevant to VBS at $\sqrt{s} = 8$ TeV using the SHERPA MC generator. Loose generator level cuts are applied on lepton $p_{\text{T}} > 5$ GeV, dilepton invariant mass $m_{ll} > 4$ GeV, and at least two jets with $m_{jj} > 10$ GeV. Numbers taken from [19].

This analysis studies $W^{\pm}W^{\pm}jj$ scattering where both W bosons decay leptonically to $e\nu$ or $\mu\nu$[2]. The $W^{\pm}W^{\pm}jj$ VBS final state consists of two leptons with the same electric charge, two neutrinos, and two high energy forward jets with a large invariant mass. Tree-level Feynman diagrams of VBS $W^{\pm}W^{\pm}jj$ production can be found in Figure 5.5 and a visual representation of the VBS topology can be found in Figure 5.6. The two forward jets also serve as a powerful tool to suppress the QCD production mode. In EWK events, the two jets tend to have much higher separation and a larger combined invariant mass than the two leading jets in a QCD event. The two plots shown in

[2] Throughout the rest of this chapter, l denotes either electrons (e) or muons (μ) unless stated otherwise. Additionally, e, μ, and ν (neutrino) with no charge or anti-particle designation refer interchangeably to either the particle or anti-particle.

Figure 5.7 highlight the differences in these dijet quantities between the two production modes. An ATLAS event display of a real $W^{\pm}W^{\pm}jj$ candidate event is shown in Figure 5.8.

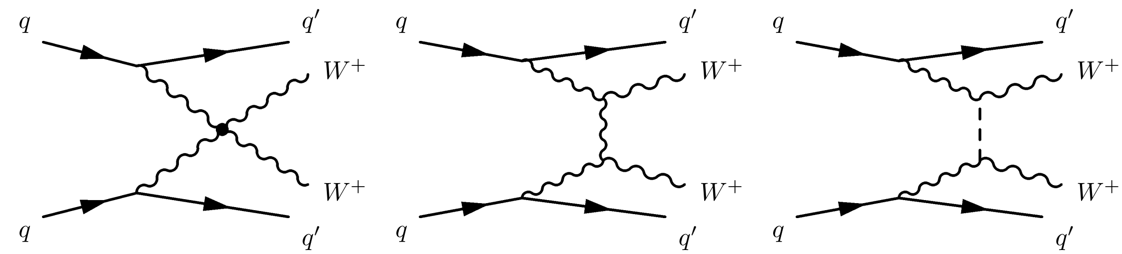

Figure 5.5: Feynman diagrams for VBS EWK production of $W^{\pm}W^{\pm}jj$ events. The leftmost diagram contains a quartic gauge coupling vertex, and the rightmost diagram contains an exchange of a Higgs boson. TODO: Make diagrams consistent with others

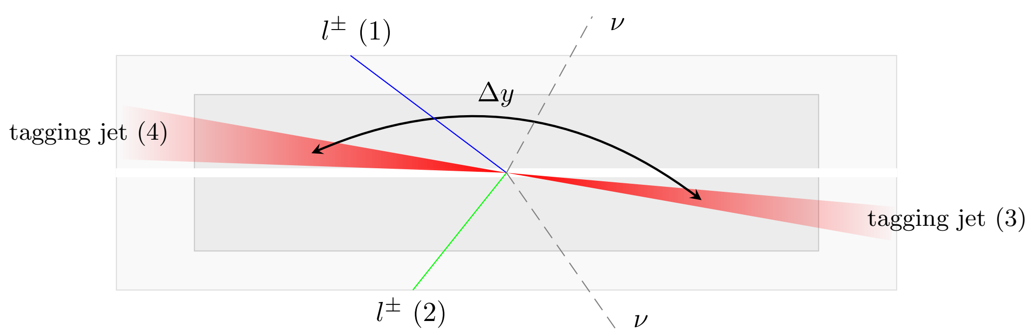

Figure 5.6: $W^{\pm}W^{\pm}jj$ VBS event topology containing two leptons (1 and 2) with the same electric charge, two neutrinos, and two forward tagging jets (3 and 4) with large rapidity separation Δy.

5.0.3 Overview of backgrounds

In addition to QCD production of $W^{\pm}W^{\pm}jj$ events, there are several other processes that can end up with a final state of two same-sign leptons, two neutrinos, and two jets. However, due to the ± 2 final state charge, there is a considerable reduction in SM backgrounds (such as Z boson events) when compared to an analysis like opposite-sign $W^{\pm}W^{\mp}jj$.

One of the largest sources of background involves processes with prompt leptons[3]. These are events that contain two leptons with the same electric charge and one or more additional leptons

[3]Prompt leptons are those that are produced in the primary collision and are a direct decay product of the process of interest. Non-prompt leptons originate from some secondary process, such as a b-hadron decay, or are jets that get mis-reconstructed as a lepton.

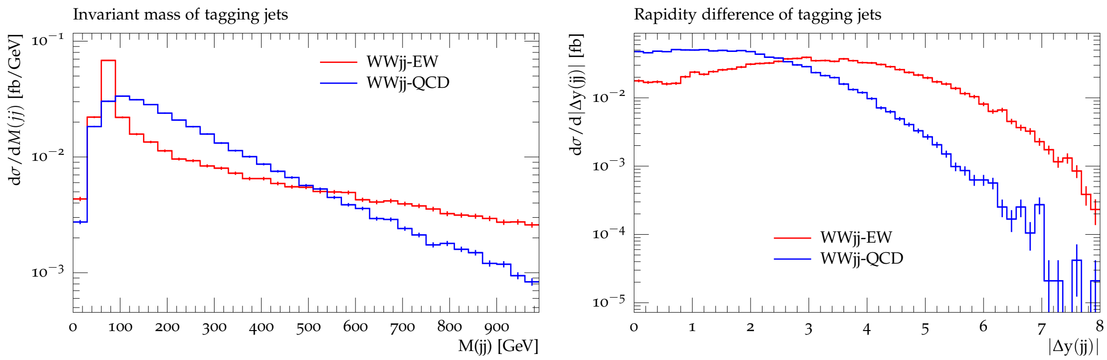

Figure 5.7: Generator level comparisons at $\sqrt{s} = 8$ TeV of dijet invariant mass (m_{jj}, left) and dijet rapidity (Δy_{jj}, right) in EWK (red) and QCD (blue) $W^{\pm}W^{\pm}jj$ events. Both data sets have been normalized to the same area. Plots taken from [19].

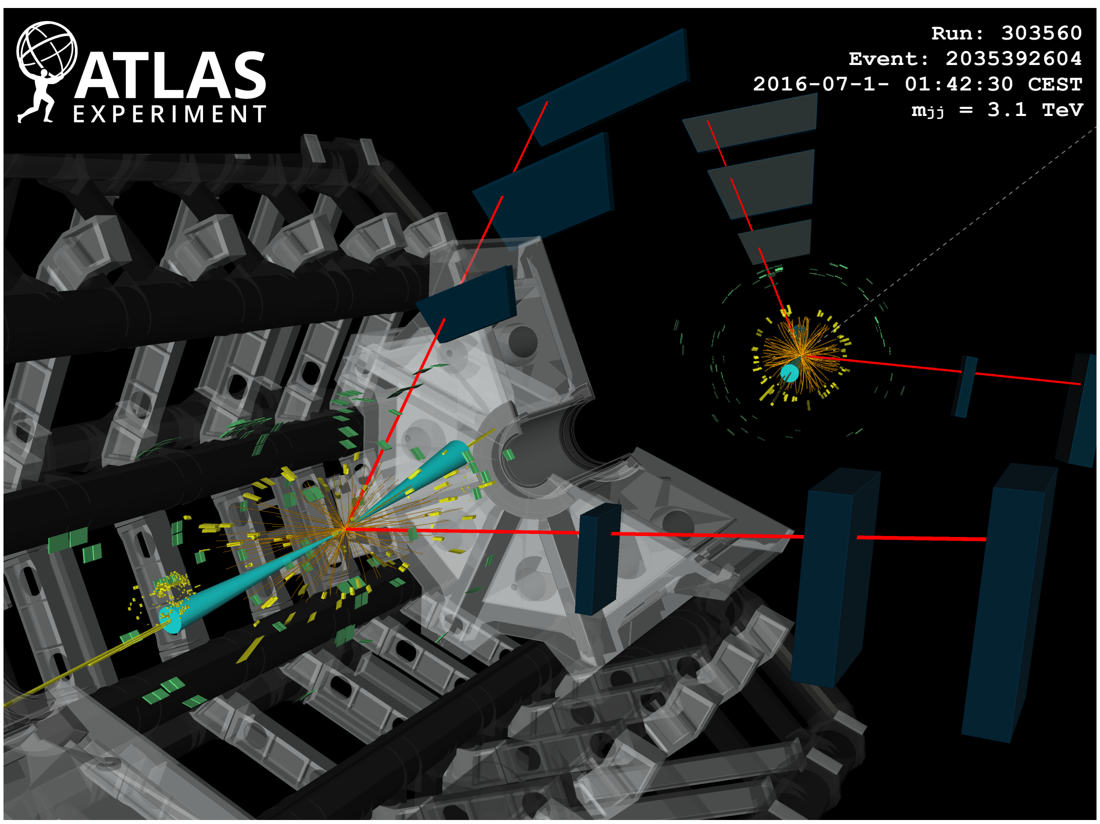

Figure 5.8: ATLAS event display of a $pp \to W^+W^+ \to \mu^+\nu_\mu\mu^+\nu_\mu jj$ event. The muons are represented by the red lines travelling from the ID through the MS, and the forward jets are represented by the blue cones with yellow energy deposits in the calorimeters. The direction of the $E_{\mathrm{T}}^{\mathrm{miss}}$ in the transverse plane is indicated by the gray dashed line in the inset image. Event display taken from [1].

that are "lost", either by failing the selection criteria or falling outside of the detector's acceptance. The number of processes that can contribute is limited by the requirement of same-sign leptons, and as a result this background is dominated by processes involving two or more vector bosons, with the largest contribution coming from WZ events and smaller contributions from ZZ and $t\bar{t}V$ events. Triboson events where one boson decays hadronically also contribute to this background; however, the jets are generally softer and more central than in a typical VBS event, and the cuts applied on the forward jets suppress these contributions.

The other dominant background comes from non-prompt, or "fake", leptons. Here one or more leptons originate from the decay of another particle unrelated to the signal process, such as a heavy-flavor decay or photon conversion, or come from a jet that is misidentified as a lepton. This background is mostly made up of events from $t\bar{t}$ and W+jets processes, with a much smaller contribution from $V\gamma$ events. TODO: check whether $V\gamma$ really qualifies as non-prompt, we lump $Z\gamma$ in with the charge flip background in the paper...

Finally, opposite-sign lepton pairs can enter the signal region if one of the leptons is reconstructed with the wrong charge (called *charge misidentification*[4]). In practice, this only affects events with electrons, as the charge misidentification rate for muons is negligible [20]. This is a major background in events with two electrons, but is a much smaller contribution for events with one electron and one muon.

5.1 Data and Monte Carlo samples

This analysis uses 36.1 fb^{-1} of $\sqrt{s} = 13$ TeV proton-proton collision data recorded by ATLAS during 2015 and 2016. The uncertainty in the combined integrated luminosity is 2.1%. It is derived following a methodology similar to that detailed in [21] and using the LUCID-2 detector for the baseline luminosity measurements [22] from calibration of the luminosity scale using x-y beam-separation scans.

5.1.1 Monte Carlo samples

A number of Monte Carlo (MC) simululations are employed to model signal and background processes. In order to model the real collision data as closely as possible, each MC has been run through a full simulation of the ATLAS detector [23] in `GEANT4` [24], and events have been reconstructed

[4] Charge misidentification is also referred to interchangeably as *charge mis-ID* and *charge flip*.

using the same algorithms as the data. The simulation reproduces as closely as possible the momentum resolutions and calorimeter responses of the detector, and also includes the effects of pileup by including soft QCD interactions using `PYTHIA v8.1` [25]. The MC samples used in this analysis are detailed in this section and summarized in Table 5.2.

The $W^{\pm}W^{\pm}jj$ samples are modeled using `SHERPA v2.2.2` [26, 27, 28] with the `NNPDF3.0` PDF set [29]. The EWK signal samples are generated by fixing the electroweak coupling constant to $\mathcal{O}(\alpha_W) = 6$, and a QCD background sample was also generated with $\mathcal{O}(\alpha_W) = 4$. `SHERPA` includes up to one parton at next-to-leading order (NLO) and up to three at leading order (LO) in the strong coupling constant α_s. A second $W^{\pm}W^{\pm}jj$ EWK sample is generated using `POWHEG-BOX v2` [30] with the `NNPDF3.0` PDF set and at NLO accuracy. This sample is only used for systematic studies, as `POWHEG-BOX` does not include resonant triboson contributions in its matrix element, which are non-negligible at NLO [31].

Diboson processes (VV where $V = W, Z$) are simulated with `SHERPA v2.2.2` for mixed hadronic and leptonic decays and `SHERPA v2.2.1` for fully leptonic decays of the bosons. Similarly, triboson (VVV) and $V\gamma$ processes are simulated using `SHERPA v2.1.1` with up to one parton at NLO and up to three at LO. W+jets processes are simulated with `SHERPA`2.2.1 with up to two partons at NLO and four at LO. All the above `SHERPA` samples use the `NNPDF3.0` PDF set and `SHERPA`'s own parton showering. The Z+jets events are generated with `Madgraph5_aMC@NLO` [32] at LO and interfaced with `PYTHIA v8.1` for parton showering.

$t\bar{t}$ events are generated using `POWHEG-BOX v2` with the `CT10` PDF set [33]. $t\bar{t}V$ samples are generated at NLO with `Madgraph5_aMC@NLO` and the `NNPDF3.0` PDF set interfaced with `PYTHIA v8` for parton showering. Finally, single top events are generated with `POWHEG-BOX v1` and the `CT10f4` PDF set interfaced with `PYTHIA v6` [34] for parton showering.

5.2 Object and event selection

This section details the selection criteria for objects used in the analysis as well as the selection for signal events.

5.2.1 Object selection

Muons, electrons, and jets all must pass strict selection requirements to ensure that only high quality, well measured objects are used. For leptons, a baseline selection is defined (called the *preselection*), which all leptons must pass in order to be considered for the analysis. This preselection is an

Process	Generator	Comments
$W^{\pm}W^{\pm}jj$ (EWK)	`SHERPA v2.2.2`	Signal sample
$W^{\pm}W^{\pm}jj$ (EWK)	`POWHEG-BOX v2`	Systematics sample
$W^{\pm}W^{\pm}jj$ (QCD)	`SHERPA v2.2.2`	
Diboson	`SHERPA v2.2.2`	Both bosons decay leptonically ($llll$, $lll\nu$, $ll\nu\nu$)
	`SHERPA v2.2.1`	One boson decays leptonically, the other hadronically
Triboson	`SHERPA v2.1.1`	
W+jets	`SHERPA v2.2.1`	
Z+jets	`Madgraph5_aMC@NLO`	
$V\gamma$	`SHERPA v2.1.1`	
$V\gamma jj$ (EWK)	`SHERPA v2.2.4`	
$t\bar{t}V$	`Madgraph5_aMC@NLO`	
$t\bar{t}$	`POWHEG-BOX v2`	
Single top	`POWHEG-BOX v1`	EWK t-, s-, & Wt-channels

Table 5.2: Summary of MC samples used in the analysis.

intentionally loose set of criteria in order to have high acceptance for rejecting backgrounds with additional leptons (i.e. $WZ \to 3l\nu jj$). Signal leptons are then required to satisfy a much tighter *signal selection* aimed at suppressing backgrounds from non-prompt or fake leptons. A third set of lepton selection criteria, the *loose selection*, defines a sample enriched in non-prompt leptons, and it is used in the fake factor method for estimating the non-prompt background, discussed in detail in Section 5.3.4. Jets are only required to pass one set of selection criteria. These selections are detailed in the following sections and summarized in Table 5.3 for muons, Table 5.4 for electrons, and Table 5.5 for jets.

5.2.1.1 Muon candidate selection

Cuts on muon p_{T} serve to reject low momentum leptons from background processes and additional collisions from pileup events. Preselected muons must have $p_{\mathrm{T}} > 6$ GeV and signal muons $p_{\mathrm{T}} >$ 27 GeV. The p_{T} requirement for loose muons is lower than for signal muons, $p_{\mathrm{T}} > 15$ GeV, for reasons that are discussed in Section 5.3.4. TODO: reference proper subsection when it's done Muons are required to fall within the detector's η acceptance: $|\eta| < 2.7$ for preselected muons, which is tightened to $|\eta| < 2.5$ for the signal muons.

Cuts on the transverse and longitudinal impact parameters are applied to ensure that the candidate muon originated from the primary particle interaction and not some other source, such as a heavy flavor decay. The preselection and the loose selection both have looser requirements on the transverse impact parameter significance (d_0/σ_{d_0}) than the signal selection; all three have the same requirement on the transverse impact paramter ($|z_0 \times \sin\theta|$).

Finally, the muon candidates are required to pass a particle identification and an isolation criteria as defined in [35]. The methods used in constructing the identification and isolation workingpoints are described in more detail in Section 3.2.4.2. The muon identification serves to select prompt muons with high efficiency and well measured momenta.This analysis uses two different workingpoints, `Loose` for preselected muons and `Medium` for loose and signal muons, where `Medium` muons are a tighter subset of those that pass the `Loose` requirement. Muon isolation is a measurement of detector activity around the muon candidate, and it is measured with both track-based and calorimeter-based variables. The isolation workingpoint used for the signal muons, `Gradient`, is defined such that there is 90% or better background rejection efficiency for 25 GeV muons, and 99% efficiency at 60 GeV. There is no minimum isolation requirement for preselected or loose muons. Loose muons are additionally required to fail one or both of the signal transverse impact parameter cut and signal isolation requirement.

Muon preselection

Momentum cut	$p_{\mathrm{T}} > 6$ GeV
Angular acceptance	$\|\eta\| < 2.7$
Longitudinal impact parameter	$\|z_0 \times \sin\theta\| < 0.5$ mm
Transverse impact parameter	$d_0/\sigma_{d_0} < 10$
Particle identification	`Loose`

Muon signal selection

Momentum cut	$p_{\mathrm{T}} > 27$ GeV
Angular acceptance	$\|\eta\| < 2.5$
Longitudinal impact parameter	$\|z_0 \times \sin\theta\| < 0.5$ mm
Transverse impact parameter	$d_0/\sigma_{d_0} < 3$
Particle identification	`Medium`
Particle isolation	`Gradient`

Muon loose selection

Momentum cut	$p_{\mathrm{T}} > 15$ GeV
Angular acceptance	$\|\eta\| < 2.5$
Longitudinal impact parameter	$\|z_0 \times \sin\theta\| < 0.5$ mm
Transverse impact parameter	$d_0/\sigma_{d_0} < 10$
Particle identification	`Medium`
Fail signal transverse impact parameter and/or isolation cuts	

Table 5.3: Muon selection criteria. All muons are required to pass the preselection (top), and then either the signal (middle) or loose (bottom) criteria is applied to the preselected electrons.

5.2.1.2 Electron candidate selection

The electron candidate selections are very similar to those for muons. The p_T cut starts at $p_\mathrm{T} >$ 6 GeV for the preselection, increases to $p_\mathrm{T} > 20$ GeV for loose electrons, and finally to $p_\mathrm{T} > 27$ GeV for signal electrons. The $|\eta|$ cut for electrons requires $|\eta| < 2.47$ for all electrons, with the region $1.37 \leq |\eta| \leq 1.52$ removed from loose and signal electrons. This region is where the electromagnetic calorimeter transitions from the barrel to the endcaps and is not fully instrumented. Both the transverse and longitudinal impact parameter cuts are the same for all electron selections.

The electron particle identification uses a multivariate likelihood technique (LH) [36] detailed in Section 3.2.4.3. Preselected electrons must pass the loosest LH workingpoint `LooseLH` with an additional requirement that there be a reconstructed track hit in the first layer of the pixel detector (a so-called B-layer hit). The LH requirement for the loose and signal electrons the tighness of the identification using `MediumLH` and `TightLH`, respectively. As for isolation, the `Gradient` workingpoint is required for signal electrons only. The loose electrons must fail one or both of the signal identification and isolation requirements.

5.2.1.3 Jet candidate selection

The final objects that need to pass selection are jets. Jets are clustered using the anti-k_t algorithm [37] within a radius of $\Delta R = 0.4$. The jets are then calibrated using E_T- and η-dependent correction factors that are trained using MC simulations [38]. These calibrated jets are then required to have $p_\mathrm{T} > 30$ GeV if they lie in the forward regions of the detector ($2.4 < |\eta| < 4.5$) and $p_\mathrm{T} > 25$ GeV in the central region ($|\eta| \leq 2.4$). In order to suppress pileup jets, the so-called jet-vertex-tagger (JVT) discriminant associates a jet with the primary interaction vertex [39]; central jets with $p_\mathrm{T} > 60$ GeV are required to pass the `Medium` JVT workingpoint, which corresponds to an average efficiency of over 92%. Finally, the jets are required to be separated by selected prompt leptons by at least $\Delta R(j, l) > 0.3$.

5.2.1.4 Treatment of overlapping objects

In the event that one or more objects are reconstructed very close to each other, there is the possiblity for double-counting if both originated from the same object. The procedure by which this ambiguity is resolved is called *overlap removal* (OR). The standard ATLAS recommendation for OR is implemented in this analysis [40, 41] and is summarized in Table 5.6.

Electron preselection	
Momentum cut	$p_{\mathrm{T}} > 6$ GeV
Angular acceptance	$\lvert\eta\rvert < 2.47$
Longitudinal impact parameter	$\lvert z_0 \times \sin\theta\rvert < 0.5$ mm
Transverse impact parameter	$d_0/\sigma_{d_0} < 5$
Particle identification	`LooseLH` + B-layer hit

Electron signal selection	
Momentum cut	$p_{\mathrm{T}} > 27$ GeV
Angular acceptance	$\lvert\eta\rvert < 2.47$, excluding $1.37 \leq \lvert\eta\rvert \leq 1.52$
Longitudinal impact parameter	$\lvert z_0 \times \sin\theta\rvert < 0.5$ mm
Transverse impact parameter	$d_0/\sigma_{d_0} < 5$
Particle identification	`TightLH`
Particle isolation	`Gradient`

Electron loose selection	
Momentum cut	$p_{\mathrm{T}} > 20$ GeV
Angular acceptance	$\lvert\eta\rvert < 2.47$, excluding $1.37 \leq \lvert\eta\rvert \leq 1.52$
Longitudinal impact parameter	$\lvert z_0 \times \sin\theta\rvert < 0.5$ mm
Transverse impact parameter	$d_0/\sigma_{d_0} < 5$
Particle identification	`MediumLH`
Fail signal identification and/or isolation cuts	

Table 5.4: Electron selection criteria. All electrons are required to pass the preselection (top), and then either the signal (middle) or loose (bottom) criteria is applied to the preselected electrons.

Jet selection	
Momentum cut	$p_{\mathrm{T}} > 30$ GeV for $2.4 < \lvert\eta\rvert < 4.5$ $p_{\mathrm{T}} > 60$ GeV for $\lvert\eta\rvert < 2.4$
JVT cut	`Medium`
Jet-lepton separation	$\Delta R(j, l) > 0.3$

Table 5.5: Jet selection criteria. All jets are required to pass the above selection in order to be used in the analysis.

Since electrons leave a shower in the EM calorimeter, every electron has a jet associated with it. Therefore, any jets close to an electron (within $\Delta R(e, j) < 0.2$) are rejected due to the high probability that they are the same object. On the other hand, when jets and electrons overlap within a large radius of $0.2 < \Delta R(e, j) < 0.4$, it is likely that the electron and jet both are part of a heavy-flavor decay, and the electron is rejected.

High energy muons can produce photons via bremsstrahlung radiation or collinear final state radiation which results in a nearby energy deposit in the calorimeters. Non-prompt muons from hadronic decays produce a similar signature; however, in this case the jet has a higher track multiplicity in the ID. It is possible to address both cases by rejecting the jet when the ID track multiplicity is less than three and otherwise rejecting the muon for jets and muons within $\Delta R(\mu, j) < 0.4$.

In addition to the case above where muon bremsstrahlung results in a nearby reconstructed jet, the ID track from the muon and the calorimeter energy deposit can lead to it bein reconstructed as an electron. In this case, if both a muon and an electron share a track in the ID, the muon is kept and the electron is rejected, unless the muon is calorimeter-tagged[5], in which case the muon is removed in favor of the electron.

Overlap	Check	Result (remove $\rightarrow$ keep)
Electron & Jet	$\Delta R(e, j) < 0.2$	Jet $\rightarrow$ electron
	$0.2 < \Delta R(e, j) < 0.4$	Electron $\rightarrow$ jet
Muon & Jet	$\Delta R(\mu, j) < 0.4$ and Jet $N_{\text{ID tracks}} < 3$	Jet $\rightarrow$ muon
	$\Delta R(\mu, j) < 0.4$ and Jet $N_{\text{ID tracks}} \geq 3$	Muon $\rightarrow$ jet
Electron & Muon	Shared ID track	Electron $\rightarrow$ muon
	Shared ID track & muon is calo-tagged	Muon $\rightarrow$ electron

Table 5.6: Summary of the overlap removal procedure used in the analysis. If the criteria in the "check" column is met, in the "result" column, the object on the left of the arrow is removed in favor of the object on the right.

5.2.2 Signal event selection

After the objects have been selected, cuts are applied on a per-event level to select $W^{\pm}W^{\pm}jj$ signal events. The event selection is summarized in Table 5.8 and is detailed in this section. It includes the results of an optimization performed using a multidimensional grid scan.

The initial event selection begins by choosing events that pass one or more of the trigger requirements listed in Table 5.7. At least one signal lepton is "matched" to a passed trigger in order

[5] A calorimeter-tagged (CT) muon is a muon that is identified by matching an ID track to a calorimeter energy deposit. CT muons have relatively low reconstruction efficiency compared to those measured by the MS, but can be used to recover acceptance in regions of the detector where the MS does not have full coverage [35].

to ensure that it was indeed a signal lepton that fired the trigger. A collection of *event cleaning* cuts must also be passed in order to remove events collected during periods in which one or more components of the detector was not operating optimally. Finally, the events are required to contain at least one interaction vertex. An event can have multiple reconstructed vertices from additional proton-proton collisions that occurred in the same bunch crossing. In this case, the *primary vertex* is determined by choosing the vertex with the largest sum of the p_{T}^2 of its associated tracks.

	2015 data	2016 data
Electrons	$p_{\mathrm{T}} > 24$ GeV and `Medium` ID $p_{\mathrm{T}} > 60$ GeV and `Medium` ID $p_{\mathrm{T}} > 120$ GeV and `Loose` ID	$p_{\mathrm{T}} > 26$ GeV and `Tight` ID and `Loose` isolation $p_{\mathrm{T}} > 60$ GeV and `Medium` ID $p_{\mathrm{T}} > 140$ GeV and `Loose` ID
Muons	$p_{\mathrm{T}} > 20$ GeV and `Loose` isolation $p_{\mathrm{T}} > 50$ GeV	$p_{\mathrm{T}} > 26$ GeV and `Medium` isolation $p_{\mathrm{T}} > 50$ GeV

Table 5.7: Summary of trigger requirements for electrons and muons for $\sqrt{s} = 13$ TeV data collected in 2015 and 2016. At least one of the triggers must be satisfied.

Events are then required to contain exactly two signal leptons with the same electric charge. The dilepton pair must have a combined invariant mass of $m_{ll} \geq 20$ GeV in order to suppress low mass Drell-Yan backgrounds. Two additional selections are applied to events in the ee-channel: both electrons are required to have $|\eta| < 1.37$ with an invariant mass at least 15 GeV away from the Z-boson mass to reduce events where one electron is reconstructed with the wrong charge (this background will be discussed in more detail in Section 5.3 TODO: Replace with proper subsection once it's written). To suppress backgrounds from events with more than two leptons, events with more than two leptons passing the preselection are vetoed.

Missing transverse energy ($E_{\mathrm{T}}^{\mathrm{miss}}$) represents any particles that escape the detector without being measured, such as neutrinos, and is defined as the magnitude of the vector sum of transverse momenta of all reconstructed objects. It can be difficult to calculate accurately, as it involves measurements from all subsystems within the detector, and it is sensitive to any corrections that may be applied to the reconstructed physics objects [42]. These corrections, including the momentum smearing for muons, energy scale and smearing for electrons, and jet calibrations, are propagated to the $E_{\mathrm{T}}^{\mathrm{miss}}$ calculation. Events are required to contain $E_{\mathrm{T}}^{\mathrm{miss}} > 30$ GeV in order to account for the two neutrinos from the W boson decays.

At least two jets are required. The leading and subleading jets must have $p_{\mathrm{T}} > 65$ GeV and $p_{\mathrm{T}} > 35$ GeV, respectively, and are referred to as the *tagging jets*. Events are vetoed if they contain one or more jets that have been tagged as a b-jet to suppress backgrounds from heavy flavor decays (especially top quark events). The b-tagging algorithm used by ATLAS is a boosted decision tree (BDT) called MV2c10, and this analysis uses a workingpoint with 85% efficiency [43].

Finally, cuts are applied on the VBS signature outlined in Section 5.0.2. The tagging jets are required to have a dijet invariant mass $m_{jj} > 200$ GeV and be separated in rapidity by $|\Delta y_{jj}| > 2.0$. This preferentially selects the VBS EWK events over the QCD-produced $W^{\pm}W^{\pm}jj$ events.

Event selection	
Event preselection	Pass at least one trigger with a matched lepton Pass event cleaning At least one reconstructed vertex
Lepton selection	Exactly two leptons passing signal selection Both signal leptons with the same electric charge $\|\eta\| < 1.37$ and $\|M_{ee} - M_Z\| > 15$ GeV (ee-channel only) Veto events with more than two preselected leptons
Missing transverse energy	$E_{\mathrm{T}}^{\mathrm{miss}} \geq 30$ GeV
Jet selection	At least two jets Leading jet $p_{\mathrm{T}} > 65$ GeV Subleading jet $p_{\mathrm{T}} > 35$ GeV $m_{jj} > 200$ GeV $N_{b\text{-jet}} = 0$ $\|\Delta y_{jj}\| > 2.0$

Table 5.8: The signal event selection

5.3 Background estimations

The major sources of background events are summarized in Section 5.0.3, and the methods used to estimate them are detailed in this section. Prompt backgrounds from ZZ and $t\bar{t}V$ are estimated directly from MC simulations. The shape of the WZ and $V\gamma$ backgrounds are taken from MC, and the predicted yeilds are normalized to the data predictions in dedicated control regions, as outlined in Sections 5.3.1 and 5.3.2, respectively. Opposite sign events with a charge misidentified electron are estimated by a data-driven background method which is summarized in Section 5.3.3. Finally, a *fake factor* method is used to estimate the contributions from non-prompt backgrounds and is the subject of Section 5.3.4.

5.3.1 Estimation of the WZ background

The dominant background involving prompt leptons comes from WZ+jets events. The contribution is estimated from MC simulation and normalized to data in a control region enriched in WZ events defined by the same event selection as Table 5.8 for the signal region, with the following changes applied to increase the purity of the WZ process:

- The third lepton veto is inverted, requiring a third lepton with $p_{\mathrm{T}} > 15$ GeV
- Two of the leptons must make a same-flavor opposite-sign pair. If more than one pair exists, the one with m_{ll} closest to the Z boson mass is chosen.
- The trilepton invariant mass is required to be $m_{lll} > 106$ GeV to reduce contributions from $Z\gamma$ and Z+jets

Once the event yields in the control region are calculated, they are propagated to the final signal region fit, detailed in Section 5.4 TODO: update reference with proper subsection once it's written, in a single bin combining all the lepton channels. The systematic uncertainties of the WZ background are also calculated at this time. The event yields for the WZ control region are listed in Table 5.9, and distributions of the leading lepton p_{T} and η as well as trilepton invariant mass m_{lll} are found in Figures 5.10 and 5.9, respectively.

Event yields in the WZ control region	
WZ	197.9 ± 1.4
ZZ	14.1 ± 0.3
Triboson	1.26 ± 0.1
top	10.8 ± 1.1
$Z\gamma$	3.1 ± 1.1
Z+jets	2.5 ± 1.4
Total prediction	229.7 ± 2.5
Data	201 ± 14.2

Table 5.9: Event yields in the WZ control region before normalization. All lepton flavor channels are combined.

5.3.2 Estimation of the $V\gamma$ background

Events from $V\gamma$ processes can pass selection if the photon converts into an e^+e^- pair and one of the electrons passes the selection criteria. The background is estimated from MC simulations which are then scaled by a normalization factor calculated from a control region enriched in $Z(\mu^+\mu^-)\gamma$ events. This control region selects two opposite-sign muons and an additional electron that is assumed to come from the photon conversion. The full event selection is detailed in Table 5.10.

The $Z\gamma$ MC samples available do not cover the full range of p_{T}^{γ} and $\Delta R(\gamma, l)$; thus, additional Drell-Yan samples (Z+jets) are used to fill out the phase space. Overlap between the two samples

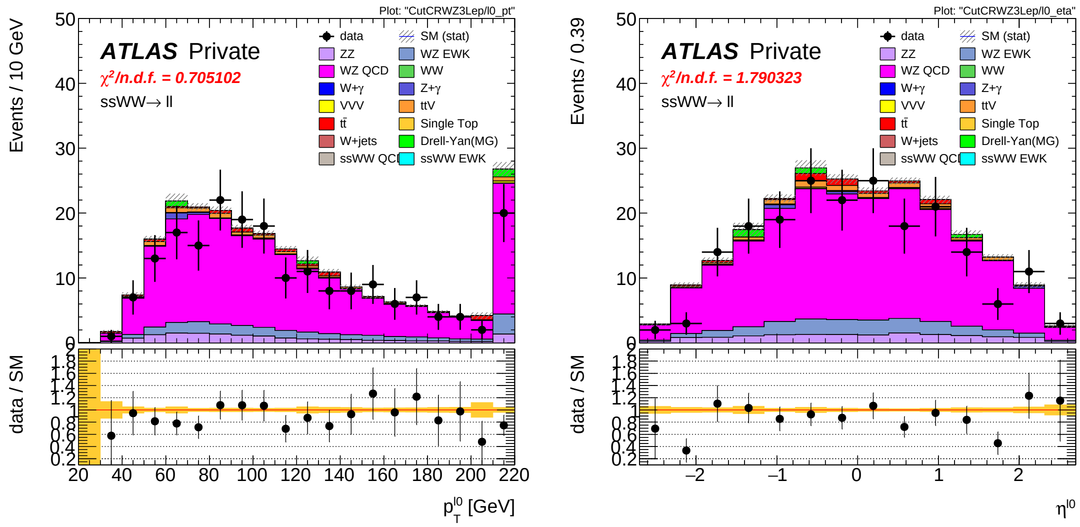

Figure 5.9: Leading lepton p_{T} (left) and η (right) distributions in the WZ control region before normalization. All lepton channels are combined.

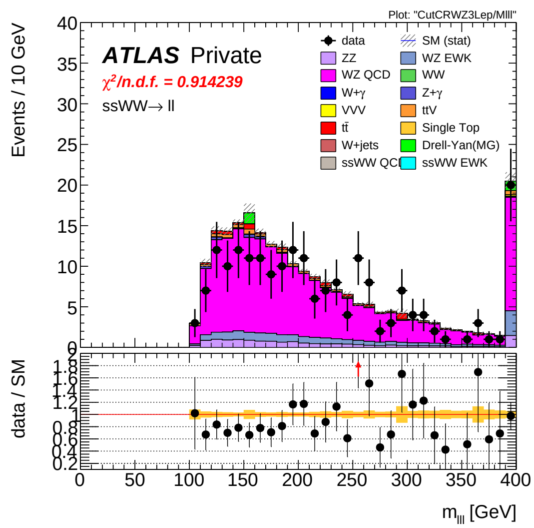

Figure 5.10: Trilepton invariant mass m_{lll} distribution in the WZ control region before normalization. All lepton channels are combined.

$V\gamma$ control region
Exactly two muons with $p_{\mathrm{T}} > 27$ GeV and $p_{\mathrm{T}} > 20$ GeV
Exactly one additional electron with $p_{\mathrm{T}} > 15$ GeV
Remove overlap between Z+jets and $Z\gamma$
Di-muon + photon invariant mass $75 < M_{\mu\mu\gamma} < 100$ GeV
$E_{\mathrm{T}}^{\mathrm{miss}} < 30$ GeV

Table 5.10: Selection criteria for the $V\gamma$ control region.

are removed based to avoid double counting. Events with final state photons at truth level are checked to ensure that the photon did not originate from a hadronic decay. Cuts on $p_{\mathrm{T}}^{\gamma} > 10$ GeV and $\Delta R(\gamma, l) > 0.1$ are then applied at generator level, and $Z\gamma$ events that fail and Z+jets events that pass this additional selection are removed.

The normalization factor is calculated directly from the event yields in the $V\gamma$ control region rather than in the signal fit, as is done for the WZ background. The event yields are listed in Table 5.11, and the normalization factor is determined to be 1.77. No MC events from $Z\gamma$ processes survive the full event selection; thus, the scaling is only applied to the $W\gamma$ background in the signal region. A systematic uncertainty of 44% is assigned to the background based off of the uncertainties in the calculation of the normalization factor.

Event yields in the $V\gamma$ control region	
$Z\gamma$	24.6 ± 3.3
Z+jets	3.0 ± 1.5
diboson + triboson	6.7 ± 0.3
top	1.5 ± 0.5
Total prediction	35.8 ± 3.7
Data	57 ± 7.6

Table 5.11: Event yields in the $V\gamma$ control region. The $V\gamma$ scale factor of 1.77 is calculated by scaling up the $Z\gamma$ and Z+jets backgrounds to account for the difference between the data and predicted total background.

5.3.3 Estimation of backgrounds from charge misidentification

If an electron's charge is mis-reconstructed, it can lead to a real, opposite-sign lepton pair passing the same-sign requirement in the event selection. There are two primary reasons this can occur:

1. An electron emits a photon via bremsstrahlung which then converts into an electron-positron pair, and the conversion track with the wrong electric charge is matched to the original electron. This is the dominant process leading to charge flip, and it is highly dependent on the electron η due to the different amount of detector material the electron passes through.

2. The curvature of the electron's track is mismeasured, resulting in the wrong charge being assigned. This process is dependent on the momentum of the electron, as its track becomes more straight as the momentum of the electron increases.

In order to estimate this background, the rate at which an electron's charge is misidentified is calculated from $Z \to e^+e^-$ MC simulation. It is known that the MC does not perfectly model

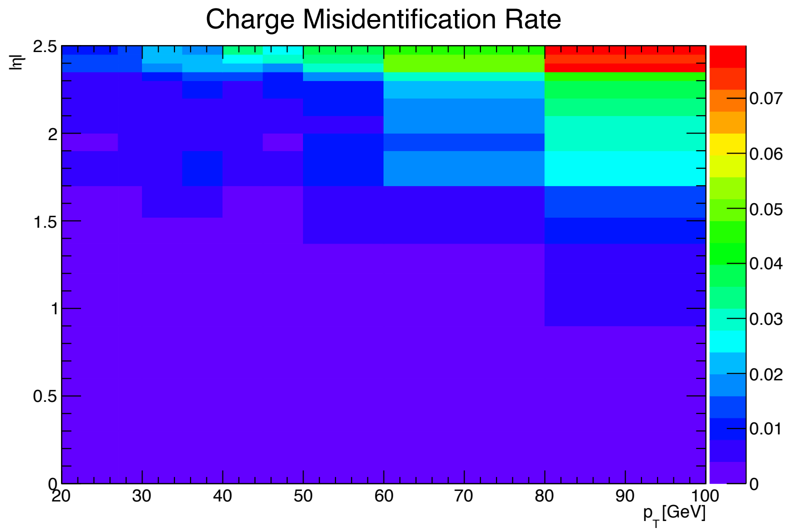

Figure 5.11: Charge misidentification rates for electrons as a function of $|\eta|$ and p_{T}. Rates are calculated from $Z \to e^+e^-$ MC after applying sacle factors to approximate the charge mis-ID rates in data.

the material effects leading to charge flip; as a result, scale factors are applied to the MC in order for it to to better reflect the real performance. These scale factors are obtained from the ratio of charge mis-ID rates in data and uncorrected MC in [10] following the method outlined in [44]. Once the scale factors are applied, the charge misidentification rate ε can be extracted by comparing the electron's reconstructed charge with the charge of its truth particle:

$$\varepsilon(\eta, p_{\mathrm{T}}) = \frac{N_{\text{wrong charge}}}{N_{\text{prompt electrons}}} \tag{5.1}$$

The charge mis-ID rate is calculated in bins of electron $|\eta|$ and p_{T} and varies from below 0.1% in the central region of the detector up to 8% in the forward regions for high p_{T} (above 90 GeV) electrons. A two-dimensional plot of ε can be found in Figure 5.11.

Given the charge flip rate $\varepsilon(\eta, p_{\mathrm{T}})$, the rate at which an electron has its charge correctly reconstructed is $(1-\varepsilon)$. Thus there are three possible combinations of charge identification, assuming a two-electron event:

1. Both electrons are reconstructed correctly: $(1-\varepsilon)^2$
2. Both electrons are mis-reconstructed: ε^2
3. Only one electron is mis-reconstructed: $2\varepsilon(1-\varepsilon)$

In order to estimate the size of the background from charge misidentification, opposite-sign events are selected using the default event selection for a given signal or control region with the same-sign requirement inverted. These events are then weighted by the probability for one of the electrons to be reconstructed with the wrong charge:

$$\omega = \frac{\varepsilon_1(1-\varepsilon_2) + \varepsilon_2(1-\varepsilon_1)}{(1-\varepsilon_1)(1-\varepsilon_2) + \varepsilon_1\varepsilon_2} \tag{5.2}$$

where the subscripts 1 and 2 refer to the leading and subleading electrons, respectively, and ε_i is a function of the η and p_{T} of the i^{th} electron. In the case of an event with only one electron and one muon, Equation 5.2 simplifies:

$$\omega = \frac{\varepsilon}{1-\varepsilon} \tag{5.3}$$

This method assumes that there is little contamination from fake electrons in the opposite-sign sample, and this has been verified with MC simulation.

Additionally, charge-flipped electrons tend to be reconstructed with lower energy when compared to electrons with the correct charge. This is due to energy loss from the material interactions that can cause the charge to be misidentified. A correction factor is calculated from MC simulations, comparing the p_{T} of the truth electron to its reconstructed counterpart:

$$\alpha = \frac{\left(\frac{p_{\mathrm{T}}^{\mathrm{reco}}}{p_{\mathrm{T}}^{\mathrm{truth}}} - 1\right)_{\text{correct charge}}}{\left(\frac{p_{\mathrm{T}}^{\mathrm{reco}}}{p_{\mathrm{T}}^{\mathrm{truth}}} - 1\right)_{\text{wrong charge}}} \tag{5.4}$$

The correction is then applied to the p_{T} of the charge-flipped electron via

$$p_{\mathrm{T}} = p_{\mathrm{T}}^{0}/(1+\alpha) + dE \tag{5.5}$$

where p_{T}^{0} is the uncorrected p_{T} of the electron and dE is a gaussian smearing factor centered at zero with a width related to the energy resolution. Since which electron is misreconstructed is never determined in this method, in the case of a two-electron event, the energy correction is applied randomly to one of the two electrons based on the probabilities for them to be charge-flipped. This also determines the overall sign of the event; the charge of the electron that does not recieve the correction is taken to be the charge for both.

Systematic uncertainties on the charge mis-ID rates are calculated by generating two additional sets of rates with the uncertainties on the scale factors varied up and down. The size of the estimated charge flip background without the energy correction applied is also taken as a systematic uncertainty. These systematic uncertainties are estimated to be approximately $\pm 15\%$.

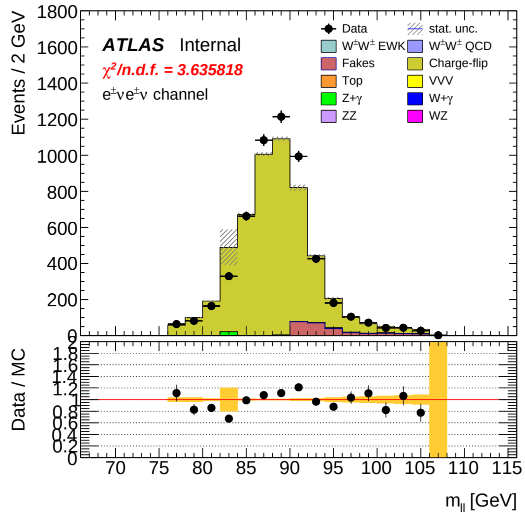

Figure 5.12: Dilepton invariant mass distribution m_{ll} for the ee channel in the same-sign inclusive VR.

5.3.3.1 Validation of the charge misidentification estimate

The performance of the charge misidentification estimation is tested in the same-sign inclusive validation region (VR), defined in Table 5.12. For ee events, the mass of the dilepton pair is required to lie within 15 GeV of the Z boson mass to increase the purity of the charge flip background. $t\bar{t}$ production, which can contribute to both the charge mis-ID and fake lepton backgrounds, is suppressed by the b-jet veto. The di-electron invariant mass is shown in Figure 5.12, and distributions of the leading and subleading electron p_{T} in the ee-channel are shown in Figure 5.13 with the Z mass cut inverted. Agreement between data and prediction is seen within the total statistical and systematic uncertainties in the VR.

Same-sign inclusive VR
Exactly 2 same-sign signal leptons
$p_{\mathrm{T}} > 27$ GeV for both leptons
$m_{ll} > 20$ GeV
$\lvert m_{ee} - m_Z \rvert > 15$ GeV ($e^{\pm}e^{\pm}$-channel only)
$N_{b\text{-jet}} = 0$

Table 5.12: Selection criteria for the same-sign inclusive validation region.

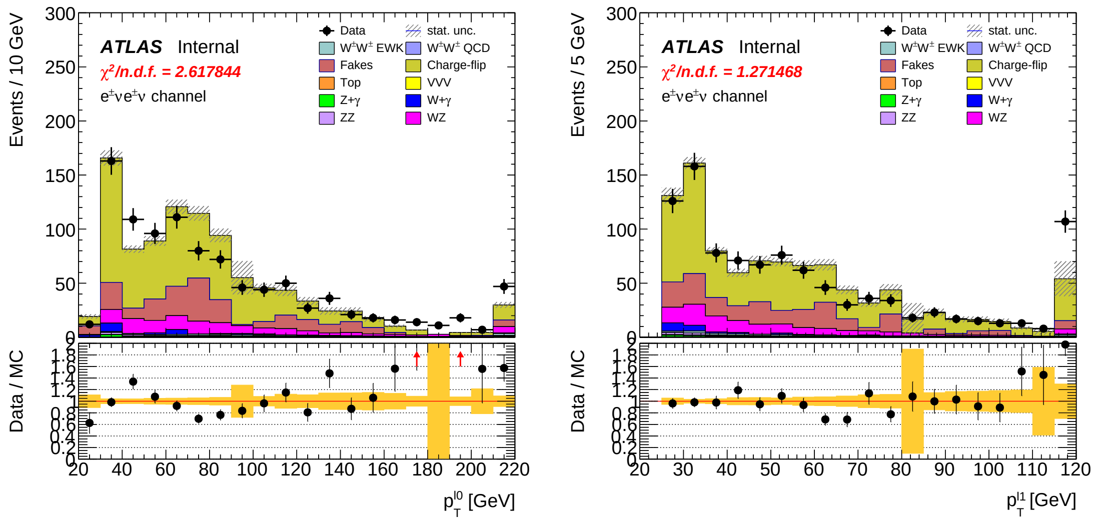

Figure 5.13: p_{T} distributions for the leading (left) and subleading (right) electron for the ee channel in the same-sign inclusive VR. In these plots, the cut requiring m_{ee} to fall within the Z mass window has been inverted in order to test the modelling away from the Z peak.

5.3.4 Estimation of non-prompt backgrounds with the fake factor method

Events with one prompt lepton produced in asociation with hadronic jets can pass the event selection if a jet is misidentified as a charged lepton or if a non-prompt lepton from the decay of a heavy flavor particle (such as b- and c-hadrons) passes the signal lepton criteria. These misidentified jets and non-prompt leptons are collectively referred to as *fake leptons*, or simply *fakes*. The rate at which a fake lepton is misidentified is generally not modelled well enough by the MC to accurately estimate their contributions directly from simulation. Therefore, a data-driven technique called the *fake factor* is used to estimate the size and shape of background processes from fake leptons. In this analysis, a new modification to the fake factor is used involving the particle isolation variables; the method is outlined in the context of the *default* fake factor in Section 5.3.4.1, and the modified fake factor is outlined in Section 5.3.4.2.

5.3.4.1 Overview of the default fake factor method

The goal of the fake factor method is to measure the fake rate from real collision events in a region enriched in fake leptons and use it to estimate the size of the fake lepton background in a chosen signal or control region. This is done by creating two samples using different lepton definitions:

1. The *nominal* sample is made up of leptons passing the signal selection.

2. The *loose* sample is made up of leptons that fail the signal selection while still passing a loosened set of criteria. This sample is enriched in fake leptons and is orthogonal to the set of signal leptons.

Using the sets of nominal and loose leptons, a fake factor f can be calculated in a region enriched in processes that are prone to producing fake leptons:

$$f = \frac{N_{\text{nominal}}}{N_{\text{loose}}} \tag{5.6}$$

Since the fake rate is not expected to be constant over the entire phase space, the fake factor can be divided into bins:

$$f(b) = \frac{N_{\text{nominal}}(b)}{N_{\text{loose}}(b)} \tag{5.7}$$

where b represents the bin number. In this analysis, the fake factor is binned in lepton p_{T}.

In order to estimate the fake background contribution in a given signal or control region, the fake factor is applied to a second control region with a selection identical to the region of interest with one of the leptons required to satisfy the loose criteria. The region for which the background is estimated contains two nominal leptons and is referred to as *nominal+nominal* (NN), and the associated control region where the fake factor is applied contains one nominal and one loose lepton and is referred to as *nominal+loose* (NL). The fake background in a NN region can then be calculated as:

$$N_{NN}^{\text{fake bkg.}} = \sum_b f(b) N_{NL}(b) \tag{5.8}$$

Backgrounds containing two prompt leptons can also enter the NL region if one of the leptons passes the nominal selection and the other passes the loose selection. Since the fake factor method estimates the fake background by scaling the amount of non-prompt events in the NL region, if these prompt contributions are not be removed, they will be included in the scaling and the background will be overpredicted. The final estimate of the fake background becomes:

$$N_{NN}^{\text{fake bkg.}} = \sum_b f(b)\big(N_{NL}(b) - N_{NL}^{\text{prompt}}(b)\big) \tag{5.9}$$

5.3.4.2 The fake factor with $p_{\mathrm{T}}^{\mathbf{cone}}$

When a jet produces a non-prompt lepton, that lepton only carries a fraction of the underlying jet's total momentum. Due to the isolation cut applied to the nominal leptons, they typically carry a much larger percentage of the underlying jet momentum[6] than the loose leptons (which are allowed to fail this criteria).

This discrepancy in the underlying jet momentum fraction can cause problems in the calculation of the fake factor f. Consider the case where two separate events have jets of identical momentum, but one produces a non-prompt lepton that passes the nominal selection, and the other produces a non-prompt lepton that passes the loose selection. The loose lepton on average will have lower p_{T} than the nominal lepton despite both originating from jets with the same momentum. This can be seen explicitly when comparing the p_{T} of a muon to its associated truth jet:

$$\Delta p_{\mathrm{T}}(\mu, j) = \frac{p_{\mathrm{T}}(j) - p_{\mathrm{T}}(\mu)}{p_{\mathrm{T}}(j) + p_{\mathrm{T}}(\mu)} \tag{5.10}$$

Since muons are not included in the jet reconstruction algorithm, Δp_{T} approximates the momentum of the muon compared to the rest of the jet. For muons that carry more than 50% of the jet's momentum, Δp_{T} will be negative and vice-versa. The Δp_{T} distributions for nominal and loose muons in $t\bar{t}$ MC events is shown Figure 5.14, where a 50 GeV jet on average corresponds to a 35 GeV nominal muon and a 20 GeV loose muon[7].

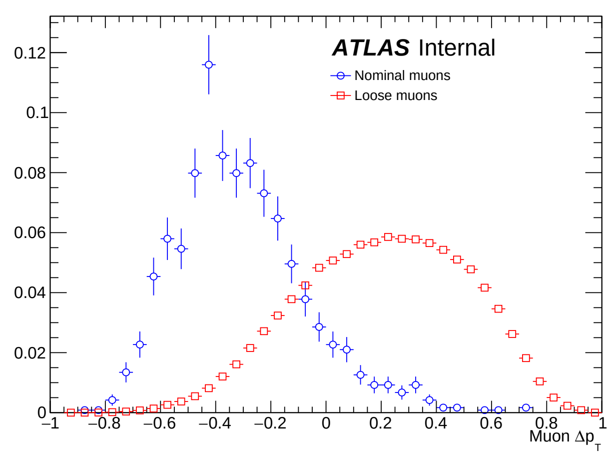

Figure 5.14: Δp_{T} distributions for nominal (blue) and loose (red) muons in simulated $t\bar{t}$ events. Each muon has been matched to a truth-level jet. Both distributions are normalized to unit area.

Since the default fake factor defined in Equation 5.7 is binned in lepton p_{T}, within a given bin,

[6] Since the isolation variables are a measure of detector activity around the lepton, if other nearby particles carried a significant portion of the jet's momentum, the lepton would likely fail this cut.

[7] To better illustrate the point, here the muon is added back into the jet p_{T}, and the corresponding muon p_{T} is obtained via $\Delta p_{\mathrm{T}}(\mu, j) = \frac{\left(p_{\mathrm{T}}(j) - p_{\mathrm{T}}\mu\right) - p_{\mathrm{T}}(\mu)}{\left(p_{\mathrm{T}}(j) - p_{\mathrm{T}}(\mu)\right) + p_{\mathrm{T}}(\mu)} = \frac{p_{\mathrm{T}}(j) - 2p_{\mathrm{T}}(\mu)}{p_{\mathrm{T}}(j)}$.

the underlying jet p_{T} spectrum can differ substantially between the numerator and the denominator. Additionally, these differences can vary depending on the process producing the non-prompt leptons or on the specific kinematic selections of the signal or control regions where the fake factor is applied.

Fortunately, the majority of the jet momentum not carried by the non-prompt lepton (excluding neutrinos) can be recovered using isolation variables. A track-based isolation is chosen, referred to as $p_{\mathrm{T}}^{\mathrm{cone}}$, and it contains the sum of the p_{T} of all particle tracks originating from the primary vertex within a cone of $\Delta R < 0.3$ around the lepton. Thus, the sample of loose leptons in the denominator of the fake factor calculation is binned in $p_{\mathrm{T}} + p_{\mathrm{T}}^{\mathrm{cone}}$ rather than simply lepton p_{T}. Adding the isolation cone greatly reduces the difference in the fraction of the underlying jet momentum carried by the nominal and loose leptons. To check this, a new Δp_{T} is calculated between a lepton and its matched truth jet, where the truth jet p_{T} has been corrected to include all muons within a cone of $\Delta R < 0.4$:

$$p_{\mathrm{T}}(j) = p_{\mathrm{T}}(j_{\mathrm{truth}}) + \sum_{\Delta R < 0.4} p_{\mathrm{T}}(\mu_{\mathrm{truth}}) \tag{5.11}$$

The Δp_{T} distributions comparing p_{T} and $p_{\mathrm{T}}+p_{\mathrm{T}}^{\mathrm{cone}}$ for nominal and loose leptons using the corrected jet p_{T} are found in Figure 5.15, and better agreement is seen between the numerator (nominal) and denominator (loose with $p_{\mathrm{T}} + p_{\mathrm{T}}^{\mathrm{cone}}$) distributions.

The numerator remains binned in lepton p_{T}, due to the fact that it is meant to mirror the signal region as closely as possible, and the signal lepton selection does not use $p_{\mathrm{T}} + p_{\mathrm{T}}^{\mathrm{cone}}$. The impact of this is expected to be negligible due to the $p_{\mathrm{T}}^{\mathrm{cone}}$ isolation being small for signal leptons, as shown for muons in Figure 5.16. Finally, the fake factor f becomes:

$$f(b) = \frac{N_{\mathrm{nominal}}\big(b(p_{\mathrm{T}})\big)}{N_{\mathrm{loose}}\big(b(p_{\mathrm{T}} + p_{\mathrm{T}}^{\mathrm{cone}})\big)} \tag{5.12}$$

5.3.4.3 Application of the fake factor

The fake factor itself is measured from a sample data events passing a dijet selection requiring exactly one lepton (either passing the nominal or loose selections) and at least one jet. The leading jet must also be b-tagged and approximately back-to-back with the lepton in order to enhance non-prompt lepton contributions while reducing contributions from processes involving W and Z bosons. W boson events are further suppressed by requiring the sum of the $E_{\mathrm{T}}^{\mathrm{miss}}$ and the transverse mass of the lepton and $E_{\mathrm{T}}^{\mathrm{miss}}$ to be less than 50 GeV. The full event selection for the dijet region is summarized in Table 5.13.

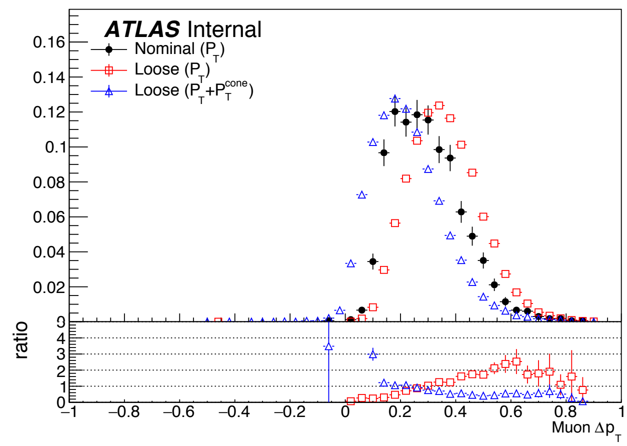

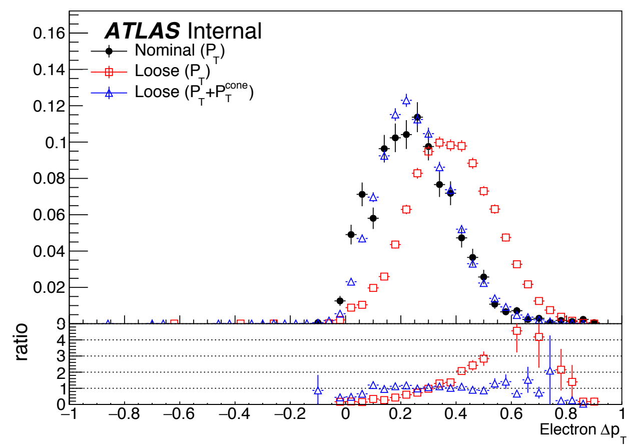

Figure 5.15: Δp_{T} distributions for muons (top) and electrons (bottom) in simulated $t\bar{t}$ events. Each lepton has been matched to a truth-level jet, and that truth jet has had its p_{T} corrected to include all truth muons within a cone of $\Delta R < 0.4$. The nominal leptons are in black. Δp_{T} is calculated for the loose leptons using p_{T} (red) and $p_{\mathrm{T}} + p_{\mathrm{T}}^{\mathrm{cone}}$ (blue).

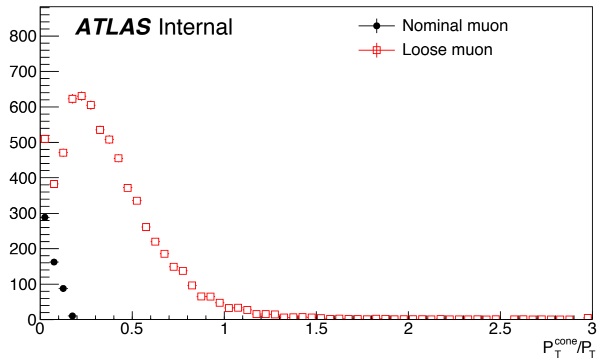

Figure 5.16: Distributions of $p_{\mathrm{T}}^{\mathrm{cone}}/p_{\mathrm{T}}$ for nominal (black) and loose (red) muons in simulated $t\bar{t}$ events.

Dijet event selection
Event preselection
Exactly one lepton with $p_{\mathrm{T}} > 15$ GeV
$N_{\mathrm{jet}} > 0$
Leading jet is b-tagged
$p_{\mathrm{T}}^{\mathrm{lead.\ jet}} > 25$ GeV
$p_{\mathrm{T}}^{\mathrm{lead.\ jet}} > 30$ GeV if $\lvert\eta_j\rvert > 2.5$
$\lvert\Delta\phi(l, \mathrm{lead.\ jet})\rvert > 2.8$
$m_{\mathrm{T}}(l, E_{\mathrm{T}}^{\mathrm{miss}}) + E_{\mathrm{T}}^{\mathrm{miss}} < 50$ GeV

Table 5.13: Event selection for the dijet region used for calculating the fake factor. The selected lepton can pass either the nominal (signal) or loose selections. In the case of the nominal leptons, the $p_{\mathrm{T}} > 27$ GeV requirement is replaced with $p_{\mathrm{T}} > 15$ GeV.

The numerator sample is constructed from dijet events in which the lepton passes the nominal (signal) selection and is binned in the lepton p_{T}. Similarly, the denominator sample is made up of the remaining dijet events where the lepton passes the loose selection and is binned in the lepton $p_{\mathrm{T}} + p_{\mathrm{T}}^{\mathrm{cone}}$. The nominal and loose leptons pass the signal selection[8] and loose selection, respectively, defined earlier in Table 5.3 for muons and Table 5.4 for electrons. Backgrounds from W+jets, Z+jets, $t\bar{t}$, and single top processes are estimated from MC simulations requiring one lepton to be prompt using the truth information; these contributions are subtracted from the dijet data. The fake factor is then calculated using Equation 5.12 for muons and for central and forward electrons separately. The muon fake factor is shown in Figure 5.17, and the two electron fake factors are shown in Figure 5.18. The numerical values of the fake factors, including their systematic uncertainties which

[8]The $p_{\mathrm{T}} > 27$ GeV cut in the signal lepton selection is dropped in favor of the $p_{\mathrm{T}} > 15$ GeV requirement in the dijet selection.

will be discussed in Section 5.3.4.4, are listed in Table 5.14.

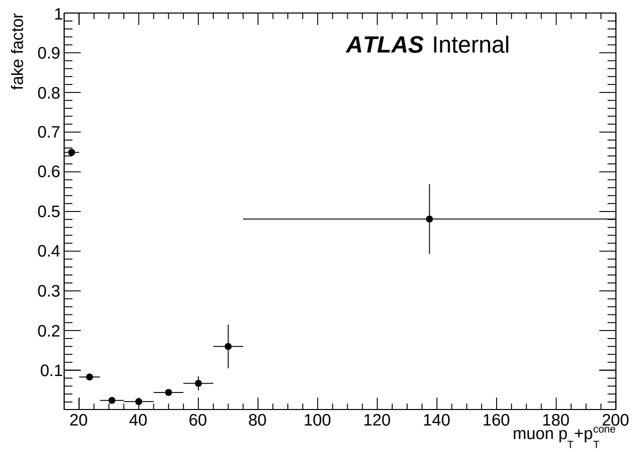

Figure 5.17: The measured fake factor as a function of muon $p_{\mathrm{T}} + p_{\mathrm{T}}^{\mathrm{cone}}$. The error bars represent the statistical uncertainty only.

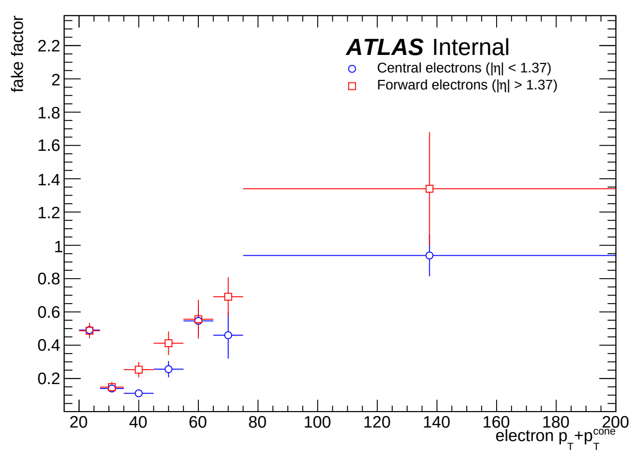

Figure 5.18: The measured fake factor as a function of electron $p_{\mathrm{T}} + p_{\mathrm{T}}^{\mathrm{cone}}$ in the central ($|\eta| < 1.37$, blue) and forward ($|\eta| > 1.37$, red) regions of the detector. The error bars represent the statistical uncertainty only.

In order to properly account for the denominator being binned in $p_{\mathrm{T}} + p_{\mathrm{T}}^{\mathrm{cone}}$, special care needs to be taken when estimating the fake background from the NL regions. For the purposes of the fake factor calculation, it is perhaps more intuitive to consider a loose *object* with $p_{\mathrm{T}} = p_{\mathrm{T}} + p_{\mathrm{T}}^{\mathrm{cone}}$ instead of simply a loose *lepton*, as the lepton and the underlying jet are treated as a whole with this method. When the lepton p_{T} cuts required by a particular signal or control region are applied to nominal and loose leptons, the cut is applied to the p_{T} of the nominal lepton and to the $p_{\mathrm{T}} + p_{\mathrm{T}}^{\mathrm{cone}}$ of the loose object. Similarly, when looking up the fake factor weight for a given NL event, the value taken from the bin corresponding to the $p_{\mathrm{T}} + p_{\mathrm{T}}^{\mathrm{cone}}$ of the loose object. Finally, when applying the weight to the event, $p_{\mathrm{T}} + p_{\mathrm{T}}^{\mathrm{cone}}$ is assigned as the p_{T} of the loose object. Figure 5.19 contains a graphical representation of this procedure.

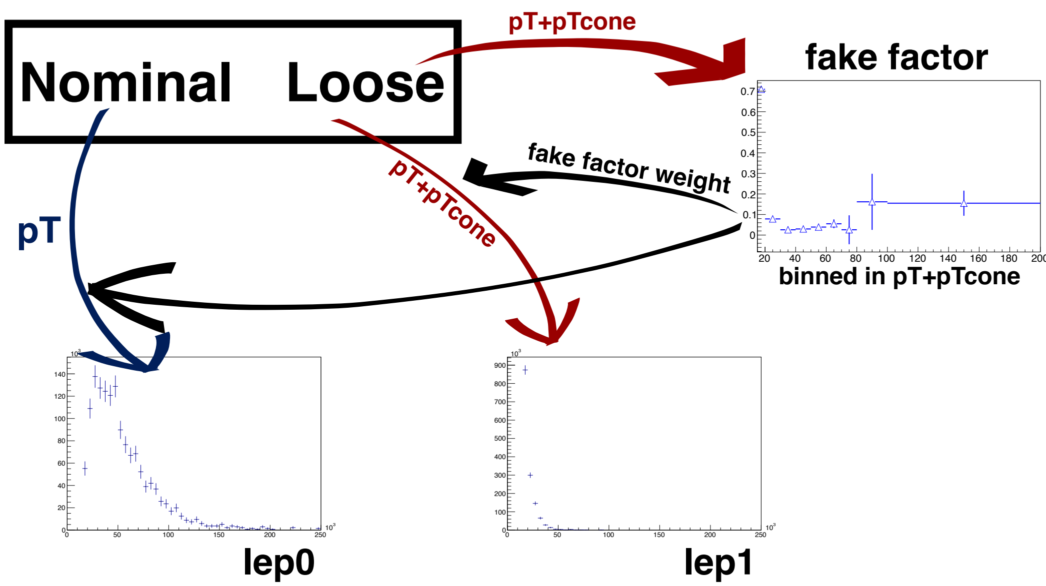

Figure 5.19: Graphical representation of the fake factor application using $p_{\mathrm{T}} + p_{\mathrm{T}}^{\mathrm{cone}}$. The value of $p_{\mathrm{T}} + p_{\mathrm{T}}^{\mathrm{cone}}$ for the loose lepton is used to "look up" the fake factor weight which is then applied to the event. The loose lepton's p_{T} becomes $p_{\mathrm{T}} + p_{\mathrm{T}}^{\mathrm{cone}}$ for the purpose of the fake background estimation.

Finally, it should be noted that the addition of $p_{\mathrm{T}}^{\mathrm{cone}}$ to the loose object may cause the loose leptons in the denominator sample to migrate into higher bins. This results in an overall decrease in the number of loose objects in the lower $p_{\mathrm{T}} + p_{\mathrm{T}}^{\mathrm{cone}}$ bins due to there not being additional leptons at lower p_{T} to replace them. Since the fake factor is a ratio of the number of events in a bin, this effect causes the first few bins of the fake factor to increase, as can be seen clearly in Figure 5.17. However, the signal and control regions (and their corresponding NL regions) contain a $p_{\mathrm{T}} > 27$ GeV cut that prevents these migrations from negatively impacting the fake estimation.

5.3.4.4 Systematic uncertainties

Four sources of systematic uncertainty are considered: the dijet event selection, the prompt background subtraction, the jet flavor composition, and residual dependence on the underlying jet p_{T} spectrum. In order to measure the impact of these systematics, new fake factors are computed with each of the systematic variations and the differences from the nominal values are taken as the uncertainty.

1. In order to estimate uncertainties due to the dijet selection, the cut on $M_{\mathrm{T}} + MET$ is varied by ± 5 GeV, $\Delta\phi(l, j)$ by ± 0.1, and the jet p_{T} cut by $+5$ GeV.

2. To estimate the systematic uncertainty on the prompt background subtraction, the MC prediction in a W+jets control region is compared to data. The discrepancy between data and MC is found to be approximately 10% [10]. Therefore, the prompt background used for the subtraction is scaled up and down by $\pm 10\%$.

3. The difference in the jet flavor composition between the dijet events and the events in the NL regions can affect the accuracy of the fake background estimation. The dijet sample is dominated by light jets, while the NL regions tend to be dominated by heavy flavor from $t\bar{t}$. To account for this, the fake factor is computed with a b-jet veto.

4. To measure any residual dependence on the underlying jet p_{T} spectrum, the leading jet p_{T} distribution is reweighted to match the p_{T} spectrum of truth jets that produce fake leptons in MC simulations. This results in an increase in the number of nominal and loose leptons at high momentum [10].

5.3.4.5 Results of the fake factor

The fake background contribution in the signal region is estimated by applying the fake factors to the equivalent NL region using Equation 5.9, where the fake factor used corresponds to the flavor of the loose lepton in the event. As usual, the prompt background is subtracted from the NL events using MC simulation. Charge misidentification is handled using the same method as in Section 5.3.3, with an additional set of charge flip rates calculated for loose leptons. The fake background yields in the signal region are listed in Table 5.15. An overall uncertainty of 50% is assigned to the fake background estimation in $\mu^{\pm}\mu^{\pm}$ events, and between 40% to 90% for $e^{\pm}e^{\pm}$ and $\mu^{\pm}e^{\pm}$ events, including both statistical and systematic effects.

fake factor	p_T [15, 20]	p_T[20, 27]	p_T[27, 35]	p_T[35, 45]	p_T[45, 55]	p_T[55, 65]	p_T[65, 75]	p_T[75, 200]
nominal	0.649 ± 0.007	0.083 ± 0.002	0.024 ± 0.002	0.021 ± 0.003	0.044 ± 0.007	0.067 ± 0.018	0.160 ± 0.055	0.481 ± 0.088
MT+MET	0.649 ± 0.007	0.082 ± 0.002	0.082 ± 0.002	0.020 ± 0.003	0.045 ± 0.007	0.068 ± 0.018	0.207 ± 0.062	0.523 ± 0.086
	0.648 ± 0.007	0.083 ± 0.003	0.024 ± 0.002	0.022 ± 0.004	0.044 ± 0.007	0.054 ± 0.020	0.207 ± 0.060	0.389 ± 0.081
$\Delta\phi(\ell, j)$	0.645 ± 0.008	0.083 ± 0.003	0.024 ± 0.002	0.021 ± 0.004	0.045 ± 0.008	0.064 ± 0.021	0.064 ± 0.058	0.438 ± 0.092
	0.646 ± 0.006	0.083 ± 0.002	0.024 ± 0.002	0.020 ± 0.003	0.043 ± 0.006	0.076 ± 0.017	0.174 ± 0.050	0.448 ± 0.078
Jet p_T	0.650 ± 0.007	0.083 ± 0.002	0.024 ± 0.002	0.021 ± 0.003	0.045 ± 0.007	0.069 ± 0.018	0.159 ± 0.018	0.481 ± 0.088
$N_{\text{b-jet}} = 0$	0.724 ± 0.003	0.094 ± 0.001	0.035 ± 0.001	0.025 ± 0.002	0.022 ± 0.004	0.060 ± 0.015	0.026 ± 0.053	0.044 ± 0.134
Bkg. subtraction	0.648 ± 0.007	0.083 ± 0.002	0.024 ± 0.002	0.019 ± 0.003	0.037 ± 0.007	0.044 ± 0.019	0.096 ± 0.062	0.370 ± 0.082
	0.649 ± 0.007	0.083 ± 0.002	0.025 ± 0.002	0.022 ± 0.003	0.050 ± 0.007	0.090 ± 0.017	0.224 ± 0.052	0.591 ± 0.099
Jet p_T Reweight	0.539 ± 0.077	0.093 ± 0.007	0.025 ± 0.004	0.043 ± 0.019	0.063 ± 0.014	0.085 ± 0.025	0.141 ± 0.110	1.962 ± 0.492

(a) Fake factor for muons.

fake factor	p_T[20, 27]	p_T[27, 35]	p_T[35, 45]	p_T[45, 55]	p_T[55, 65]	p_T[65, 75]	p_T[75, 200]
nominal	0.491 ± 0.031	0.140 ± 0.020	0.111 ± 0.023	0.256 ± 0.049	0.546 ± 0.091	0.460 ± 0.140	0.939 ± 0.125
MT+MET	0.493 ± 0.030	0.138 ± 0.019	0.115 ± 0.022	0.261 ± 0.045	0.559 ± 0.084	0.656 ± 0.091	0.802 ± 0.016
	0.488 ± 0.032	0.137 ± 0.020	0.110 ± 0.025	0.283 ± 0.053	0.503 ± 0.097	0.351 ± 0.149	1.117 ± 0.255
$\Delta\phi(\ell, j)$	0.489 ± 0.035	0.134 ± 0.021	0.105 ± 0.025	0.224 ± 0.048	0.593 ± 0.093	0.356 ± 0.144	0.928 ± 0.177
	0.506 ± 0.029	0.140 ± 0.018	0.111 ± 0.022	0.260 ± 0.046	0.545 ± 0.084	0.546 ± 0.120	0.882 ± 0.103
Jet p_T	0.493 ± 0.032	0.146 ± 0.021	0.115 ± 0.024	0.259 ± 0.049	0.550 ± 0.091	0.460 ± 0.140	0.939 ± 0.125
$N_{\text{b-jet}} = 0$	0.387 ± 0.009	0.130 ± 0.008	0.321 ± 0.012	0.473 ± 0.015	0.716 ± 0.180	0.716 ± 0.180	0.716 ± 0.180
Bkg. subtraction	0.488 ± 0.031	0.138 ± 0.020	0.106 ± 0.023	0.248 ± 0.049	0.529 ± 0.092	0.434 ± 0.143	0.888 ± 0.115
	0.493 ± 0.031	0.142 ± 0.020	0.115 ± 0.023	0.264 ± 0.049	0.563 ± 0.090	0.485 ± 0.136	0.989 ± 0.132
Jet p_T Reweight	0.445 ± 0.055	0.137 ± 0.037	0.065 ± 0.023	0.115 ± 0.033	0.603 ± 0.047	0.104 ± 0.105	0.299 ± 0.260

(b) Fake factor for central electrons ($|\eta| < 1.37$).

fake factor	p_T[20, 27]	p_T[27, 35]	p_T[35, 45]	p_T[45, 55]	p_T[55, 65]	p_T[65, 75]	p_T[75, 200]
nominal	0.487 ± 0.046	0.148 ± 0.031	0.253 ± 0.046	0.412 ± 0.071	0.556 ± 0.117	0.691 ± 0.117	1.340 ± 0.340
MT+MET	0.483 ± 0.045	0.152 ± 0.031	0.241 ± 0.043	0.443 ± 0.070	0.565 ± 0.106	0.668 ± 0.117	1.075 ± 0.189
	0.495 ± 0.047	0.156 ± 0.033	0.271 ± 0.052	0.364 ± 0.074	0.664 ± 0.107	0.749 ± 0.056	0.885 ± 0.084
$\Delta\phi(\ell, j)$	0.471 ± 0.051	0.158 ± 0.035	0.247 ± 0.051	0.474 ± 0.085	0.283 ± 0.107	0.546 ± 0.149	1.189 ± 0.266
	0.478 ± 0.042	0.170 ± 0.031	0.274 ± 0.046	0.389 ± 0.066	0.645 ± 0.104	0.757 ± 0.102	1.319 ± 0.326
Jet p_T	0.523 ± 0.048	0.149 ± 0.033	0.235 ± 0.045	0.429 ± 0.073	0.555 ± 0.117	0.691 ± 0.117	1.340 ± 0.340
$N_{\text{b-jet}} = 0$	0.525 ± 0.011	0.234 ± 0.013	0.644 ± 0.016	0.710 ± 0.014	0.274 ± 0.316	0.274 ± 0.316	0.274 ± 0.316
Bkg. subtraction	0.484 ± 0.046	0.146 ± 0.031	0.248 ± 0.046	0.406 ± 0.071	0.545 ± 0.118	0.676 ± 0.118	1.317 ± 0.337
	0.489 ± 0.046	0.151 ± 0.031	0.257 ± 0.046	0.419 ± 0.071	0.568 ± 0.117	0.705 ± 0.115	1.363 ± 0.342
Jet p_T Reweight	0.328 ± 0.068	0.124 ± 0.048	0.297 ± 0.100	0.234 ± 0.061	0.680 ± 0.092	0.452 ± 0.138	2.385 ± 1.729

(c) Fake factor for forward electrons ($1.37 < |\eta|$).

Table 5.14: Values of the fake factor in each p_T bin and for each individual systematic source.

	estimated yield	f_e stat. up	f_e stat. dn	f_e syst. up	f_e syst. dn	f_μ stat. up	f_μ stat. dn	f_μ syst. up	f_μ syst. dn
$e^\pm e^\pm$	11.42 ± 3.13	1.69	−1.69	1.67	−5.56	—	—	—	—
$\mu^\pm \mu^\pm$	4.82 ± 0.77	—	—	—	—	0.65	−0.65	3.64	−0.61
$\mu^\pm e^\pm$	37.08 ± 5.16	4.90	−4.90	5.59	−14.34	1.39	−1.39	16.10	−1.98

Table 5.15: Estimated yields for the fake lepton background. The estimated yield is shown in the first column together with the statistical uncertainty followed by the systematic uncertainties from variations of the the fake factors within their statistical (stat.) and systematic (syst.) uncertainties. The labels f_e and f_μ indicate the fake factors for electrons and muons, respectively.

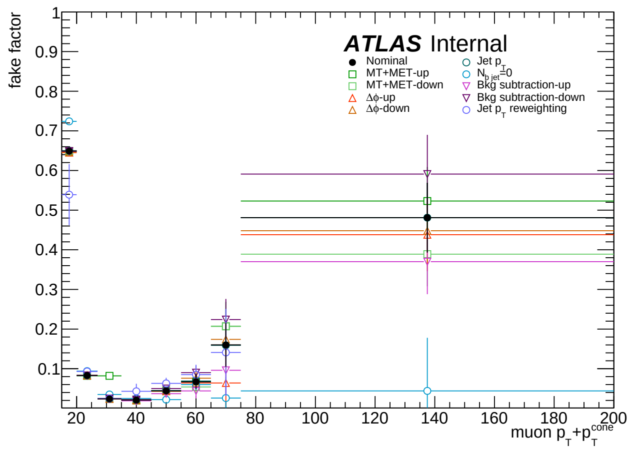

Figure 5.20: Systematic variations in the fake factor as a function of muon $p_{\mathrm{T}}+p_{\mathrm{T}}^{\mathrm{cone}}$. The individual fake factors obtained for each systematic variation are displayed with their statistical uncertainties.

5.3.4.6 Validation of the fake factor

The accuracy of the fake factor method is tested in several validation regions, the most sensitive of which is the same-sign top fakes VR (SS top VR), defined in Table 5.16. This region inverts the signal region's b-jet veto to accept events with exactly one b-jet. Due to this requirement, the dominant source of events comes from the $t\bar{t}$ process where a b-jet fakes an isolated lepton. The distribution of the subleading lepton p_{T} in this VR is shown in Figure 5.22 for all lepton flavor combinations. There is good agreement between the data and the prediction, even when only taking into account the statistical uncertainty and not the large systematic uncertainties assigned to the fake estimation.

Same-sign inclusive VR
Exactly 2 same-sign signal leptons
$p_{\mathrm{T}} > 27$ GeV for both leptons
$m_{ll} > 20$ GeV
$\lvert m_{ee} - m_Z \rvert > 15$ GeV ($e^{\pm}e^{\pm}$-channel only)
$N_{b\text{-jet}} = 1$
$N_{\mathrm{jet}} \geq 2$
Leading jet $p_{\mathrm{T}} > 65$ GeV
Subleading jet $p_{\mathrm{T}} > 35$ GeV

Table 5.16: Selection criteria for the same-sign top fakes validation region.

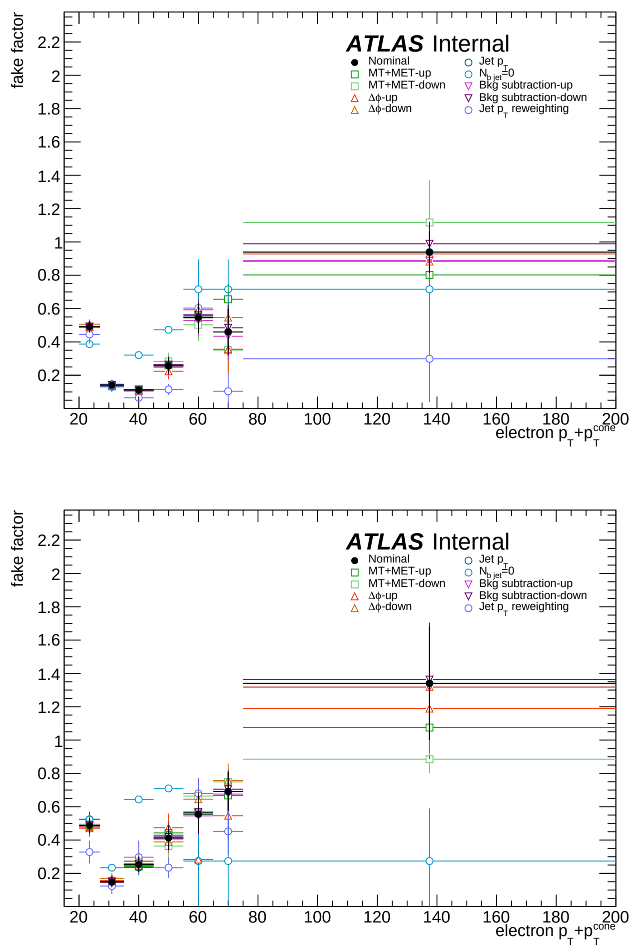

Figure 5.21: Systematic variations in the fake factor as a function of electron $p_{\mathrm{T}} + p_{\mathrm{T}}^{\mathrm{cone}}$ in the central ($|\eta| < 1.37$, top) and forward ($|\eta| > 1.37$, bottom) regions of the detector. The individual fake factors obtained for each systematic variation are displayed with their statistical uncertainties.

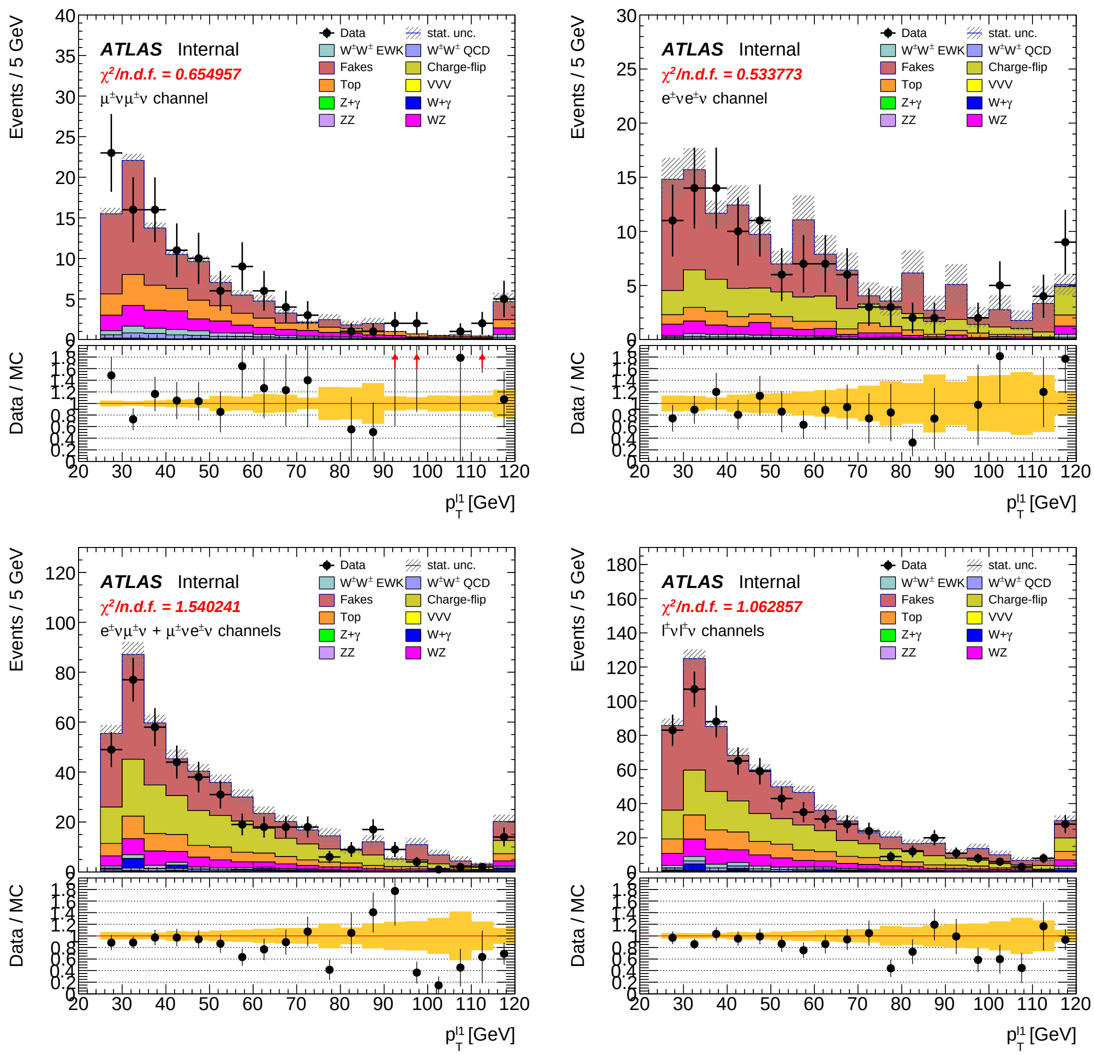

Figure 5.22: Distributions of the subleading lepton p_T in the same-sign top fakes VR for $\mu^\pm\mu^\pm$ events (top right), $e^\pm e^\pm$ events (top left), $\mu^\pm e^\pm$ events (bottom left), and all events combined (bottom right). All errors are statistical only.

5.3.5 Reduction of WZ background using custom overlap removal

The dominant source of prompt background in this analysis comes from WZ events where both bosons decay leptonically. Traditionally, the background is dealt with by imposing a veto on any event with a third lepton passing some loose identification criteria (the so-called *trilepton veto*). In the case of this analysis, if one or more leptons (in addition to the two signal leptons) passed the preselection criteria, the event would be rejected. However, WZ events can still enter the signal region if one of the leptons fails the veto selection or falls outside of the detector's acceptance.

In order to understand the sources of WZ events that are not removed by the trilepton veto, a study was performed on truth-level leptons[9] on $W^{\pm}W^{\pm}jj$ and WZ MC samples. Events with three truth leptons were selected, and each was matched to its reconstruction-level partner by finding the closest $\Delta R(\text{truth}, \text{reco})$ and $\Delta p_{\text{T,truth,reco}}$ match. For events surviving the trilepton veto, the two signal leptons were removed, and the remaining leptons represent real leptons that failed to be selected for the veto. Between 40-50% of these leptons fell outside of the eta acceptance of the analysis (see Figure 5.23) and were unrecoverable. The second largest source of leptons failing the preselection was the OR, defined in Section 5.2.1.4. The standard OF procedure appeared to be too aggressive in removing leptons in favor of jets, causing many three lepton events to "lose" their third lepton and pass the trilepton veto. Therefore a *Custom OR* was investigated which would replace the standard OR in the preselection and allow for better WZ rejection by removing fewer third leptons.

TODO: Mention how the extra leptons in the $W^{\pm}W^{\pm}jj$ are background leptons since there are only 2 from the main decay

In order to construct a "custom" OR, a new quantity is defined between a lepton (l) and a nearby jet (j)

$$p_{\text{T,ratio}}(l, j) = \frac{p_{\text{T}l}}{p_{\text{T}j}} \tag{5.13}$$

which, along with $\Delta R(l, j)$, will allow for more third leptons to pass the preselection. The idea behind including $p_{\text{T,ratio}}$ is to be able to preferentially remove background leptons originating from jets (i.e. those that carry a low percentage of the total jet momentum) instead of removing *any* lepton near to jet. The distributions of $p_{\text{T,ratio}}$ and the associated efficiency curves for muons and electrons can be found in Figures 5.24 and 5.26, respectively, and the distributions for $\Delta R(\mu, j)$ for

[9] Truth particles are the particles produced directly by the MC generator before being passed through the full detector simulation, at which point they are considered *reconstruction-level* (or *reco-level*) particles.

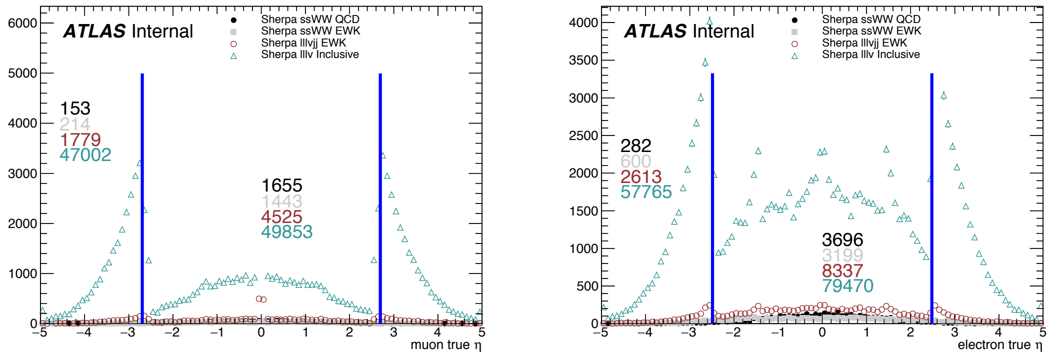

Figure 5.23: Pseudorapidity (η) distributions of truth muons (top) and electrons (bottom) for Sherpa $W^{\pm}W^{\pm}jj$ and WZ MC samples. The blue vertical lines represent the allowed η range for each lepton flavor. The numbers correspond to the number of raw MC events that fall within and outside of the allowed η range for each MC sample.

muons can be found in Figure 5.25. Since all electrons have an associated jet in the calorimeters, the $\Delta R(e, j)$ variable is not a good quantity to use for this custom OR.

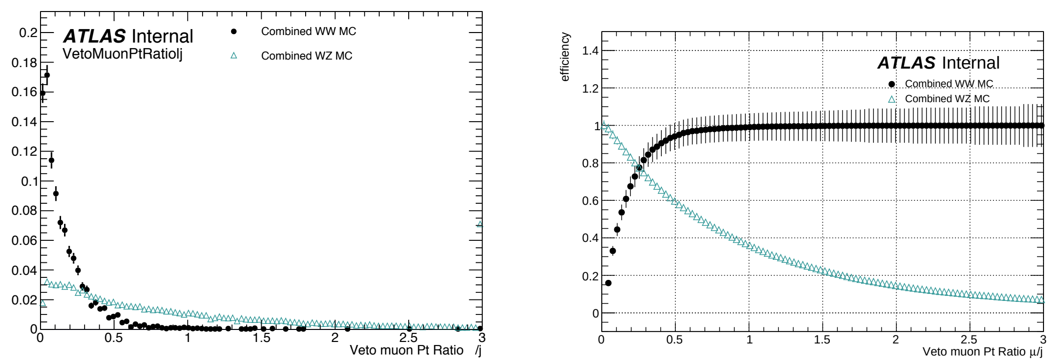

Figure 5.24: Distributions of $p_{\mathrm{T,ratio}}(\mu, j)$ for EWK and QCD $W^{\pm}W^{\pm}jj$ signal (black) and WZ background (teal) for truth-matched third muons in events that pass the trilepton veto. Both distributions are normalized to unit area. The associated efficiency curves are on the right where efficiency is defined as the percentage of total events that would pass a cut on $p_{\mathrm{T,ratio}}(\mu, j)$ at a given value on the x-axis.

A workingpoint for the Custom OR was chosen by requiring 90% signal retention for muons and 90% background rejection for electrons. The cut on electrons was allowed to be much tighter because the number of signal events with a third electron is considerably smaller than for muons. It should be re-emphasized the signal events that are present in Figures 5.24-5.26 do not represent the full set of signal events, but only those with a real third lepton (which must come from some

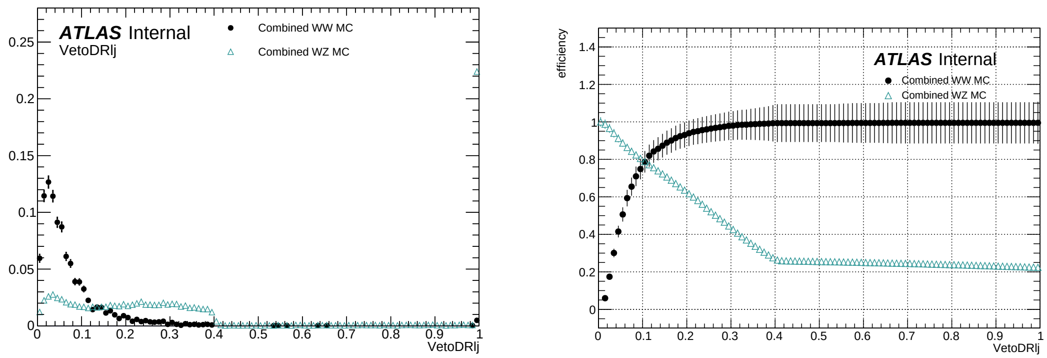

Figure 5.25: Distributions of $\Delta R(\mu, j)$ for EWK and QCD $W^{\pm}W^{\pm}jj$ signal (black) and WZ background (teal) for truth-matched third muons in events that pass the trilepton veto. Both distributions are normalized to unit area. The associated efficiency curves are on the right where efficiency is defined as the percentage of total events that would pass a cut on $\Delta R(\mu, j)$ at a given value on the x-axis.

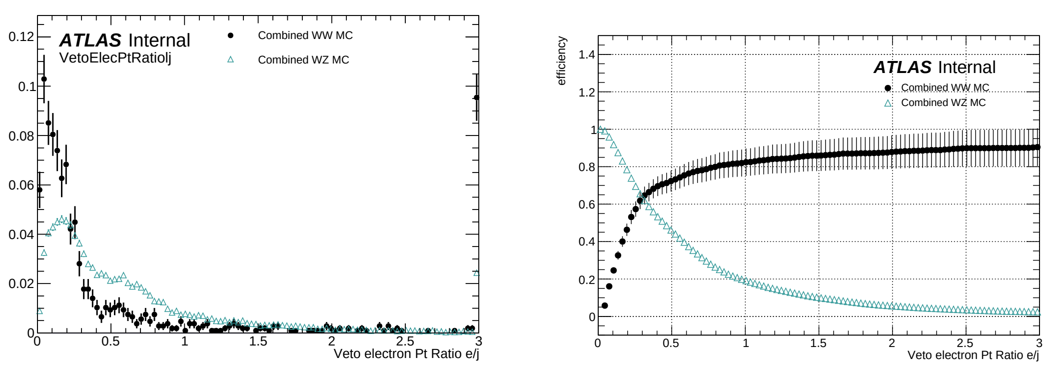

Figure 5.26: Distributions of $p_{\mathrm{T,ratio}}(e, j)$ for EWK and QCD $W^{\pm}W^{\pm}jj$ signal (black) and WZ background (teal) for truth-matched third electrons in events that pass the trilepton veto. Both distributions are normalized to unit area. The associated efficiency curves are on the right where efficiency is defined as the percentage of total events that would pass a cut on $p_{\mathrm{T,ratio}}(e, j)$ at a given value on the x-axis.

source other than the signal $W^{\pm}W^{\pm}jj$ process). For muons, an or of $p_{\mathrm{T,ratio}}(\mu, j)$ and $\Delta R(\mu, j)$ is used to maximize the third lepton acceptance due to correlations between the quantities, as shown in Figure 5.27; for electrons, only a cut on $p_{\mathrm{T,ratio}}(e, j)$ is used. The Custom OR workingpoint is outlined in Table 5.17.

Custom OR Definition	
Muons	$p_{\mathrm{T,ratio}}(\mu, j) > 0.40$ or $\Delta R(\mu, j) > 0.15$
Electrons	$p_{\mathrm{T,ratio}}(e, j) > 0.18$

Table 5.17: Custom OR definition. Leptons must pass this selection in order to be counted for the trilepton veto.

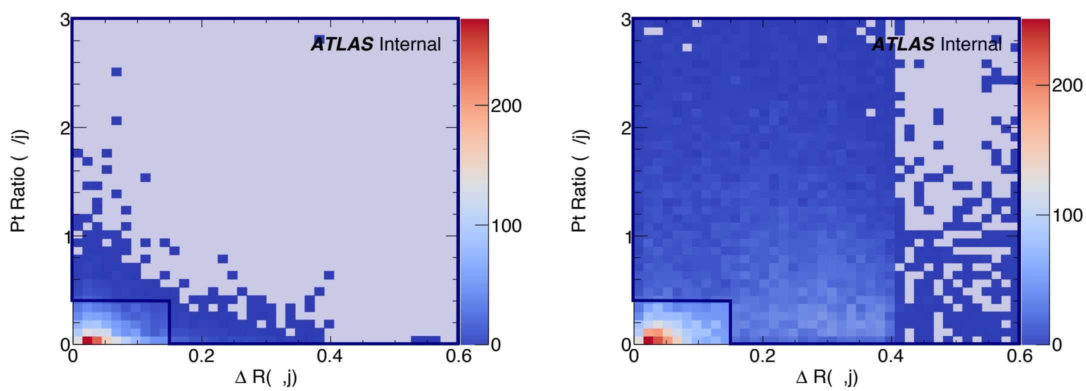

Figure 5.27: Two-dimensional plots of $p_{\mathrm{T,ratio}}(\mu, j)$ vs $\Delta R(\mu, j)$ for truth-matched third muons in events that pass the trilepton veto for EWK and QCD $W^{\pm}W^{\pm}jj$ signal (left) and WZ background (right). The blue overlay indicates the area in which the third leptons will pass the custom OR and result in the event failing the trilepton veto.

Tests of the performance of the Custom OR yield promising results, with approximately 20% reduction in WZ background compared to less than 2% signal loss in the signal region. Unfortunately, due to differences between the primary analysis framework and the one used for testing, in practice the gains in WZ rejection are not nearly as substantial, and ultimately the Custom OR is not included in the final analysis. However, it is still a potentially useful tool for improving background rejection via lepton number vetoes in analyses with overly aggressive OR procedures.

5.4 Cross section measurement

Hello world!

5.5 Results

Results

Chapter 6

Prospects for same-sign WW at the High Luminosity LHC

On December 3, 2018, Run 2 of the LHC officialy ended, and the collider was shut down to begin the first of two scheduled extended maintenance periods [45]. During these two long shutdowns, the Phase-I and Phase-II upgrades of the LHC and ATLAS will occur in order to prepare for the High-Luminosity LHC (HL-LHC) which is scheduled to begin operation in 2026 [46].

The HL-LHC is planned to run at a center-of-mass energy of $\sqrt{s} = 14$ TeV with an instantaneous luminosity of $\mathcal{L} = 5 \times 10^{34}$ cm^{-2}s^{-1} with up to 200 collisions per beam-crossing. Over the course of operation, the HL-LHC is expected to collect a total integrated luminosity of $\mathcal{L} = 3000$ fb^{-1} by 2035 [47]. TODO: Compare to current LHC numbers?

These run conditions will be much harsher than what ATLAS has experienced so far, and there are several upgrades planned for the detector to operate in the high luminosity environment. Most notably, the entire ID will be replaced with an all-silicon tracker which will extend the coverage from $|\eta| \leq 2.7$ up to $|\eta| \leq 4.0$. This will allow for reconstruction of charged particle tracks which can in turn be matched to clusters in the calorimeters for electron identification or forward jet tagging [48].

The upgraded detector, the higher beam energy, and the increased volume of data to be collected provides the opportunity to measure rarer processes with a much higher precision than what was possible in Run 1. Same-sign $W^{\pm}W^{\pm}jj$ production, is one such process. With greater statistics, the accuracy of the cross section measurement can be improved over the 13 TeV analysis detailed in Chapter 5, and it also will allow for more detailed physics studies, such as measuring the polarization of the W bosons. A measurement of the longitudinal polarization of the scattered W bosons has not yet been possible, but it remains of great interest due to its sensitivity to electroweak symmetry breaking [49]. The analysis detailed in this chapter is based off of the 2018 ATLAS HL-LHC $W^{\pm}W^{\pm}jj$ prospects study [50] which is itself an extension of the 2017 ATLAS study [51]. TODO: mention CMS's study + yellow report?

6.0.1 Analysis Overview

The experimental signature of interest is identical to the 13 TeV analysis: two prompt leptons (either electrons or muons) with the same charge, missing transverse energy, and two high energy, forward jets. These jets are again required to have a large angular separation and a high combined invariant mass to preferentially select EWK- over QCD-produced $W^{\pm}W^{\pm}jj$ events.

Background processes are again similar to the 13 TeV analysis and are summarized again here. The dominant source of prompt background from WZ+jets events where both bosons decay leptonically. If the lepton from the Z-decay with opposite charge from the W falls outside of the detector acceptance or is not identified, the remainder could appear to be a $W^{\pm}W^{\pm}jj$ signal event. To a lesser extent, ZZ+jets events can enter the signal region in much the same way provided two leptons are "lost". Other prompt sources include $t\bar{t}+V$ and and multiple parton interactions, however these processes do not contribute much. These prompt backgrounds are expected to contribute less than in Run 2 with the addition of forward tracking in the upgraded ATLAS detector. Jets mis-reconstructed as leptons or leptons from hacronic decays (such as $t\bar{t}$ and W+jets production) comprise the non-prompt lepton background. Lastly, events with two prompt, opposite-charge electrons can appear as a same-sign event provided one of the electrons is mis-reconstructed as the wrong charge.

In this analysis, the EWK production of $W^{\pm}W^{\pm}jj$ is studied in the context of the planned HL-LHC run conditions and upgraded ATLAS detector. An optimized event selection (referred to as the *optimized selection*) is also explored in an effort to gain increased signal significance over the *default selection.* The cross section of the inclusive EWK production is measured for both the default and optimized selections, and the extraction of the longitudinal scattering significance is measured with the optimized selection.

6.1 Theoretical motivation

The theoretical motivation for studying the ssWW process–and VBS in general–is detailed in Section 5.0.1. Since it is specifically the scattering of *longitudinally polarized* vector bosons that violates unitarity without a SM Higgs boson, a direct measurement of this cross section will be very useful for understanding how the Higgs unitarizes the process [49].

6.1.1 Experimental sensitivity to longitudinal polarization

TODO: mention that since there are so many polarization possibilities, a large integrated luminosity is needed to measure just one of them individually There are three possible polarization states for a massive vector boson: two transverse (+ or −) and one longitudinal (0). Therefore, in a system with two W bosons, the overall polarization can be purely longitudinal (00), purely transverse (++, −−, and +−), or mixed (+0 and −0). The three combinations will be referred to as LL, TT, and LT respectively.

In order extract the longitudinal scattering component, it is necessary to find variables that distinguish the LL from the TT and LT. Several were studied, and those with the best discriminating power between the polarizations are the leading and subleading lepton p_{T} as well as the azimuthal separation ($|\Delta\phi_{jj}|$) of the two VBS jets. The LL events prefer lower p_{T} for both signal leptons (see Figure 6.1), which motivates keeping cuts on these quantities as low as possible in the event selection.In the case of $|\Delta\phi_{jj}|$, the LL events generally had a larger dijet separation (see Figure 6.2), and this variable is used in a binned likelihood fit to extract the longitudinal scattering significance.

6.2 Monte Carlo samples

As no real HL-LHC data will be available for many years, all signal and background processes are modeled using MC simulations generated at $\sqrt{s} = 14$ TeV, with the event yields scaled to the anticipated HL-LHC integrated luminosity of $\mathcal{L} = 3000$ fb^{-1}. The MC samples used in the analysis are generated at particle-level and have not been run through the typical full simulation of the ATLAS detector. Instead, smearing functions derived from a `GEANT4` simulation of the upgraded ATLAS detector are used to estimate detector effects such as momentum resolution. In addition, pileup events are fully simulated. The MC samples used in this analysis are summarized in Table 6.1.

The signal sample consists of both VBS and non-VBS electroweak (EWK) $W^{\pm}W^{\pm}jj$ production, and it is sumulated with the `Madgraph5_aMC@NLO` generator using the `NNPDF3.0` PDF set and interfaced with `PYTHIA v8` [52] for hadronization and parton showering. To study the longitudinal polarization more directly, two additional `Madgraph5_aMC@NLO` $W^{\pm}W^{\pm}jj$ samples are used: one containing only the longitudinal contribution (LL) and a second containing the transverse (TT) and mixed (LT) contributions.

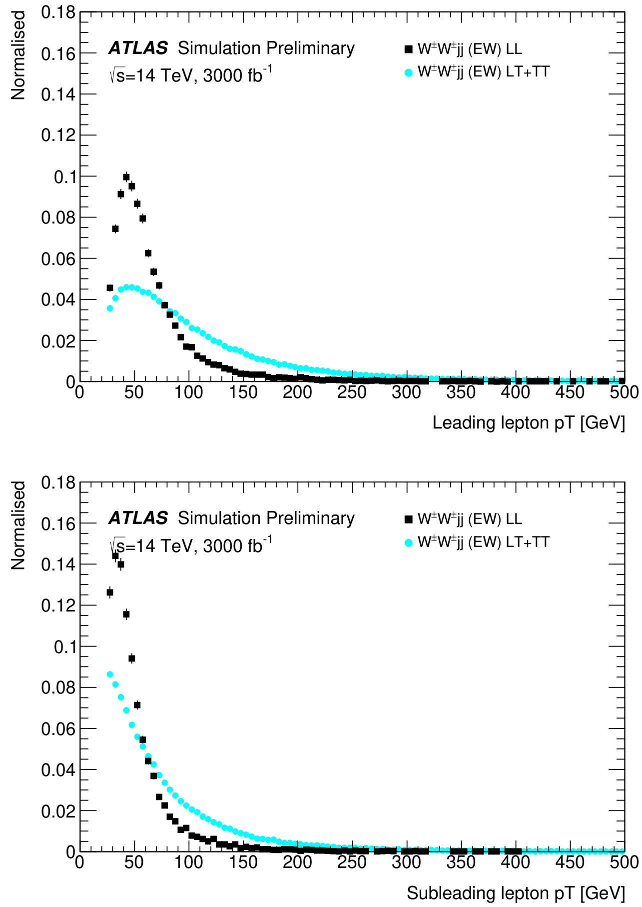

Figure 6.1: Comparison of the leading (top) and subleading (bottom) lepton p_{T} distributions for purely longitudinal (LL, black) and mixed polarization (LT+TT, cyan) $W^{\pm}W^{\pm}jj$ events.

There are many other processes that can produce the same final state as the $W^{\pm}W^{\pm}jj$ and must also be accounted for using MC simulations. WZ events are generated using `SHERPA v2.2.0`, which includes up to one parton at NLO in the strong coupling constant and up to three additional partons at LO. Both EWK and QCD production are included in these samples. ZZ and triboson VVV ($V = W, Z$) events are generated using `SHERPA v2.2.2` with up to two additional partons in the final state. For the triboson backgrounds, the bosons can decay leptonically or hadronically. W+jets backgrounds are generated for electron, muon, and tau final states at LO with `Madgraph5_aMC@NLO` and the `NNPDF3.0` set with showering from `PYTHIA v8`. Z+jets events are produced using `POWHEG-BOX v2` and the `CT10` PDF set interfaced with `PYTHIA v8`. Finally, $t\bar{t}$ and single-top events are generated using `POWHEG-BOX` with showering from `PYTHIA v6`.

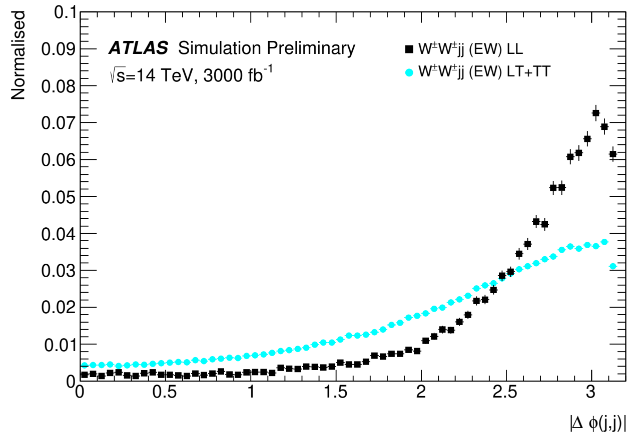

Figure 6.2: Comparison of the azimuthal dijet separation ($|\Delta\phi_{jj}|$) for purely longitudinal (LL, black) and mixed polarization (LT+TT, cyan) $W^{\pm}W^{\pm}jj$ events.

Process	Generator	Comments
$W^{\pm}W^{\pm}jj$ (EWK)	`Madgraph5_aMC@NLO`	Signal sample
$W^{\pm}W^{\pm}jj$ (QCD)	`Madgraph5_aMC@NLO`	
$W^{\pm}W^{\pm}jj$ (LL)	`Madgraph5_aMC@NLO`	Pure longitudinal polarization sample
$W^{\pm}W^{\pm}jj$ (TT+LT)	`Madgraph5_aMC@NLO`	Mixed and transverse polarization sample
Diboson	`SHERPA v2.2.0`	WZ events
	`SHERPA v2.2.2`	ZZ events
Triboson	`SHERPA v2.2.2`	
W+jets	`Madgraph5_aMC@NLO`	
Z+jets	`POWHEG-BOX v2`	
$t\bar{t}$	`POWHEG-BOX`	
Single top	`POWHEG-BOS`	

Table 6.1: Summary of MC samples used in the analysis.

6.3 Background estimations

In this analysis, all background contributions are estimated using MC simulations. Backgrounds such as electron charge misidentification and fake electrons from jets (which are traditionally estimated using data-driven techniques) are estimated using a set of parameterization functions applied to the MC. These functions calculate the probability that an electron is assigned the wrong charge or a jet is mis-reconstructed as an electron parameterized by the p_{T} and η of the electron or jet. The probabilites are derived from studies on expected electron performance with the upgraded ATLAS detector [53].

Processes involving two W and Z bosons are grouped together as *diboson* backgrounds, with the exception of $W^{\pm}W^{\pm}jj$ events produced via QCD interactions, which are kept separate. Similarly, all backgrounds with three vector bosons are combined and labeled as *triboson*. Any W+jets or top events that pass selection and do not contain a fake electron, as well as any Z+jets events without an electron identifed as having its charge misidentified are combined as *other non-prompt* backgrounds.

6.3.1 Truth-based isolation

To properly calculate particle isolation, it requires information from several detector subsystems including tracking and calorimeter responses. Since the MC samples used in this analysis have not been run through a full detector simulation, it is not possible to construct the canonical isolation variables used in analyses. At truth-level, this is generally not a serious concern as p_{T} signal leptons tend to be well isolated to begin with. However, isolation is one of the most powerful tools for rejecting leptons from non-prompt sources such as top events, which are produced in association with additional nearby particles from b and c quark decays. In this analysis, with the absence of any sort of isolation requirement, contributions from top backgrounds (including single top, $t\bar{t}$ and $t\bar{t}+V$) are more than an order of magnitude higher than expected.

As a result, it is necessary to find one or more quantities that are comparable to the isolation information that is available in fully-simulated samples. Analogues to track- and calorimeter-based isolation variables are constructed by summing the momentum and energy, respectively, of stable truth particles with $p_{\mathrm{T}} > 1$ GeV within a specified radius of each signal lepton. For the track-based isolation, only charged truth particles are used; both charged and neutral particles (excluding neutrinos) are included for the calorimeter-based isolation. Ultimately, a set of isolation cuts are chosen that are similar to those recommended by ATLAS for Run 2 analyses. The truth-based isolation requirements are listed in Table 6.2.

	Electron Isolation	Muon Isolation
Track-based isolation cone size	$\Delta R < 0.2$	$\Delta R < 0.3$
Track-based isolation requirement	$\sum p_{\mathrm{T}}/p_{\mathrm{T}}^{e} < 0.06$	$\sum p_{\mathrm{T}}/p_{\mathrm{T}}^{\mu} < 0.04$
Calorimeter-based isolation cone size	$\Delta R < 0.2$	$\Delta R < 0.2$
Calorimeter-based isolation requirement	$\sum E_{\mathrm{T}}/p_{\mathrm{T}}^{e} < 0.06$	$\sum E_{\mathrm{T}}/p_{\mathrm{T}}^{\mu} < 0.15$

Table 6.2: Truth-based isolation requirements for electrons and muons.

The truth-based isolation requirement reduces the top background by over 99%, and the percentage of the total background consisting of top events is reduced from 83% to 2%. Additional details on the truth-based isolation studies are presented in Appendix A.

6.4 Object and event selection

6.4.1 Object selection

Electrons and muons are preselected to have $p_{\mathrm{T}} > 7$ and 6 GeV, respectively, and $|\eta| \leq 4.0$. The likelihood of a given lepton to pass the trigger and identification requirements is estimated by calculating an efficiency dependent on the p_{T} and η of the lepton. The leptons are also required to pass the isolation criteria detailed in Table 6.2. Jets that have been tagged as a fake electron by the functions described in Section 6.3 are treated as electrons for the purpose of the object selection and are subject to the same criteria. In order to be considered a signal lepton, an additional requirement of $p_{\mathrm{T}} > 25$ GeV is applied on top of the preselection. The two highest p_{T} leptons passing this selection are chosen to be the leading and subleading signal leptons.

Jets are clustered using the anti-k_t algorithm [37] from final-state particles within a radius of $\Delta R = 0.4$ (excluding muons and neutrinos). Jets are required to have $p_{\mathrm{T}} > 30$ GeV and lie within $|\eta| < 4.5$, with an additional cut of $p_{\mathrm{T}} > 70$ GeV for jets above $|\eta| \geq 3.8$ in order to suppress jets from pileup interactions. Jets overlapping with a preselected electron within $\Delta R(e, j) < 0.05$ are removed in order to prevent double counting. The two highest p_{T} jets are defined as the leading and subleading *tag jets*.

6.4.2 Event selection

The default event selection is summarized in Table 6.3 and described here. Exactly two signal leptons are required with the same electric charge and separated from each other by $\Delta R(ll) > 0.3$. In order to suppress contributions from Drell-Yan backgrounds, the two signal leptons must have an invariant mass m_{ll} greater than 20 GeV. Additionally, if both signal leptons are electrons, their mass must be at least 10 GeV from the Z-boson mass in order to reduce background from Z-boson decays[10]. The event is required to have at least 40 GeV of missing transverse energy ($E_{\mathrm{T}}^{\mathrm{miss}}$) to account for the two neutrinos from the W decays. Events with additional preselected leptons are vetoed, which greatly reduces WZ and ZZ backgrounds.

Each event must have at least two jets, and both tag jets are required to not overlap with the signal leptons, and there is a veto on events with one or more b-jets. In order to preferentially select EWK production, the tag jets are also required to have a large separation between them and a large

[10]The electron charge misidentification rate in the upgraded ATLAS detector is estimated to be high enough that contributions from $Z \to ee$ backgrounds are non-negligible.

invariant mass. Finally, a cut on the lepton centrality[11], ζ, defined in Equation 6.1 enhances the EWK $W^{\pm}W^{\pm}jj$ signal.

$$\zeta = \min[\min(\eta_{\ell 1}, \eta_{\ell 2}) - \min(\eta_{j1}, \eta_{j2}), \max(\eta_{j1}, \eta_{j2}) - \max(\eta_{\ell 1}, \eta_{\ell 2})] \tag{6.1}$$

Selection requirement	Selection value
Lepton kinematics	$p_{\mathrm{T}} > 25$ GeV $\lvert\eta\rvert \leq 4.0$
Jet kinematics	$p_{\mathrm{T}} > 30$ GeV for $\lvert\eta\rvert \leq 4.5$ $p_{\mathrm{T}} > 70$ GeV for $\lvert\eta\rvert > 3.8$
Dilepton charge	Exactly two signal leptons with same charge
Dilepton separation	$\Delta R_{l,l} \geq 0.3$
Dilepton mass	$m_{ll} > 20$ GeV
Z boson veto	$\lvert m_{ee} - m_Z\rvert > 10$ GeV (ee-channel only)
$E_{\mathrm{T}}^{\mathrm{miss}}$	$E_{\mathrm{T}}^{\mathrm{miss}} > 40$ GeV
Jet selection	At least two jets with $\Delta R_{l,j} > 0.3$
b jet veto	$N_{\text{b-jet}} = 0$
Dijet separation	$\Delta\eta_{jj} > 2.5$
Trilepton veto	No additional preselected leptons
Dijet mass	$m_{jj} > 500$ GeV
Lepton-jet centrality	$\zeta > 0$

Table 6.3: Summary of the signal event selection.

6.5 Selection optimization

An upgraded detector along with an increase in center of mass energy and integrated luminosity provides an opportunity to study whether the event selection can be optimized to improve the signal to background ratio.

6.5.1 Random grid search algorithm

The chosen method for optimizing the event selection is a cut-based algorithm known as the Random Grid Search (RGS) [54]. Consider a simple case of two variables x and y chosen to differentiate signal from background. In order to be considered a signal event, a given event would be required to pass a set of selection criteria, called a *cut point*: $c = \{x > x_c, y > y_c\}$. A simple method to choose the optimal cut point (i.e. the "best" values of the cuts x_c and y_c) would be to construct an $n \times m$

[11] ζ is a measurement of whether the two signal leptons lie between the two tagging jets in η, as is preferred by the VBS topology.

rectangular grid in x and y consisting of points $(x_0, y_0), (x_1, y_1), ..., (x_n, y_m)$, as in Figure 6.3. One can then choose a cut point $c_k = \{x > x_i, y > y_j\}$ that maximizes the signal significance as measured by a chosen metric. This would be considered a *rectangular grid search*.

While effective in principle, a rectangular grid search comes with two major drawbacks:

1. The algorithm scales exponentially as the number of variables to be optimized increases, as this is effectively increasing the dimensionality of the grid. In the simple case of a square grid with N bins per variable v, the number of cut points to be evaluated grows as N^v.
2. Signal and background samples are rarely evenly distributed over the entire grid, resulting in many cut points being sub-optimal and evaluating them would be a waste of computing resources.

To combat these limitations, the RGS algorithm constructs a grid of cut points directly from the signal sample itself. In the two-dimensional example, this means that the variables x_i and y_j making up the cut point $c_k = \{x > x_i, y > y_j\}$ take their values directly from a given signal event. This has the benefit of creating a *random grid* of cut points that is biased towards regions of high signal concentration by construction. This reduces the need for exponentially increasing numbers of cut points while ensuring that computing resources are not wasted in regions with few to no signal events. An example of the the two-dimensional random grid is shown in Figure 6.4.

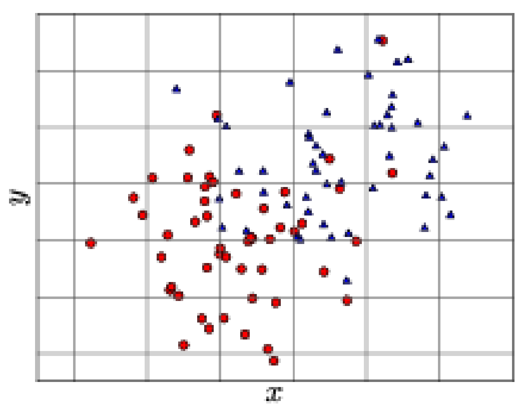

Figure 6.3: A visual representation of a rectangular grid search algorithm. The signal events are the blue triangles, and the red circles are the background events. TODO: replace with own figure

Once the random grid of cut points is constructed, the optimal cut point can be chosen using any number of metrics, such as signal to background ratio. For the purpose of the $W^{\pm}W^{\pm}jj$ upgrade

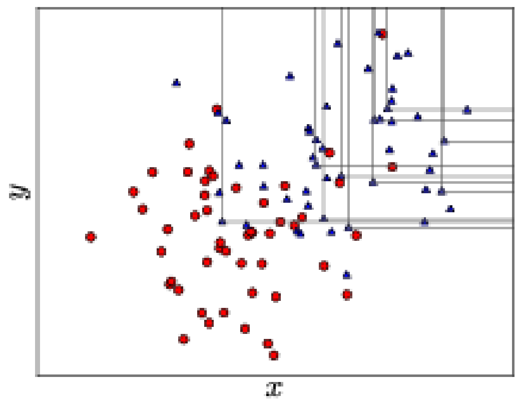

Figure 6.4: A visual representation of a random grid search algorithm. The signal events are the blue triangles, and the red circles are the background events. TODO: replace with own figure

study, the optimal cut point is chosen to be the one that mazimizes the signal significance Z as defined in Equation 6.2 [55].

$$Z = \sqrt{2\left[(s+b)\ln\left(\frac{s+b}{b_0}\right) + b_0 - s - b\right] + \frac{(b-b_0)^2}{\sigma_b^2}} \tag{6.2}$$

where s and b are the number of signal and background events, respectively, σ_b is the total uncertainty on the background, and b_0 is defined as:

$$b_0 = \frac{1}{2}\Big(b - \sigma_b^2 + \sqrt{(b-\sigma_b^2)^2 + 4(s+b)\sigma_b^2}\Big) \tag{6.3}$$

In the case where the backround is known precisely (i.e. $\sigma_b = 0$), Equation 6.2 simplifies to

$$Z = \sqrt{2\Big(b\big[(1+s/b)\ln(1+s/b) - s/b\big]\Big)} \tag{6.4}$$

which further reduces to the familiar $Z = s/\sqrt{b}$ for the case when $s << b$.

6.5.2 Inputs to the optimization

In order to train the RGS, signal and background samples are prepared from events passing the event selection outlined in Table 6.3 up through the b-jet veto. The signal sample is chosen to be the longitudinally polarized $W^\pm W^\pm jj$ EWK events, and the transverse and mixed polarizations are treated as background along with $W^\pm W^\pm jj$ events from QCD interactions and the traditional backgrounds listed in Section 6.3. Splitting the inclusive $W^\pm W^\pm jj$ EWK events by polarization allows the optimization to favor the longitunally polarized events as much as possible, even though they both contribute to the EWK signal.

The following variables are chosen for optimization:

- Leading lepton p_{T}
- Dilepton invariant mass (m_{ll})
- Leading and subleading jet p_{T}
- Dijet invariant mass (m_{jj})
- Lepton-jet centrality (ζ)

Subleading lepton p_{T} is omitted as it is desirable to keep the cut value as low as possible due to its sensitivity to the longitudinal polarization (as discussed in Section 6.1.1). Additionally, the dijet separation $\Delta\eta_{jj}$ was included in the optimization originally, however it was dropped from the list due to the cut value being motivated by differences between EWK and QCD produced $W^{\pm}W^{\pm}jj$ events.

Two additional constraints were imposed when selecting the optimal cut point:

1. At least 1000 signal events must survive in order to prevent the optimization from being too aggressive and unnecssarily reducing signal statistics.
2. The dijet invariant mass may only vary within a 50 GeV range of the default value (from $450 - 550$ GeV) due to the cut being physically motivated by the VBS event topology (see Section 5.0.2).

Lastly, the signal significance is calculated without taking into account the uncertainty of the background using Equation 6.4. This is due to the fact that the statistical uncertainties of the fake electron and charge misidentification backgrounds are quite large, owing to poor MC statiscs in a few of the samples. If Equation 6.2 were used instead, the optimization will cut unreasonably hard against these backgrounds. Since Monte Carlo statistics is not expected to be a limiting factor when this analysis is performed at the HL-LHC, it is more realistic to simply ignore these large statistical uncertainties for the purpose of the optimization.

6.5.3 Results of the optimization

Ultimately, the random grid is constructed from over 38,000 LL-polarized $W^{\pm}W^{\pm}jj$ events in the six variables listed above. After applying the constraints, the optimal cut point reduces the total background from 9900 to 2310 while reducing the signal from 3489 to 2958. This corresponds to an increase in signal significance from $Z = 33.26$ to $Z = 52.63$ as calculated by Equation 6.4. The updates to the event selection are listed in Table 6.4.

The large reduction in the background is primarily a result of the increase in the leading and subleading jet p_{T} from 30 GeV to 90 GeV and 45 GeV, respectively. As can be seen in Figure 6.7, this increase removes a significant portion of the backgrounds from jets faking electrons and charge mis-ID. Additionally, the loosening of the lepton-jet centrality cut ζ allows more signal events to survive the event selection (see Figure 6.9). Other changes to the event selection are minor and do not individually have a large impact on the signal or background yields.

The full event yields after optimization as well as the cross section measurement are detailed alongside those using the default selection in Section 6.6.

TODO: It's a bit awkward to reference the results of the default/optimized before they're properly presented. Maybe move the sections around? not sure...

Selection requirement	Selection value
Lepton kinematics	$p_{\mathrm{T}} > 28$ GeV (leading lepton only)
Jet kinematics	$p_{\mathrm{T}} > 90$ GeV (leading jet)
	$p_{\mathrm{T}} > 45$ GeV (subleading jet)
Dilepton mass	$m_{ll} > 28$ GeV
Dijet mass	$m_{jj} > 520$ GeV
Lepton-jet centrality	$\zeta > -0.5$

Table 6.4: Updates to the $W^{\pm}W^{\pm}jj$ event selection criteria after optimization. Cuts not listed remain unchanged from the default selection in Table 6.3.

6.6 Results

6.6.1 Event yields

After applying the full event selection, the analysis is broken down into four channels based off of the flavor of the signal leptons: $\mu\mu$, ee, μe, and $e\mu$. The full signal and background event yields are shown in Table 6.5 for each channel separately and combined using the default event selection. 3489 EWK $W^{\pm}W^{\pm}jj$ events are expected compared to 9900 background events. The dominant sources of background are jets faking electrons followed by charge misidentification and diboson processes. Triboson events, QCD $W^{\pm}W^{\pm}jj$, and other non-prompt sources make up approximately 5% of the total background combined.

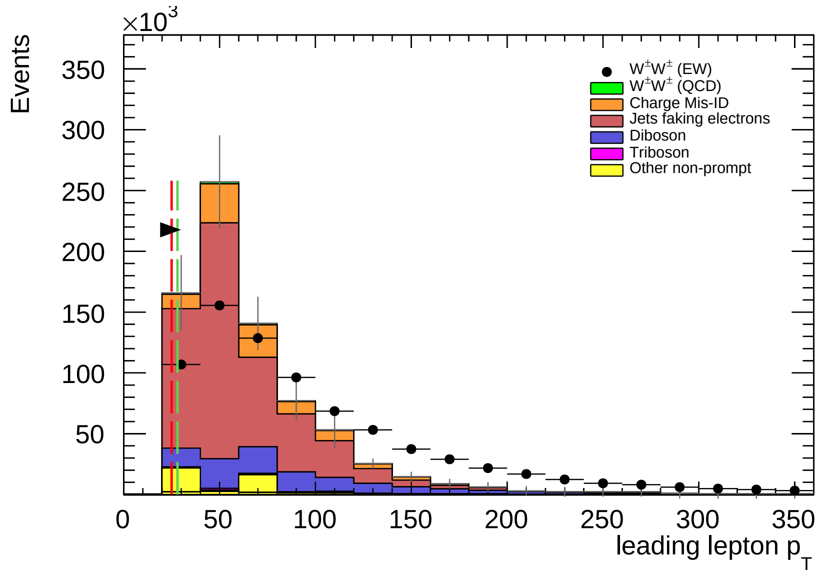

Figure 6.5: Leading lepton p_{T} distribution. The default and optimized cuts are represented by the red and green dashed lines, respectively. The $W^{\pm}W^{\pm}jj$ EWK signal (black points) is normalized to the same area as the sum of the backgrounds (colored histogram). TODO: Move to appendix or omit

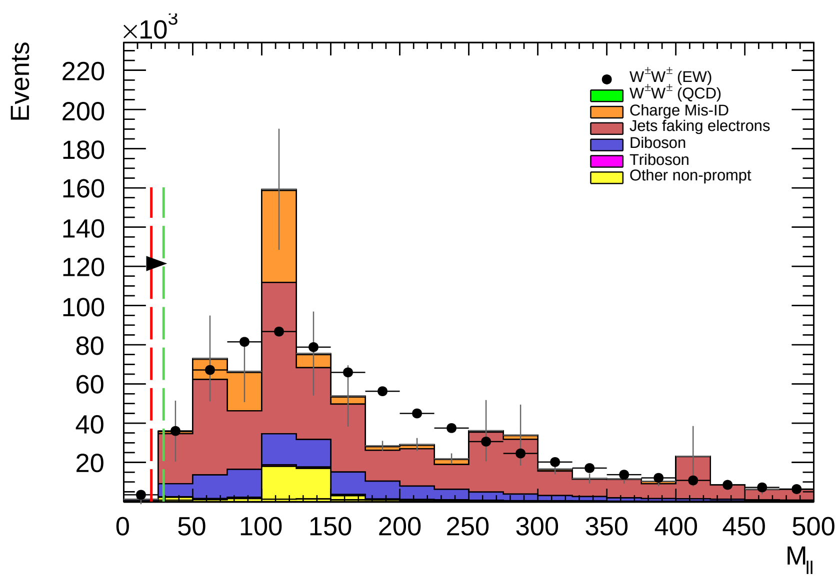

Figure 6.6: Dilepton invariant mass distribution. The default and optimized cuts are represented by the red and green dashed lines, respectively. The $W^{\pm}W^{\pm}jj$ EWK signal (black points) is normalized to the same area as the sum of the backgrounds (colored histogram). TODO: Move to appendix or omit

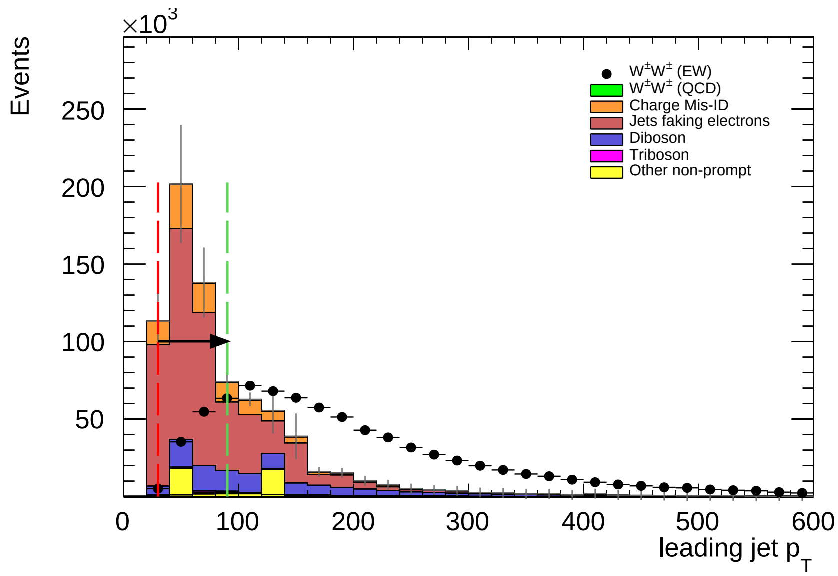

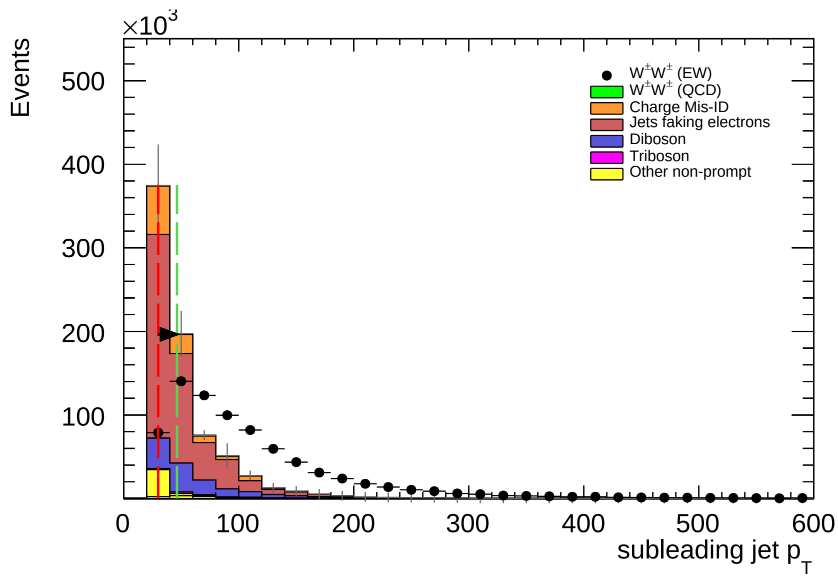

Figure 6.7: Leading (top) and subleading (bottom) jet p_{T} distributions. The default and optimized cuts are represented by the red and green dashed lines, respectively. The $W^{\pm}W^{\pm}jj$ EWK signal (black points) is normalized to the same area as the sum of the backgrounds (colored histogram).

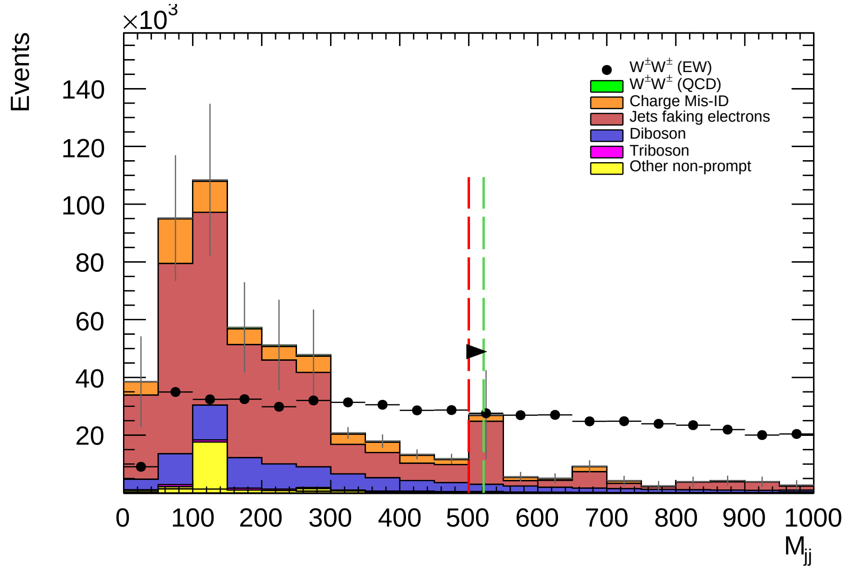

Figure 6.8: Dijet invariant mass distribution. The default and optimized cuts are represented by the red and green dashed lines, respectively. The $W^{\pm}W^{\pm}jj$ EWK signal (black points) is normalized to the same area as the sum of the backgrounds (colored histogram). TODO: Move to appendix or omit

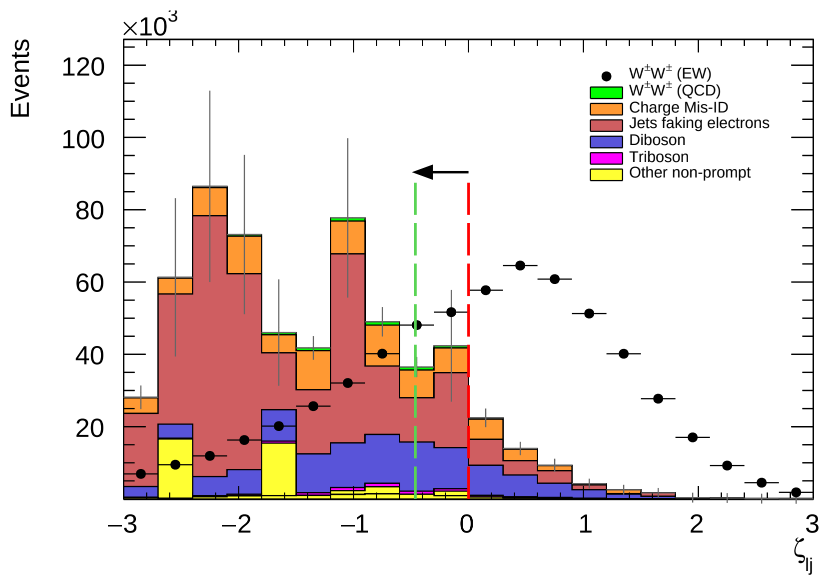

Figure 6.9: Lepton-jet centrality distribution. The default and optimized cuts are represented by the red and green dashed lines, respectively. The $W^{\pm}W^{\pm}jj$ EWK signal (black points) is normalized to the same area as the sum of the backgrounds (colored histogram).

	All channels	$\mu\mu$	ee	μe	$e\mu$
$W^{\pm}W^{\pm}jj$ (QCD)	206.4	91.1	22.8	38.4	54.1
Charge Misidentification	2300	0.0	2100	90	160
Jets faking electrons	5000	0.0	3400	1200	340
$WZ + ZZ$	2040	500	438	423	680
Tribosons	115	47	15.4	21.6	31.2
Other non-prompt	210	110	20	60	27
Total Background	9900	750	6000	1900	1290
Signal $W^{\pm}W^{\pm}jj$ (EWK)	3489	1435	432	679	944

Table 6.5: Signal and background event yields using the default event selection for an integrated luminosity of $\mathcal{L} = 3000$ fb^{-1}. Events containing a fake or charge-flipped electron are removed from their respective sources and combined into a single entry each.

The event yields for the optimized selection detailed in Section 6.5.3 are listed in Table 6.6. After optimization, 2958 signal events and just 2310 background events are expected. Diboson events are now the primary source of background, as the optimization greatly reduces the fake and charge misidentification backgrounds. As discussed earlier, the increase in the leading and subleading jet p_{T} cuts as well as the loosening of the centrality cut are most responsible for the changes in the signal and background yields; distributions of these quantities using the default and the optimized event selections can be found in Figures 6.10, 6.11, and 6.12, respectively.

	All channels	$\mu\mu$	ee	μe	$e\mu$
$W^{\pm}W^{\pm}jj$ (QCD)	168.7	74.6	19.7	32.2	42.2
Charge Misidentification	200	0.0	11	30	160
Jets faking electrons	460	0.0	130	260	70
$WZ + ZZ$	1286	322	289	271	404
Tribosons	76	30.1	9.6	15.1	21.6
Other non-prompt	120	29	16.6	50	19
Total Background	2310	455	480	660	710
Signal $W^{\pm}W^{\pm}jj$ (EWK)	2958	1228	380	589	761

Table 6.6: Signal and background event yields using the optimized event selection for an integrated luminosity of $\mathcal{L} = 3000$ fb^{-1}. Events containing a fake or charge-flipped electron are removed from their respective sources and combined into a single entry each.

It is important to note, however, that the MC sample used to estimate Z+jets events suffers from poor statistics which results in large per-event weights once scaled to $\mathcal{L} = 3000$ fb^{-1}. This sample contributes heavily to the fake and charge misidentification backgrounds, and a handful of these events being cut out by the optimization contributes has a large effect on the dramatic reduction of these backgrounds. As a result, these particular optimized results are likely overly optimistic. However, given proper MC statistics, it is still expected that the optimization will outperform the

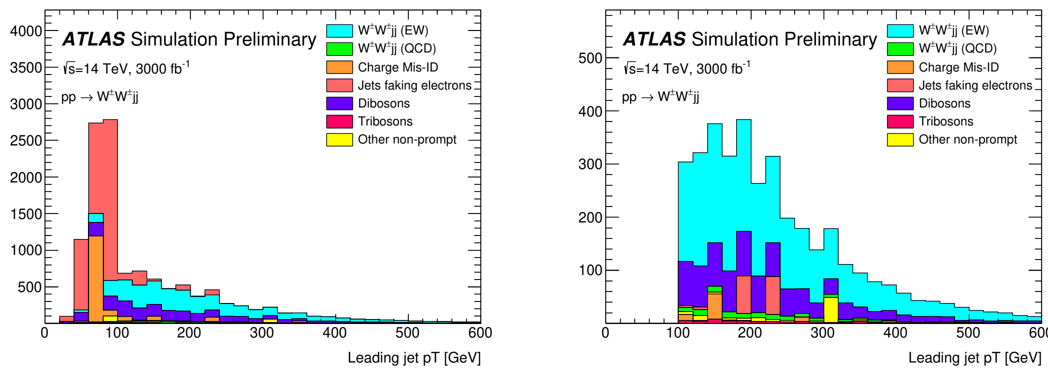

Figure 6.10: p_{T} distributions for the leading jet using the default (left) and optimized (right) event selections for all channels combined.

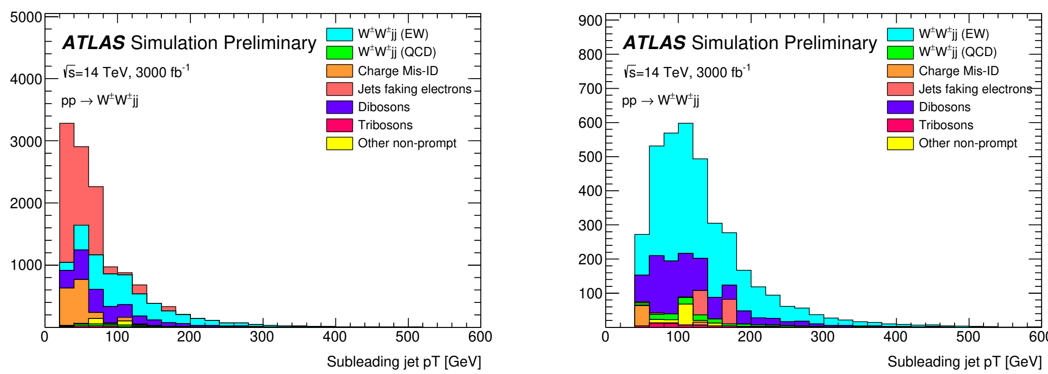

Figure 6.11: p_{T} distributions for the subleading jet using the default (left) and optimized (right) event selections for all channels combined.

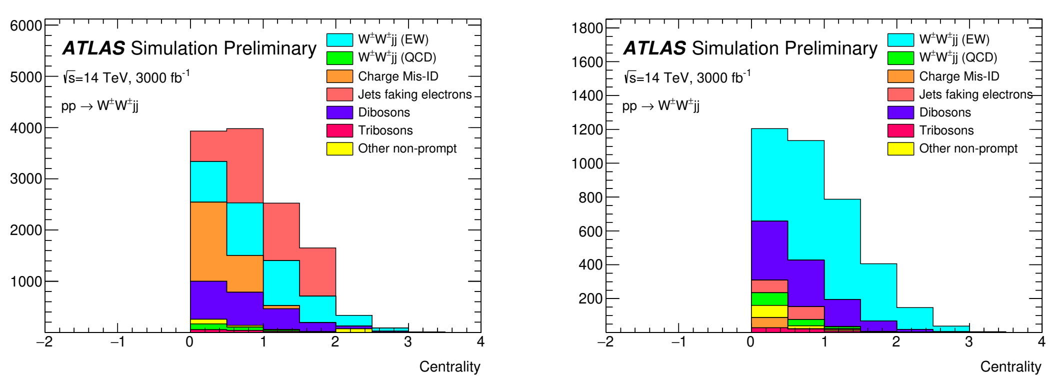

Figure 6.12: p_{T} distributions for lepton-jet centrality ζ using the default (left) and optimized (right) event selections for all channels combined.

default selection.

6.6.2 Uncertainties

TODO: Ask for details on how some of these uncertainties were calculated – specifically the fakes and charge mis-ID The uncertainties considered for the analysis are summarized in Table 6.7. Values for experimental systematics on the trigger efficiency, lepton and jet reconstruction, and flavor tagging are taken directly from the 13 TeV analysis [1]. The rate uncertainties for the background processes are halved from the 13 TeV values.

Source	Uncertainty (%)
$W^{\pm}W^{\pm}jj$ (EWK)	3
Luminosity	1
Trigger efficiency	0.5
Lepton reconstruction and identification	1.8
Jets	2.3
Flavor tagging	1.8
Jets faking electrons	20
Charge misidentification	25
$W^{\pm}W^{\pm}jj$ (QCD)	20
Top	15
Diboson	10
Triboson	15

Table 6.7: Summary of estimated experimental and rate uncertainties.

6.6.3 Cross section measurement

The cross section is calculated using the same method as in the 13 TeV analysis, detailed in Chapter 5. TODO: update from chapter reference to subsection reference (once it's written)... Once again, each of the four lepton flavor channels is further split by charge (i.e. $\mu\mu \to \mu^+\mu^+ + \mu^-\mu^-$), as this increases the sensitivity of the analysis. Each channel's m_{jj} distribution is combined in a profile likelihood fit to extract the EWK $W^{\pm}W^{\pm}jj$ production cross section. The expected cross section calculated using the default event selection is:

$$\sigma^{\text{expected}}_{W^{\pm}W^{\pm}jj} = 16.89 \pm 0.36 \text{ (stat)} \pm 0.53 \text{ (theory)} \pm 0.84 \text{ (syst) fb} \tag{6.5}$$

The expected cross section calculated using the optimized event selection is:

$$\sigma^{\text{expected}}_{W^{\pm}W^{\pm}jj} = 16.94 \pm 0.36 \text{ (stat)} \pm 0.53 \text{ (theory)} \pm 0.78 \text{ (syst) fb} \tag{6.6}$$

The optimized selection should not change the measured value of the cross section, and indeed both are consistent with within uncertainties. The sytematic uncertainty is reduced by approximately 7% with the optimized selection. Projections of the total uncertainty on the cross section as a function of integrated luminosity made by TODO: how was this made? is shown in Figure 6.13. As the integrated luminosity increases past $\mathcal{L} > 3000$ fb^{-1}, the statistical uncertainty reduces faster than the systematic uncertainties. However, the total uncertainty is expected to reduce by less than a percent with increased luminosity past the planned 3000 fb^{-1}.

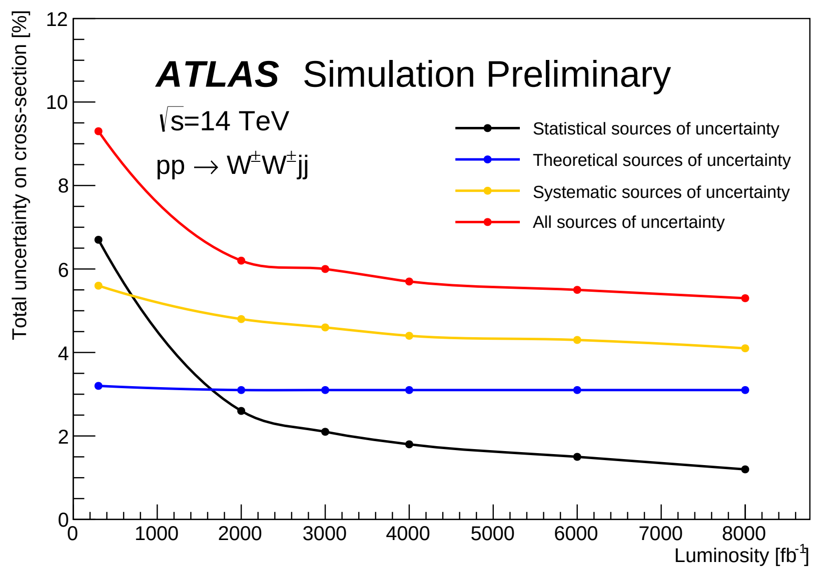

Figure 6.13: Projections of the statistical (black), theoretical (blue), systematic (yellow), and total (red) uncertainties on the measured cross section as a function of integrated luminosity using the optimized event selection.

6.6.4 Longitudinal scattering significance

TODO: get some details on how this was all done... The longitudinal scattering significance is extracted from the $|\Delta\phi_{jj}|$ distribution using a simultaneous binned likelihood fit. In order to increase sensitivity, the $|\Delta\phi_{jj}|$ distribution was split into two bins in m_{jj}, and an additional cut on the pseudorapidity of the subleading lepton was applied ($|\eta| < 2.5$) to reduce background from fake and charge misidentification. The $|\Delta\phi_{jj}|$ distributions used in the fit are shown in Figure 6.14. Due to limited statistics, the four lepton flavor channels were not split by charge. The expected significance of the $W_L^{\pm}W_L^{\pm}jj$ process is 1.8σ with a precision of 47% on the measurement. Projections of the expected significance as a function of integrated luminosity is shown in Figure 6.15.

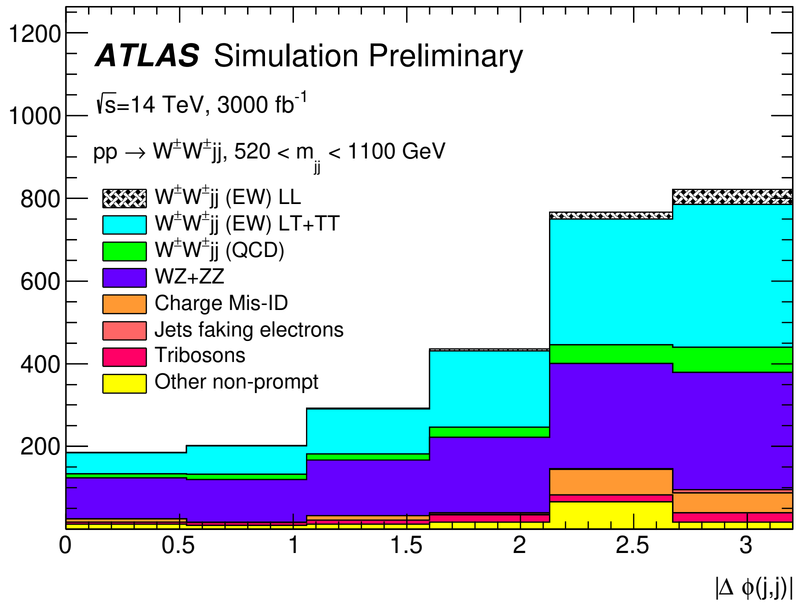

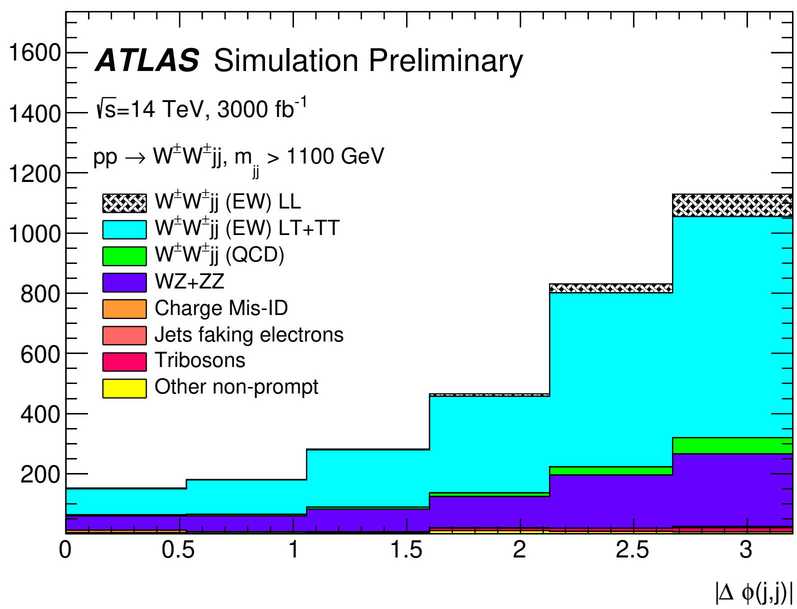

Figure 6.14: Dijet azimuthal separation ($|\Delta\phi_{jj}|$) for the low m_{jj} region ($520 < m_{jj} < 1100$ GeV, top) and the high m_{jj} region ($m_{jj} > 1100$ GeV, bottom). The purely longitudinal (LL, gray) is plotted separately from the mixed and transverse (LT+TT, cyan) polarizations.

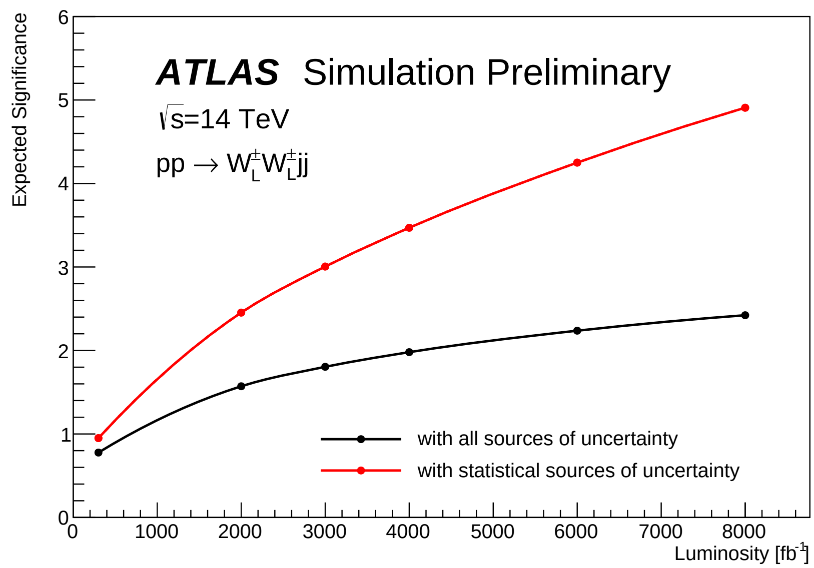

Figure 6.15: Projections of the expected longitudinal scattering significance as a function of integrated luminosity when considering all sources of uncertainties (black) or only statistical uncertainties (red).

Chapter 7

Conclusion

Here's where you wrap it up.

Looking Ahead

Here's an example of how to have an "informal subsection".

Appendix A

Additional material on truth isolation

yields by type	all channels	$\mu\mu$	ee	μe	$e\mu$
signal	4011	1583.2	531.7	793.1	1103.1
ww qcd	252.6	105.8	30.4	48	68.4
charge flip	2528.4	0.0	2075.4	255.1	197.8
fakes	7135.4	0.0	4675.1	1904.3	555.9
diboson	2370.4	581.2	491.8	517.9	779.6
triboson	125.5	49.1	17.8	24.6	34.1
top	90150.5	26618	15301.6	25277.9	22953.1
z+jets	241.2	0.0	0.0	0.0	241.2
w+jets	31.4	3.9	7.6	13.2	6.7
total bkg	102803.9	27354	22592	28027.8	24830.1
signal	4011	1583.2	531.7	793.1	1103.1

Table A.1: Event yields prior to applying any form of truth-based isolation criteria.

yields by type	all channels	$\mu\mu$	ee	μe	$e\mu$
signal	3470.5	1427.3	428.8	675.8	938.7
ww qcd	205.8	90.8	22.7	38.3	54
charge flip	2398.3	0.0	2104.6	95.8	197.9
fakes	4309.7	0.0	3390.6	750.8	168.3
diboson	1552.4	311.3	355.6	346.8	538.7
triboson	115	46.8	15.4	21.6	31.2
top	156.9	42.3	14.8	76.6	23.3
z+jets	0.0	0.0	0.0	0.0	0.0
w+jets	0.3	0.0	0.0	0.3	0.0
total bkg	8738.1	491.3	5903.7	1329.8	1013.4
signal	3470.5	1427.3	428.8	675.8	938.7

Table A.2: Event yields after applying a test version of the truth-based isolation.

TODO: Add tables for tight vs loose working point, information on the necessity of TRUTH1++

Bibliography

[1] ATLAS Collaboration Collaboration, *Observation of electroweak production of a same-sign W boson pair in association with two jets in pp collisions at $\sqrt{s} = 13$ TeV with the ATLAS detector*, Tech. Rep. ATLAS-CONF-2018-030, CERN, Geneva, Jul, 2018. https://cds.cern.ch/record/2629411. (document), 5, 5.8, 6.6.2

[2] S. L. Glashow, *The Renormalizability of Vector Meson Interactions*, Nucl. Phys. **10** (1959) 107–117. 2.2

[3] A. Salam and J. C. Ward, *Weak and Electromagnetic Interactions*, Nuovo Cimento **11** (1959) 568–577. 2.2

[4] L. R. Evans and P. Bryant, *LHC Machine*, JINST **3** (2008) S08001. https://cds.cern.ch/record/1129806. This report is an abridged version of the LHC Design Report (CERN-2004-003). 3.1

[5] ATLAS Collaboration, *The ATLAS Experiment at the CERN Large Hadron Collider*, JINST **3** (2008) S08003. 3.1

[6] ATLAS Collaboration Collaboration, *Alignment of the ATLAS Inner Detector Tracking System with 2010 LHC proton-proton collisions at $\sqrt{s} = 7$ TeV*, Tech. Rep. ATLAS-CONF-2011-012, CERN, Geneva, Mar, 2011. https://cds.cern.ch/record/1334582. 4

[7] ATLAS Collaboration, ATLAS Collaboration, *Evidence for Electroweak Production of $W^{\pm}W^{\pm}jj$ in pp Collisions at $\sqrt{s} = 8$ TeV with the ATLAS Detector*, Phys. Rev. Lett. **1**13 (2014) no. 14, 141803, arXiv:1405.6241 [hep-ex]. 5

[8] CMS Collaboration, V. Khachatryan et al., *Study of vector boson scattering and search for new physics in events with two same-sign leptons and two jets*, Phys. Rev. Lett. **1**14 (2015) no. 5, 051801, arXiv:1410.6315 [hep-ex]. 5

[9] CMS Collaboration, CMS Collaboration, *Observation of electroweak production of same-sign W boson pairs in the two jet and two same-sign lepton final state in proton-proton collisions at $\sqrt{s} = 13$ TeV*, arXiv:1709.05822 [hep-ex]. 5

[10] C. Bittrich, W. K. Di Clemente, E. M. Duffield, C. Geng, G. Gonella, J. Guo, B. Heinemann, T. Herrmann, F. Iltzsche Speiser, M. Kobel, K. Koeneke, J. I. Kroll, S. Li, J. Liu, Y. Liu, J. A.

Manjarres Ramos, G. Azuelos, C. A. Lee, M. Mittal, C. Mwewa, R. Ospanov, S. Pagan Griso, K. J. Potamianos, M. Shapiro, P. Sommer, S. Todt, Y. Wu, W. Xu, S. Yacoob, H. Yang, L. Zhang, Z. Zhao, B. Zhou, J. Zhu, and M.-A. Pleier, *Support note for measurement of electroweak $W^{\pm}W^{\pm}jj$ production at $\sqrt{s} = 13$ TeV*, Tech. Rep. ATL-COM-PHYS-2018-252, CERN, Geneva, Mar, 2018. https://cds.cern.ch/record/2309552. 5, 5.3.3, 2, 4

[11] B. W. Lee, C. Quigg, and H. B. Thacker, *The Strength of Weak Interactions at Very High-Energies and the Higgs Boson Mass*, Phys. Rev. Lett. **38** (1977) 883–885. 5.0.1

[12] S. D. Rindani, *Strong gauge boson scattering at the LHC*, in *Physics at the Large Hadron Collider*, A. Datta, B. Mukhopadhyaya, A. Raychaudhuri, A. K. Gupta, C. L. Khetrapal, T. Padmanabhan, and M. Vijayan, eds., pp. 145–155. 2009. arXiv:0910.5068 [hep-ph]. 5.0.1

[13] A. Alboteanu, W. Kilian, and J. Reuter, *Resonances and Unitarity in Weak Boson Scattering at the LHC*, JHEP **11** (2008) 010, arXiv:0806.4145 [hep-ph]. 5.0.1, 5.1

[14] ATLAS Collaboration, *Observation of a new particle in the search for the Standard Model Higgs boson with the ATLAS detector at the LHC*, Phys. Lett. B **716** (2012) 1, arXiv:1207.7214 [hep-ex]. 5.0.1

[15] CMS Collaboration, *Observation of a new boson at a mass of 125 GeV with the CMS experiment at the LHC*, Phys. Lett. B **716** (2012) 30, arXiv:1207.7235 [hep-ex]. 5.0.1

[16] J. M. Campbell and R. K. Ellis, *Higgs Constraints from Vector Boson Fusion and Scattering*, JHEP **04** (2015) 030, arXiv:1502.02990 [hep-ph]. 5.0.1, 5.0.2

[17] M. SZleper, *The Higgs boson and the physics of WW scattering before and after Higgs discovery*, arXiv:1412.8367 [hep-ph]. 5.0.1

[18] E. Accomando, A. Ballestrero, A. Belhouari, and E. Maina, *Isolating Vector Boson Scattering at the LHC: Gauge cancellations and the Equivalent Vector Boson Approximation vs complete calculations*, Phys. Rev. **D74** (2006) 073010, arXiv:hep-ph/0608019 [hep-ph]. 5.0.1

[19] P. Anger, B. Axen, T. Dai, C. Gumpert, C. Hasterok, B. Heinemann, M. Hurwitz, N. Ilic, M. Kobel, J. Liu, L. Liu, J. Metcalfe, S. Pagan Griso, B. Zhou, S. Hou, M.-A. Pleier, U. Schnoor, J. Searcy, F. Socher, A. Sood, A. Vest, L. Xu, and J. Zhu, *Same Sign $W^{\pm}W^{\pm}$ Production and Limits on Anomalous Quartic Gauge Couplings*, Tech. Rep. ATL-COM-PHYS-2013-990, CERN, Geneva, Jul, 2013. https://cds.cern.ch/record/1561731. Internal note for approved paper STDM-2013-06 https://atlas.web.cern.ch/Atlas/GROUPS/PHYSICS/PAPERS/STDM-2013-06/. 5.0.2, 5.1, 5.7

[20] J. Almond, L. Bianchini, C. Blocker, J. Klinger, A. Maslennikov, M. Owen, K. Skovpen, Y. Tikhonov, and U. Yang, *Search for heavy neutrino, W_R and Z_R gauge bosons in events with two high-P_T leptons and jets with the ATLAS detector in pp collisions at $\sqrt{s}$ = 8 TeV*, Tech. Rep. ATL-COM-PHYS-2013-810, CERN, Geneva, Jun, 2013. https://cds.cern.ch/record/1555805. This is the supporting note for EXOT-2012-24, which is now published as JHEP07 (2015) 162. 5.0.3

[21] ATLAS Collaboration, M. Aaboud et al., *Luminosity determination in pp collisions at $\sqrt{s}$ = 8 TeV using the ATLAS detector at the LHC*, Eur. Phys. J. **C76** (2016) no. 12, 653, arXiv:1608.03953 [hep-ex]. 5.1

[22] G. Avoni et al., *The new LUCID-2 detector for luminosity measurement and monitoring in ATLAS*, JINST **13** (2018) no. 07, P07017. 5.1

[23] ATLAS Collaboration, G. Aad et al., *The ATLAS Simulation Infrastructure*, Eur. Phys. J. **C**70 (2010) 823–874, arXiv:1005.4568 [physics.ins-det]. 5.1.1

[24] S. Agostinelli et al., *GEANT4 - a simulation toolkit*, Nucl. Instrum. Meth. **A**506 (2003) 250–303. 5.1.1

[25] T. Sjostrand, S. Mrenna, and P. Skands, *A Brief Introduction to PYTHIA 8.1*, Comput. Phys. Commun. **178** (2008) 852–867, arXiv:0710.3820 [hep-ph]. 5.1.1

[26] T. Gleisberg et al., *Event generation with SHERPA 1.1*, JHEP **02** (2009) 007, arXiv:0811.4622 [hep-ph]. 5.1.1

[27] S. Schumann and F. Krauss, *A parton shower algorithm based on Catani-Seymour dipole factorization*, JHEP **03** (2008) 038, arXiv:0709.1027 [hep-ph]. 5.1.1

[28] S. Höche, F. Krauss, S. Schumann, and F. Siegert, *QCD matrix elements and truncated showers*, JHEP **05** (2009) 053, arXiv:0903.1219 [hep-ph]. 5.1.1

[29] R. D. Ball et al., *Parton distributions for the LHC Run II*, JHEP **04** (2015) 040, arXiv:1410.8849 [hep-ph]. 5.1.1

[30] S. Alioli, P. Nason, C. Oleari, and E. Re, *A general framework for implementing NLO calculations in shower Monte Carlo programs: the POWHEG BOX*, JHEP **06** (2010) 043, arXiv:1002.2581 [hep-ph]. 5.1.1

[31] A. Ballestrero et al., *Precise predictions for same-sign W-boson scattering at the LHC*, Eur. Phys. J. **C**78 (2018) no. 8, 671, arXiv:1803.07943 [hep-ph]. 5.1.1

[32] J. Alwall, R. Frederix, S. Frixione, V. Hirschi, F. Maltoni, O. Mattelaer, H. S. Shao, T. Stelzer, P. Torrielli, and M. Zaro, *The automated computation of tree-level and next-to-leading order differential cross sections, and their matching to parton shower simulations*, JHEP **07** (2014) 079, arXiv:1405.0301 [hep-ph]. 5.1.1

[33] H.-L. Lai, M. Guzzi, J. Huston, Z. Li, P. M. Nadolsky, J. Pumplin, and C. P. Yuan, *New parton distributions for collider physics*, Phys. Rev. D **82** (2010) 074024, arXiv:1007.2241 [hep-ph]. 5.1.1

[34] T. Sjostrand, S. Mrenna, and P. Skands, *PYTHIA 6.4 physics and manual*, JHEP **05** (2006) 026, arXiv:0603175 [hep-ph]. 5.1.1

[35] ATLAS Collaboration, G. Aad et al., *Muon reconstruction performance of the ATLAS detector in protonproton collision data at $\sqrt{s}$ =13 TeV*, Eur. Phys. J. **C**76 (2016) no. 5, 292, arXiv:1603.05598 [hep-ex]. 5.2.1.1, 5

[36] ATLAS Collaboration Collaboration, *Electron efficiency measurements with the ATLAS detector using the 2015 LHC proton-proton collision data*, Tech. Rep. ATLAS-CONF-2016-024, CERN, Geneva, Jun, 2016. `https://cds.cern.ch/record/2157687`. 5.2.1.2

[37] M. Cacciari, G. P. Salam, G. Soyez, *The anti-k_t jet clustering algorithm*, JHEP **04** (2008) 063, arXiv:0802.1189 [hep-ph]. 5.2.1.3, 6.4.1

[38] ATLAS Collaboration, M. Aaboud et al., *Jet energy scale measurements and their systematic uncertainties in proton-proton collisions at $\sqrt{s} = 13$ TeV with the ATLAS detector*, Phys. Rev. **D96** (2017) no. 7, 072002, arXiv:1703.09665 [hep-ex]. 5.2.1.3

[39] *Tagging and suppression of pileup jets with the ATLAS detector*, Tech. Rep. ATLAS-CONF-2014-018, CERN, Geneva, May, 2014. `http://cds.cern.ch/record/1700870`. 5.2.1.3

[40] D. Adams, C. Anastopoulos, A. Andreazza, M. Aoki, L. Asquith, M. Begel, F. Bernlochner, U. Blumenschein, A. Bocci, S. Cheatham, W. Davey, P.-A. Delsart, P.-O. DeViveiros, A. Dewhurst, D. Duschinger, F. Filthaut, P. Francavilla, F. Garberson, S. Head, A. Henrichs, A. Hoecker, M. Kagan, B. Kersevan, T. Khoo, B. Lenzi, D. Lopez Mateos, B. Malaescu, Z. Marshall, T. Martin, C. Meyer, A. Morley, W. Murray, M. zur Nedden, R. Nicolaidou, S. Pagan Griso, G. Pasztor, P. Petroff, C. Pizio, R. Polifka, X. Poveda, R. Reece, F. Ruehr, F. Salvatore, R. Sandstroem, T. Scanlon, D. Scheirich, S. Schramm, A. Schwartzman, K. Suruliz, M. Sutton, E. Thompson, M. Tripiana, A. Tuna, S. Viel, M. Vincter, I. Vivarelli, M. Wielers, A. Wildauer, and Z. Zinonos, *Recommendations of the Physics Objects and Analysis Harmonisation Study Groups 2014*, Tech. Rep. ATL-PHYS-INT-2014-018, CERN, Geneva, Jul, 2014. `https://cds.cern.ch/record/1743654`. 5.2.1.4

[41] ATLAS Collaboration, M. Aaboud et al., *Measurement of the cross-section for producing a W boson in association with a single top quark in pp collisions at $\sqrt{s} = 13$ TeV with ATLAS*, JHEP **01** (2018) 063, arXiv:1612.07231 [hep-ex]. 5.2.1.4

[42] ATLAS Collaboration, M. Aaboud et al., *Performance of missing transverse momentum reconstruction with the ATLAS detector using proton-proton collisions at $\sqrt{s} = 13$ TeV*, Eur. Phys. J. **C78** (2018) no. 11, 903, arXiv:1802.08168 [hep-ex]. 5.2.2

[43] ATLAS Collaboration, M. Aaboud et al., *Measurements of b-jet tagging efficiency with the ATLAS detector using $t\bar{t}$ events at $\sqrt{s} = 13$ TeV*, JHEP **08** (2018) 089, arXiv:1805.01845 [hep-ex]. 5.2.2

[44] J.-F. Arguin, J. Claude, G. Gonella, B. P. Kersevan, and K tech. rep. 5.3.3

[45] R. Steerenberg, *LHC Report: Another run is over and LS2 has just begun...*, `https://home.cern/news/news/accelerators/lhc-report-another-run-over-and-ls2-has-just-begun`, 2018. Accessed: 2018-12-14. 6

[46] *Letter of Intent for the Phase-I Upgrade of the ATLAS Experiment*, Tech. Rep. CERN-LHCC-2011-012. LHCC-I-020, CERN, Geneva, Nov, 2011. `http://cds.cern.ch/record/1402470`. 6

[47] G. Apollinari, I. Bjar Alonso, O. Brning, M. Lamont, and L. Rossi, *High-Luminosity Large Hadron Collider (HL-LHC): Preliminary Design Report.* CERN Yellow Reports: Monographs. CERN, Geneva, 2015. `https://cds.cern.ch/record/2116337`. 6

[48] ATLAS Collaboration Collaboration, ATLAS Collaboration, *ATLAS Phase-II Upgrade Scoping Document*, Cern-lhcc-2015-020, Geneva, Sep, 2015. `http://cds.cern.ch/record/2055248`. 6

[49] D. Espriu and B. Yencho, *Longitudinal WW scattering in light of the "Higgs boson" discovery*, Phys. Rev. D **87** (2013) 055017, arXiv:1212.4158 [hep-ph]. 6, 6.1

[50] ATLAS Collaboration Collaboration, *Prospects for the measurement of the $W^{\pm}W^{\pm}$ scattering cross section and extraction of the longitudinal scattering component in pp collisions at the High-Luminosity LHC with the ATLAS experiment*, Tech. Rep. ATL-PHYS-PUB-2018-052, CERN, Geneva, Dec, 2018. http://cds.cern.ch/record/2652447. 6

[51] ATLAS Collaboration Collaboration, *Studies on the impact of an extended Inner Detector tracker and a forward muon tagger on $W^{\pm}W^{\pm}$ scattering in pp collisions at the High-Luminosity LHC with the ATLAS experiment*, Tech. Rep. ATL-PHYS-PUB-2017-023, CERN, Geneva, Dec, 2017. https://cds.cern.ch/record/2298958. 6

[52] T. Sjöstrand, S. Ask, J. R. Christiansen, R. Corke, N. Desai, P. Ilten, S. Mrenna, S. Prestel, C. O. Rasmussen, and P. Z. Skands, *An Introduction to PYTHIA 8.2*, Comput. Phys. Commun. **1**91 (2015) 159–177, arXiv:1410.3012 [hep-ph]. 6.2

[53] ATLAS Collaboration Collaboration, *Expected performance for an upgraded ATLAS detector at High-Luminosity LHC*, Tech. Rep. ATL-PHYS-PUB-2016-026, CERN, Geneva, Oct, 2016. http://cds.cern.ch/record/2223839. 6.3

[54] P. C. Bhat, H. B. Prosper, S. Sekmen, and C. Stewart, *Optimizing Event Selection with the Random Grid Search*, Comput. Phys. Commun. **2**28 (2018) 245–257, arXiv:1706.09907 [hep-ph]. 6.5.1

[55] G. Cowan, K. Cranmer, E. Gross, and O. Vitells, *Asymptotic formulae for likelihood-based tests of new physics*, Eur. Phys. J. **C**71 (2011) 1554, arXiv:1007.1727 [physics.data-an]. [Erratum: Eur. Phys. J.C73,2501(2013)]. 6.5.1